Title
The Development and Use of the Berkeley Fluorescence Spectrometer to Characterize Microbial Content and Detect Volcanic Ash in Glacial Ice

Author
Rohde, Robert Andrew

Publication Date
2010

Peer reviewed|Thesis/dissertation

The Development and Use of the Berkeley Fluorescence Spectrometer to Characterize Microbial Content and Detect Volcanic Ash in Glacial Ice

by

Robert Andrew Rohde

A dissertation submitted in partial satisfaction of the requirements for the degree of

Doctor of Philosophy

in

Physics

in the

Graduate Division

of the

University of California, Berkeley

Committee in charge:

Professor P. Buford Price, Chair
Professor Richard Muller
Professor Kurt Cuffey

Fall 2009

Abstract

The Development and Use of the Berkeley Fluorescence Spectrometer to Characterize Microbial Content and Detect Volcanic Ash in Glacial Ice

by

Robert Andrew Rohde

Doctor of Philosophy in Physics

University of California, Berkeley

Professor P. Buford Price, Chair

The Berkeley Fluorescence Spectrometer (BFS) was designed and implemented to provide rapid non-destructive characterizations of the organic / microbial content in glacial ice. The resulting information is general, aiming at bulk microbial concentration and a few identifiable classes of microbes, but nonetheless can provide orders of magnitude more data than can be reasonably obtained via the slow process of cutting and sampling. This instrument has now scanned ice cores segments from a variety of Antarctic and Greenland sites including a majority of the 580 m of the WAIS Divide Core (WDC) that has been archived at the National Ice Core Laboratory (NICL). A sustained scanning rate of 4 minutes per ice core meter has been achieved with seven channel fluorescence spectra collected every 750 microns.

These scans have provided the largest collection of data on the microbial content of glacial ice ever assembled. They show the microbial content of the ice to be fairly homogenous in bulk but heterogeneous at the fine scale. We further discovered that the observed fluorescence declines ~95% during the top ~100m of all ice cores for which scans have been conducted. This decline corresponds to the transition from snow to fully dense ice and the signal response may reflect a combination of changes in the microbial population of the ice mixed with changes in the optical properties of the ice itself. Thus far microbial deposits have not shown the kind of the large-scale continuity that would be required to coordinate events over large scales or make them useful for dating. However, the BFS has revealed an unexpected sensitivity to volcanic ash that makes it a very sensitive non-destructive system for detecting faint ash layers in archived ice cores.

Table of Contents

1 Introduction 1
2 Hardware 3
2.1 Targeted Ultraviolet Chemical Sensor (TUCS) 3
2.1.1 Laser System and Internal Power Sensor 4
2.1.2 Laser Safety 7
2.1.3 Communications and Control 8
2.1.4 Phototubes 9
2.2 Optical Elements 10
2.3 Photon Counter System 11
2.3.1 Photon counting modules 13
2.4 Mounting and Translation Stage 15
2.5 Micromanipulator 16
2.6 Miscellaneous Equipment 17
3 Labview Control Software 18
3.1 Communications Panel 19
3.2 Frankenstein Communication Panel 19
3.3 Laser Control Panel 20
3.4 Data Logging Panel 20
3.5 Configuration Panel 21
3.6 Motor Controller Panel 22
3.7 Micromanipulator Variant 22
3.8 Labview Programming 23
3.9 File Format 23
3.10 Original TUCS Code 24
4 Analysis Stack 24
4.1 Uncertainty Analysis 26
5 Fluorescence Scanning Results 27
5.1 2008 NICL Trip – WAIS Divide 27
5.2 2009 NICL Trip – GISP2, Siple Dome, WAIS, RIDS, Vostok, and South Pole 29
5.3 Two-dimensional scans 30
6 Analysis 32
6.1 Comparison of 2008 and 2009 intensities 32
6.2 Artifacts 33
6.2.1 Drill fluid contamination 33
6.2.2 Edge effects 33
6.2.3 Ice fractures 35
6.3 Trend with Depth 35
6.4 Spectral Analysis 37
6.5 Annual Cycle 39
6.6 Greenland versus Antarctica 39
6.7 Volcanic Index 40
7 Future Work 41
7.1 Recommendations for a Future BFS 43
8 References 46

9 Figures 50
10 Appendix 91
10.1 Labview Control Program 91
10.2 Matlab Analysis Script 91

Acknowledgements

Thanks to Nathan Bramall and Ryan Bay for their frequent material assistance and help on this project. Further thanks to the staff at NICL for their assistance in making this work possible, especially Erik Cravens and Geoff Hargreaves. Deep gratitude to Rich Muller and Kurt Cuffey for reviewing this work. Love to L., J., and C. for their emotional support and encouragement to finally get this thing done. And special thanks to Buford Price for his direction and support.

This work is dedicated to the memory of Leo F. Rohde (June 8, 1948 – June 9, 2007) who is dearly missed. Though he did not live to see this work completed, his love, support, and respect played a large role in getting here.

This work was primarily supported by NSF Office of Polar Programs grants 0440609 and 0738658.

1 Introduction

The microbial abundance and composition in glacial ice has thus far been poorly characterized. A single measurement will often consist of sawing a piece of ice from an appropriate ice core, melting it under sterile conditions, concentrating its contents, and then examining it using either microscopy and/or genetic techniques. This whole process can take several days for each piece of data retrieved. Consequently, relatively few studies have attempted to characterize life in glacial ice. Figure 1 shows a review of eight studies that have attempted to measure cell concentrations in ice through direct cell counting and they have collectively produced slightly more than 80 measurements. The typical cell concentration reported generally varies from $10^4 – 10^6$ cells / cm^3 for Greenland sites (Miteva et al. 2009; Tung et al. 2005) and $10^2 – 10^4$ cells / cm^3 by researchers working on Antarctica sites (Abyzov et al. 1998, Abyzov et al. 2004a, Abyzov et al. 2004b, Abyzov and Perovich 2007, Christner et al. 2006).

The goal in designing the Berkeley Fluorescence Spectrometer (BFS) was to overcome the long measurement delays by creating a system to rapidly characterize the microbial content in ice. The strategy has been to use the autofluorescence[a] of biomolecules when excited at ultraviolet wavelengths – specifically 224 nm – to measure the relative abundance of microbes and provide limited information about the types of microbes present. In its basic form, fluorescent substances absorb high energy photons and emit characteristic lower energy photons in response. In most cases, the high energy photon creates a transient electronic excited state within the targeted molecule or atom that is then promptly reduced to a meta-stable electronic state via molecular interactions or energy transfer via other non-radiative modes (Lakowicz 1999). The meta-stable state then decays to lower energy state, often the ground state, via emission of a characteristic photon. Since the key transition occurs between at intermediate meta-state, the energy of the emitted photon is predictable, relatively insensitive to excitation energy, and always of lower energy than the original excitation photon. Most fluorescent compounds allow the excitation to occur over a wide range of energies above the minimum required to reach the meta-stable state. In the absence of thermal effects, the emitted photon would come from one (or a few) narrow energy bands, but at temperatures near room temperature the possible emitted states are broadened and often cover 50 nm or more of wavelength space (Lakowicz 1999). The necessary excitation energy required to provoke fluorescence, if possible at all, varies greatly for different molecules due to variation in their electronic configuration. Commonly encountered fluorescence compounds generally have one of two features that reduce the energy needed to reach a suitable electronic state. For organic compounds the key characteristic is usually π-bonded ring structures, and for inorganic materials fluorescence occurs most often in the presence is partially shielded unfilled p-orbitals such as are present in some transition metals (Lakowicz 1999).

Using fluorescence with ice is possible because pure ice is essentially transparent at ultraviolet wavelengths longer than ~200 m (Ackermann et al. 2006), though in practice bubbles

[a] Autofluorescence refers to a molecule's intrinsic fluorescence not dependent on any stain or other chemical alteration.

usually create an abundance of short-range scattering. At our 224 nm excitation, the amino acids tryptophan and tyrosine are the brightest sources of fluorescence in most cellular environments, though some compounds such as Chlorophyll may be brighter on a per molecule basis when present (Lakowicz 1999). Since these amino acids are ubiquitous in all life, it has been expected that looking at their fluorescence would provide an immediate proxy for the total cell mass in ice. The excitation and emission spectra for the amino acids tryptophan, tyrosine, and phenylalanine are shown in Figure 2 and Figure 3 respectively. These three are the only proteinogenic amino acids with benzene rings, which enhances their fluorescence potential. The higher absorbance of tryptophan at 224 nm excitation is approximately balanced by the higher emission intensity of tyrosine and tyrosine's 120% greater abundance in the natural environment (Tourasse and Li 2000). However as discussed in Section 6.4, this may be partially countered by the potential for tryptophan to quench tyrosine. We also expect that tyrosine may be important for detecting endospores due to the high levels of tyrosine generally found in their coats (Ricca and Cutting 2003).

As designed the BFS can provide approximately ten 7-channel fluorescence spectra per second, greatly exceeding the rate and data volume of traditional cell counting techniques used when working with ice. The intention has been to create a systematic characterization of microbial abundances throughout ice cores. In addition to bulk abundances associated with amino acids, fluorescence can identify certain other compounds such as chlorophyll (diagnostic of phototrophs) and coenzyme F420 (diagnostic of methanogens), and other targets of opportunity. This document will focus on tryptophan/tyrosine and chlorophyll-like fluorescence. Though the characterization available via fluorescence is limited to only bulk cell content and a few classes of microbes with specifically identifiable biomolecules, this has the potential to greatly improve the quantitative and qualitative understanding of how life is distributed in ice assuming fluorescence data can be tied to true concentrations of microbes. This should complement existing genetic studies that aim to enumerate the species of microbes present in particular ice samples but which often provide little or no information about abundance and distribution (Bidle et al. 2007, Christner et al. 2000, Miteva et al. 2009, Willerslev et al. 1999, Miteva et al. 2004).

Except near the base of the ice sheet, all cells in glacial ice originally derive from wind-borne transport that passively deposits them onto the snow. It is hoped that studying the distribution of microbes in ice may provide a proxy for weather related variations in transport. Further, the changes in deposition over time might provide insight into climatic events and provide other information about either changing conditions for transport or changing growth conditions at the microbial source regions. At the same time, systematic changes versus depth could provide insight into adaptations affecting the survivability of microbes in ice. If the BFS can rapidly identify heterogeneity in the ice, then follow-up studies can more easily investigate the factors that help microbes survive the transition to a glacial environment.

The fraction of cells that survive deposition and remain viable over long time periods in glacial ice is a subject of disagreement, with claims ranging from 2% to 80% of cells being viable (Yung et al. 2007, Zhang et al. 2008, Christner et al. 2006, Abyzov et al. 1999, Sheridan et al. 2006, Zhang et al. 2003), where much of discrepancy is attributable to methodological issues in defining viability for the large fraction of cells that may be alive but do not respond to be culturing attempts. Regardless of the exact fraction, it is clear that at least a small fraction of cells extracted from glaciers can remain viable and be cultured even after hundreds of thousands

or even millions of years in ice (Bidle et al. 2007, Christner et al. 2000, Tung et al. 2005, Yung et al. 2007). In order to repair spontaneous macromolecular degradation over the longest timescales it is likely that these cells need to have at least a minimal level of metabolic activity while imprisoned in ice (Tung et al. 2005, Bidle et al. 2007). Several papers have developed a theoretical and experimental framework for different modes of life that are possible in ice, including: life attached to dust grains facilitated by iron metabolism (Tung et al. 2006), life in the vein network created at the triple junctions between ice grains and fed by organic compounds excluded during freezing (Price 2000, Junge et al. 2004, Mader et al. 2006), and life imprisoned in ice crystals and fed by solid state diffusion of small molecules (Rohde and Price 2006). Ultimately the BFS may help distinguish between these different modes of life and their relative importance, though only rudimentary steps in that direction are taken in this thesis.

An important side effect of active metabolism in glacial ice is that it can alter the abundance of the organic compounds in the ice. In particular, the in situ biological production or destruction of compounds such as CO_2 and CH_4 has the potential to be a confounding factor with respect to attempts to use ice cores to determine past atmospheric conditions. It has long been realized that the 10^4 fold excess of CH_4 and 500 fold excess of CO_2 in the basal ice at Greenland is driven by microbial activity with cell concentrations of $10^7 - 10^9$ cells / cm^3 present in the basal ice (Sheridan et al. 2003, Tung et al. 2006, Souchez et al. 1995). However these cells are directly associated with the basal silt and are being dragged up from the subglacial environment (Tung et al. 2006, Souchez 1997). It remains less clear whether in situ metabolism by the much lower cell concentrations present in the bulk of the glacial ice can appreciably alter the concentrations of atmospherically relevant gases; however, in the case of certain NO2 anomalies we argued for this conclusion using preliminary fluorimetry data (Rohde et al. 2008). As the metabolic rates for typical cells are expected to be extremely low given the low temperatures (Tung et al. 2005), the accumulation of waste products is expected to matter only over very long time periods (~10^5 years) and for gases where the atmospheric abundance was very low to begin with. For scale, 10^4 bacterial cells / cm^3 would have to oxidize a carbon mass equal to their own total carbon content in order to raise CO_2 concentrations ~3 ppm (2% of glacial mean). However, given sufficient time, 10^2 hydrogenotrophic methanogens / cm^3 might plausibly convert 12% of the glacial H_2 and 0.01% of the CO_2 to create a 10% anomaly in glacial CH_4. Ultimately though, the observation that trace gases appear similar in many different Antarctic and Greenland ice cores (Stauffer et al. 1998, Stauffer et al. 2002, Schilta et al. in press) – generally supports the conclusion that biological alteration, if it occurs, is only infrequently a significant factor.

2 Hardware

2.1 Targeted Ultraviolet Chemical Sensor (TUCS)

The first generation of measurements on this project relied on a Targeted Ultraviolet Chemical Sensor (TUCS) manufactured by Photon Systems of Covina, California. This system is a compact, portable fluorescence spectrometer using a 224 nm ultraviolet (UV) excitation (Photon Systems 2007, Photon Systems 2009). During the course of this work the spectrometric

aspects of the TUCS were replaced (see Section 2.3), but the laser system has continued to be used. The TUCS incorporates a pulsed 224 nm AgHe gas laser of a proprietary design[b] to excite fluorescence in target compounds and in the current work is primarily intended to target the autofluoresence[c] of biomolecules, especially tryptophan, tyrosine, and chlorophyll-like chromophores. In the commercial TUCS, this fluorescence is captured by 6 band-pass filtered photo multiplier tubes positioned to capture emitted light from around the excitation focus. The selection of ½″ filters to use with the tubes is at the operator's discretion and may be tailored towards the identification of various compounds (Photon Systems 2009, Bhartia et al. 2008). As discussed in Chapter 2.3 in the Berkeley Fluorescence System (BFS), these phototubes were replaced by a system of seven photon counting modules.

The laser system is shown photographically in Figure 4. The principal components are the laser tube mounted on a central partition, an analysis board, a power controller, a communications board, the optical path, an arrangement of phototubes, and a power sensor. Within the optical path, diagrammed in Figure 5, there are three alignment mirrors, an internal partition, a 1% partial mirror, and the internal power sensor. The alignment mirrors additionally serve as short-pass filters as they are only reflective at UV wavelengths (roughly 250 nm and below), thus removing additional spectral lines that may be excited in the laser tube. This approach was chosen because traditional transmission-based excitation filters generally have very low efficiencies at the 224 nm wavelength. Each alignment mirror is mounted on a two rotational axis mini-platform that can be adjusted through the use of Allen wrenches for fine manipulation of the beam path. After the three mirrors, the beam encounters a partially silvered mirror redirecting approximately 1% of the beam to a photodiode serving as an internal power sensor. The bulk of the beam then exits the instrument through a vertical exit port.

2.1.1 Laser System and Internal Power Sensor

During the alignment process the goal is for the beam to exit vertically while centered down the emission port. However, in addition, it is important to ensure that the 1% sample of the beam falls on the center of the power sensor. This sensor was calibrated based on a factory measurement of the emitted power beyond the emission port to produce a measure of the total power per pulse, with a nominal expectation of approximately 1 μJ when configured for a 100 μs pulse. As the absolute laser power can vary greater due to different laser settings and variations in alignment quality, such power readings are important to making comparisons between different configurations.

The photodiode used for internal calibrations is operated in such a fashion that a time-resolved intensity pattern is reported with better than 1 μs reported precision. As shown in Figure 6, the reported intensity generally has an apparent quiescent phase of ~30 μs during which current is applied to the laser tube but little or no laser light is registered. Given that light can travel the length of the tube tens of thousands of times during that duration, such a delay is

[b] The AgHe laser, i.e. a silver-helium gas laser, is a patented design of Photon Systems qualitatively similar to the more conventional helium-neon lasers (HeNe). To our knowledge no other company makes, or is allowed to make, silver-helium laser.

[c] "Autofluorescence" refers to the intrinsic tendency of certain compounds to fluoresce without the need to add additional dyes or other compounds.

unexpected. Subsequent tests conducted with photon counters suggest that the delay is largely or entirely fictitious and that the lasing occurs during essentially the entire 100μs window over which current is applied to the laser tube. Our working hypothesis is that the reported delay (and possibly the large variations in reported intensity) is the result of electrical "inertia" in the measurement circuit rather than actual variations in output. We note that the TUCS photodiode provides a voltage output that is cabled to the data acquisition board via a 30 cm twisted-pair ribbon cable. Given a typical self-inductance of order $4x10^{-7}$ H/m and cable resistance 20 mΩ the RL time constant is already of order 6 μs. Even without considering other circuit elements, this adds plausibility to the conclusion that the delay and quasi-oscillation seen in Figure 6 is a product of poor circuit design. However, as the detection equipment available to us could not provide a time resolved laser measurement for direct comparison, the true temporal evolution of the laser pulse is not currently known.

In light of the questionable performance of the power sensor, its results should be treated with some skepticism. Ideally, the power received at the emission port should be measured and used to recalibrate the internal sensor each time the laser settings are changed or the system realigned. However, as we did not become aware of the apparent problems with the internal sensor until recently, no such calibrations were generally done for the measurements reported in this thesis. As a result we generally are forced to assume that the integrated current from the photodiode is proportional to laser power. This is probably reasonable for the small pulse-to-pulse variations within a given run, but is unverified for the much larger variations associated with varying run conditions. Since we only rely on the integrated current and all reported data herein was taken with the same 100 μs laser duration, we can hope that the resonance effects in the measurement circuit are somewhat mitigated.

The laser beam is emitted from the laser tube as a circular spot approximately 3 mm in size. It is not visible under ordinary conditions, but can be easily visualized by interrupting the beam by either white paper or green fluorescent dots. In either case the UV light is downshifted into the visible and is apparent to the naked eye even under room light conditions. Due to the 45° angle of the last alignment mirror, this spot will be elongated at the emission port. In the case of poor alignment, there are several opportunities for the laser beam to be partially occluded during the optical path and hence checking the shape of the emitted beam is a valuable check on the alignment. It should be noted that the active surface of the photodiode used as the internal power sensor is of similar dimensions to the laser beam itself. As a result one must be careful to ensure that the laser beam remains centered on the power sensor; otherwise it will only read part of the incident energy. This can usually be accomplished by making fine adjustments to the alignment mirror while attempting to maximize the reported laser intensity.

The AgHe laser is proprietary technology belonging to Photon Systems and identified as 224.3 nm (Photon Systems 2007). The basic construction of the tube itself is not uncommon and similar to that of other gas lasers. It consists of an approximately 20 cm tube filled with diffuse vapor and excited by a co-axial high voltage current arc. Typical mode is 400 V at 11 A, which is a much higher power than the 2000 V at 6.5 mA typical for HeNe lasers (Verdeyen 2000). Unlike most laser systems, which tightly constrain the lasing wavelength, the AgHe system allows a fairly broad range of wavelengths to escape the laser tube. This is a compromise due to the lack of high quality UV emissions filters. At the upper wavelength end, the alignment mirrors are non-reflective above ~260 nm and at the lower end even UV-tolerant fused silica will become absorptive below ~180nm. The exact details of the laser configuration are proprietary,

but based on the NIST reference tables (Ralchenko et al. 2009) we assume that the high intensity lines at 224.651, 231.004, and 216.189 nm of Ag^{+3} are the most significant components of the main output. However, it is possible that the 200.024 and 197.592 nm excitations represent significant side bands. If the above speculation is correct, the need to maintain a triply ionized silver vapor may explain why ~0.5 J of energy is required per 1 μJ of laser emission. This makes the AgHe laser a factor of 500 less efficient than a typical HeNe laser (Verdeyen 2000). We have not had access to equipment capable of resolving the UV emission bands, and have relied on Photon Systems' nominal description of 224 nm in our analysis.

Because Ag is not a gas at room temperature, it will generally be deposited on the inside surface of the tube. It is vaporized by the high current of the discharge arc. As a result, the laser may need to be primed by multiple current pulses before it reaches a stable operating condition. Photon Systems suggests that as many as 1000 pulses may be necessary, but in practice we find that stability is often achieved after as few as ten pulses.

As is typical of high-end gas lasers, the system has two alignment mirrors, one partially silvered, in order to form the resonant optical cavity. The mirrors are placed in tube mounts whose alignment may be adjusted by bending the entire tube under forces exerted by four alignment screws (Figure 5). Such alignment is possible at both ends, but it is highly recommended that one limit adjustments to only the fully silvered mirror at the rear of the instrument to the degree that this is possible. The laser's output is extremely sensitive to the alignment of these tubes, and the tubes themselves can become misaligned due to vibrations and other rough handling of the instrument as a whole. When correctly aligned, the laser beam emitted by the tube will be circular. When partially aligned, the emitted beam will usually appear as a partially truncated circle. If totally misaligned, the tube emits only a diffuse glow created by the current arc with no discernable lasing. When partially aligned, the alignment can usually be fixed by adjusting one or more alignment screws by very small increments (typically 1/8 of a revolution or less) so as to torque the tube in a direction counter to the observed clipping.

When completely misaligned, it is necessary to search the available two-dimensional alignment space to find the position for lasing. With the laser operating, it is often possible to apply manual pressure to the alignment collar with either a finger or an implement such as an Allen wrench to test for the correct direction prior to adjusting the alignment screws. To avoid overstressing the collar, such tests may be best conducted with all of the alignment screws rolled back so no additional pressure is being exerted on the collar. Once one determines the correct direction to move, the screws should be applied in small increments. Assuming the alignment was recently correct, it is unlikely that the instrument will require an exerted force greater than ¼ of a revolution of the alignment screw. Once the optical alignment is approximately correct, fine adjustments to the laser can be made using variations in the internal power reading to guide adjustments.

It is important not to overstress the alignment collar. Excess force can fracture the collar, exposing the laser tube to open air, and requiring a complete replacement of the tube. This happened only once (in mid 2009) after we received a new laser with alignment tubes of Kovar[d] rather than the prior stainless steel material. The new material is stiffer and more resistant to

[d] Kovar is the trade name of a Fe-Ni-Co alloy developed by Carpenter Technology Corporation that is designed to match the thermal expansion characteristics of borosilicate glass, which makes it well suited to mounting the mirrors while avoiding thermal stress.

thermal stress; however, this also makes it more fragile. Photon Systems reported that they had never previously had a client with a fractured alignment tube. Because the alignment was occurring at -20 °C, it is possible that the low temperature was a contributing factor to this unusual failure mode. At the same time, we found that the Kovar was more tolerant towards thermal shock. A laser properly aligned at room temperature still generally functioned well at -20 °C, whereas our experience with the stainless steel was that it nearly always required realignment after any thermal transition.

The laser control software is configured to only allow repetition rates of up to 10 Hz. We found that this limitation could be bypassed by sending "single fire" commands at a higher rate. Photon Systems has said that they have stably operated the system at 50 Hz. Due to other factors (section 2.3) the BFS was generally limited to operation at no more than 12.5 Hz. This rate was only ever briefly exceeded during hardware tests and we never attempted to take the laser above 15 or 20 Hz. It should also be noted that the electronics for the phototubes included with the generic TUCS configuration have an apparent discharge time in the tens of ms range, which means they are unsuitable for high-speed operation. Even at 10 Hz the electronics associated with those phototubes showed evidence of bleed-through from one measurement to the next (Section 2.1.4), though this issue was eliminated by the BFS switch to photon counters in 2008.

2.1.2 Laser Safety

The 224 nm TUCS laser is a Class 3B laser device (pulsed laser less than 400 μJ at 200-250 nm). By law such lasers require a key lock, provided at the rear of the TUCS. UC Berkeley regulations further require the operators of all such lasers have approval and specialized training and that warning systems be used prior to activation.

At only 1 μJ per pulse, the energy delivered per pulse in a focused beam (0.5 mm diameter) is approximately 5 J / m^2, substantially below the 250 J / m^2 recommended skin exposure limit at 225 nm (Moseley 1994). As such, the laser is not a significant hazard due to incidental skin exposure (though repeated or intentional exposure is not recommended). Even with repeated exposure, this laser will not burn skin or any other likely target, but it may lead to the breakdown of DNA and other organic compounds, with potentially carcinogenic effects. Sunlight at the Earth's surface contains no radiation at 224 nm.

Coherent exposure to the laser (direct or reflected) presents a possible eye hazard. Eye protection is recommended whenever the laser system is in use. Because 224 nm light is highly absorbed by plastics, most plastic (not glass) safety goggles will fully block the beam. This can be directly tested by placing the goggles into the beam and verifying that it does not penetrate. Depending on material, there may be a diffuse visible flash in response to exposure to the ultraviolet beam; such a pulse is not hazardous.

Far ultraviolet, such as 224 nm, will not penetrate into the eye and as a result poses no risk to the retina, but it may cause burns to the cornea (Moseley 1994). Ultraviolet lasers at ~190 nm are routinely used to cut corneal tissue in eye surgeries (e.g. Gartry 1997). A similar laser system at 213 nm with a radiant intensity of ~10000 J / m^2 / pulse was considered for applications in eye surgery. That 213 nm system produced a region of ablated cornea approximately 0.2 μm deep / pulse and negligible disruption 1 μm below the ablation (Gailitis et al. 1991). Given that the test system had 2000-fold greater intensity than the TUCS laser and produced only relatively shallow damage, we would speculate that the potential damage due to

accidental viewing of the TUCS laser is low. In addition, there is a hypothetical risk of ultraviolet keratitis (colloquially known as "snow blindness") due to long-term exposure to diffuse ultraviolet light. This event is unlikely since diffuse laser reflections have less ultraviolet radiation than direct sunlight, but the possibility is noted here for completeness. Most cases of ultraviolet keratitis resolve within 48 hours without treatment (Brozen and Fromm 2009).

2.1.3 Communications and Control

Communication with the TUCS may be accomplished by either a USB cable or a crossover Ethernet connection. In principle the Ethernet communications port could be set-up to allow the system to operate remotely using the Internet. However, such remote control was never considered for the current work. In addition, we found that the Ethernet communications chip was unreliable at low temperatures and hence we relied on USB communication nearly exclusively. Computer drivers for the TUCS were provided by Photon Systems with their software package and are required for USB operation.

Internally most commands are routed to the primary processor and data acquisition board. This communicates via an internal communications protocol with the power control board for the laser. Due to the initialization and handshaking involved, the TUCS requires approximately 20 seconds after power on before it is ready to operate. Further, there is a substantial and somewhat variable delay on the order of 35 ms between when fire commands are sent to the TUCS and when the firing current is actually sent to the laser tube. Though it was never used, the back panel of the TUCS includes a wire panel with a TTL pulse[e] synchronized to laser firing which could be used by systems requiring precise awareness of the laser response. In practice, we set our instrumentation to integrate over a 40 ms window that was chosen to be significantly longer than the possible jitter created by the firing delay. This guaranteed that the 100 μs laser pulse would be contained in our observation window even though its exact timing was unknown.

The control of the TUCS is accomplished through a Labview[f] interface. Photon Systems provided the initial Labview control software, as well as several version updates. Their software was heavily modified over the years to accommodate our needs and add additional functionality. This section will provide a brief overview of the information flow. Additional details of the current software are described in Chapter 3, and printed code is provided in the Electronic Supplement.

It should be noted that control of the TUCS includes several "black box" modules that were encrypted and locked by Photon Systems. These provide functions such as communicating with the laser hardware and presumably were protected to intentionally keep the users dependent on Photon System's control software. In principle, one should be able to reverse engineer these functions by intercepting all of the traffic flowing across the TUCS USB connection. To date we have not found it necessary to do this, and have simply accepted the use of encrypted commands where necessary.

The communications software begins by initiating a connection to the laser system. The process takes several seconds and is accompanied by an audible change in the TUCS. Before

[e] TTL = time-to-live. A simple voltage spike used for rudimentary analog or digital signaling.

[f] Labview is a common commercial programming language specialized for control of instruments and embedded systems.

being initiated the power system produces a series of soft audible clicks repeated at roughly 1 Hz. During initialization a louder sound is triggered followed by silence, which indicates that the power system is energized. After being energized one is then able to configure the laser system with adjustments to current, voltage, pulse duration, and repetition rate. While these settings can affect total power delivered by the laser, we generally find the default settings to be adequate.

After being initialized, if there is a communications failure between the TUCS and the controlling computer (such as the USB cable coming loose), the current implementation does not provide any means of reconnecting except to power cycle the TUCS and restart the control software. Power cycling is also the primary solution to dealing with any other problems that cause the TUCS to lock up or stop responding.

2.1.4 Phototubes

The original TUCS configuration used 6 Hamamatsu phototubes (4 head-on H6780-06 and 2 side-on H6779-06) and had an internal data acquisition system. In addition, the control software allowed one to adjust the high voltage applied to the phototubes and select one of three different capacitors (47, 470, and 4700 pF). The current from the phototubes was fed to the selected capacitor and read by a 16-bit analog-to-digital (A-to-D) voltage sensor. Adjustments to the voltage and capacitance allowed one to adjust the dynamic range to respond to various sample targets. However, we found that the concentrations of target cells in ice were sufficiently low that we nearly always needed to run the instrument at or near the highest available gain. Unfortunately, at the highest gain setting the thermal noise in the circuit produced fluctuations of 10-30% in the typical signal.

In addition, the characteristic time scale for the capacitor circuit was such that the discharge was not necessarily complete when the system was operated as 10 Hz. This allowed directly measured data to bleed into the dark noise measurements[g] taken between pulses, and partly contaminate the background characterizations. In addition, it appeared that such residual signals allowed cross-talk between channels. Under certain conditions it was routine for a channel's dark noise to report two or three times more counts than when the channel was supposed to be active. Because the firmware running the on board data acquisition system in the TUCS was proprietary and closed source we were not able to fully investigate this phenomenon; however, we would speculate that reading the dark counts on channel 1 immediately after finding a large signal in channel 6 resulted in some of the channel 6 signal bleeding into channel 1. Photon Systems never directly acknowledged these defects in their data acquisition system, but we became aware that subsequent models of their instrument were designed so that each channel had a fully independent A-to-D which would have prevented such crosstalk.

In 2006 and 2007, when we were using the phototubes with the TUCS, we generally adopted an empirical floor model for the background in order to work around the limitations of the Photon Systems measurement system. Thus we treated the lowest 5% of the active data from

[g] Dark noise refers to the counts measured by the readout electronics at times when the laser is turned off. It is expected to capture both instrumental effects such as electronic noise and any ambient light present in the environment. By subtracting the dark noise counts from the total counts produced when the laser fires one would ordinarily assume that the remainder are the direct result of the laser system.

any given run as representing an empirical zero for that channel and focused our analysis primarily on signals that presented themselves as well above that floor. The limitation of this approach is that it made it impossible to meaningfully characterize the bulk matrix of the ice; however, studies of localized impurities – presenting as spikes above the empirical floor – were still possible.

Though a 16-bit A-to-D nominally gives a dynamic range of 65,535 counts, in practice, we observed that apparent saturation did not reach the theoretical maximum. The highest level reported appeared to be 65,280 (corresponding to binary 1111 1111 0000 0000), and apparent saturation behavior seemed to be present at even lower levels. As a result, we decided to treat all phototube results above 64,000 as saturated. We are unclear of the cause of this discrepancy as a typical A-to-D is usually fairly stable and would have no obvious reason to exclude the lower register.

Because of the poor signal to noise, need for complex adjustments to the dynamic range, and difficulties with background characterization, we abandoned the phototube system and replaced it with a photon counter system of our own design in 2008. This is discussed in Section 2.3.

2.2 Optical Elements

The TUCS is designed to accept ½″-diameter emission filters placed in holders in front of the phototubes. The full BFS was designed to accept either the ½″ filter or 1″ filters. All filters used were prepared by Chroma Technology of Bellows Falls, VT. Some of the filters were ordered specifically for this work and some (including most of the 1″ filters) were reused from prior optical experiments conducted by Nathan Bramall (Bramall 2007, Bramall et al. 2005, Bay et al. 2003). The filters used in 2008 and 2009 in the BFS were: 300bp20, 320bp20, 340bp20, 360bp20, 380bp20, 670bp40, and 710bp20[h]. In addition, 6 of the 7 channels where preceded by a 250 nm long-pass filter (250lp) to exclude scattered laser light. Due to the unavailability of a seventh long-pass filter, the channel 670bp40 was shielded with a float glass window[i]. Float glass should be absorbing at 224 nm and have a similar effect to the long-pass filter but would be less efficient. This was intentionally used on a long wavelength channel due to the reduced risk of bleed-through if it was incompletely effective. However, such concerns may be of limited importance. Except for the 300bp20, all other filters used in the BFS were specified by the manufacturer as providing at least a 10^6 reduction in intensity at 224 nm even without the inclusion of the laser-blocking pre-filter. Figure 7 shows the factory-measured transmission spectrum for these filters. The 250lp filter in Figure 7 has the same characteristics as the alignment mirrors used in the TUCS (Section 2.1.1) except that the alignment function relies on its high reflectivity at low wavelength rather than its transmissivity at high wavelength.

The choice of filters is designed to focus on two biological targets, amino acids in the 300 to 380 channels (specifically tryptophan and tyrosine, see Figure 3) and chlorophyll-like

[h] Here a band-pass filter is characterized by its nominal central wavelength and the approximate width of the equivalent square wave. Hence, a 400bp30 filter would be a band-pass filter centered at 400nm with a nominal filter width of 30nm.

[i] Float glass is ordinary commercial glass, usually soda-lime, made by pouring molten glass onto a bed of molten metal (typically tin). It is the primary type of glass used in windows. Because of its method of manufacturing it will generally have more metallic impurities than other kinds of glass.

compounds in the 670 and 710 nm channels. There are several different types of chlorophyll and similar bacterial phototrophic compounds that fluoresce in the 670 ± 20 nm band we are targeting (Bramall 2007). Preliminary observations by Nathan Bramall of ice samples from WAIS Divide suggest that the 670 nm emissions we observe may be dominated by a bacterial source rather than by chlorophyll per se. The 710 nm channel is intended to distinguish phototrophic compounds, which generally peak below 700 nm, from mineral fluorescence, which can also trigger both channels but may be increasing with wavelength at 700nm. As discussed in Section 6.7, the 710 nm channel is almost never triggered except for volcanic ash.

In addition to the optical filters, Photon Systems provided one fused silica ½″ biconvex lens for focusing the 224 nm laser. Only a single lens is used in the entire system because the fused silica is still partially absorptive of light at 224 nm. The full magnitude of the intensity reduction was never characterized but based the performance of other fused silica pieces is plausibly 10-30%. The focal length of the lens is approximately 35.0 mm at 224 nm. As noted by Photon Systems, the index of refraction is strongly wavelength-dependent in the ultraviolet. In the visual range the lens has an apparent focal length of 40.1 mm. Assuming the 224 nm beam is centered on the lens and has an initial diameter of ~3 mm, we find the resulting focus point produces a spot of approximately 0.5 mm diameter (possibly limited by spherical aberration). Depending on the time of scan being performed, the lens may be included or excluded.

In addition to the standard filters, a series of neutral density (ND) filters was also procured that could be used to attenuate the beam. Using an ND1 (10% transmission) or an ND2 (1% transmission) provided an easier way to test the effects of varying laser intensity rather than making adjustments to the laser system controls. It is worth noting that we purchased ND filters calibrated for 224 nm light. ND filters calibrated for visible light would tend to transmit less than rated at 224 nm due to the absorbance of the fused silica substrate.

2.3 Photon Counter System

In 2008 we replaced the internal system of phototubes described in Section 2.1.4 with a photon counter system of our own design. This system was based on equipment previously used by Ryan Bay and Nathan Bramall in various fluorescence and dust logging applications (Bramall et al. 2005, Bramall 2007, Bay et al. 2003, Bay et al. 2005). The basic arrangement is shown in a photograph in Figure 8. It consists of a seven-fold ring of Hamamatsu photon counting modules arranged at a 45 degree angle relative to target focus. These are wired to a Prometheus PR-Z32-EA microcomputer manufactured by Diamond Systems through 7 RS-232[j] serial connections. The microcomputer in turn communicates to the operating laptop through a RS-485[j] connection (which we first connected to a USB converter). The final electronics piece is an onboard power converter that takes 120 VAC and provides 5 VDC and 12 VDC supplies for the computer and photon counters respectively

[j] RS-232 and RS-485 refer to "Recommended Standard" 232 and 485 respectively which refer to standardized binary signaling technology used in computer serial ports, where the standard specifies the number, layout, and purpose of a number of connection pins. RS-232 was the most common serial communications standard used in computers primary to the adoption of universal serial bus (USB) technology, which has now largely displaced it.

The microcomputer uses a 100 MHz 486-DX2 processor and a 64 MB solid state flash-based hard drive on a small secondary board. The computer itself runs a stripped down version of RedHat Linux intended to manage only timing, communications, and disk operations. The custom software to run the system was written in C and originally designed by Ryan Bay for the biospectrologger (BSL) that was used at South Pole in 2004 (Bramall 2007). Unfortunately, the equipment required to update the solid state drive was accidentally destroyed sometime between 2005 and 2007. As a result, we were forced to rely on the software as existed at the time of the BSL. If the solid state drive were to fail at this point there would be no alternative but to rewrite the control software from scratch. Though this creates a dangerous single point of failure, the BSL control software was generally adequate for the task of querying the photon counters and relaying the information to the operating computer. One major limitation, however, was that the microcomputer was programmed to operate only over a 9600 baud[k] connection to the controlling computer. Given the volume of data exchanged this imposed a fundamental limitation of about 12.5 Hz on the operating rate of the photon counter system. At the present time this is the controlling limit on the measurement speed of the BFS. If this software were replaced it is believed that the total system could probably be operated at 30-50 Hz without changes in hardware (except for the raster mode described in Section 5.3, which is limited by the speed of the micromanipulator motor).

Figure 9 shows a schematic of the optical path used by the photon counters. The seven-fold mount and the collars used on the photon counters were custom engineered, while most other components were off-the-shell items purchased from Thorlabs. The collars used to mount the photon counters use O-ring seals to provide a firm light tight seal to the featureless photon modules. The interior of the collar is threaded to accept 1″ retaining rings allowing 1″ optical filters to be mounted inside. As shown in Figure 10, a ½″ optics tube extends from the seven-fold mount towards the target and allows ½″ filters to be mounted inside it. The laser line blocking filters are placed at the very front of these ½″ tubes. The stacked and recessed design has the no direct paths exists that allow the photon counters to see exterior equipment services Hence it would require at least two scattering events for stray laser photons to excite fluorescence in the equipment that would be visible to the counters. As a practical matter, essentially all metals will generate some fluorescence when excited at 224 nm, so isolation by design is critical.

Below the mounting platform, an aluminum “dish” provides a partial shield against stray light (see Figure 16). This dish was originally black-anodized with the intention of absorbing stray light; however, we discovered both that the anodizing process was contaminated with an unknown compound and that the anodization itself was contributing to a fluorescent background. (In particular, aluminum oxide fluorescence provided a background directly interfering with the F420 studies conducted in 2007.) As a result the anodization was removed from the exterior face of the dish. In addition the original 1/2″ hole was expanded to 1 1/4″ so that no portion of the interior surface would be directly visible to the photon counters.

As illustrated in Figure 11, the main viewing area of the photon counters extends to a depth of ~5 mm over which the entire active surface of the photon counter would be accessible to fluorescence emission. Below this, the center of the active surface is visible to a depth of 14

[k] Baud is the same as the number of binary bits per second in this context.

mm, at which depth approximately 40% of the active surface could be reached. Finally, the most extreme edge of the active surface could be visible to a total depth of 29 cm. As the active surface of the photon counter is actually square, despite being mounted in a circular housing, these numbers are approximate and slightly dependent on the rotational orientation of the photon counter. The large acceptance area of this design makes the instrument insensitive to moderate variations in the distance between the ice surface and the emission port (especially over the 5 mm full focal distance), and allows alignment of the ice to be accomplished more rapidly. This contrasts with the design of the TUCS phototube system, which had a visible depth of only a few mm and was extremely sensitive to variation in the range to target.

The 224 nm laser may or may not actually penetrate to a significant depth. In most cases beam dissipation is controlled by scattering on impurities, principally air bubbles. The absorption on impurities and the scattering / absorption against pure ice are comparatively unimportant (Ackermann et al. 2006). The number density of such bubbles can be estimated as ~6 scattering sites per ice crystal. The typical crystal size runs from <1 mm in firn to several cm in the oldest ice (much larger crystal sizes are possible, but not generally present in samples we examined). Using the visible bubble sizes as a guide, one can estimate the effective scattering length as ranging from less than a mm in firn to many cm in the clearest ice. This is consistent with the observation that firn[1] is white and opaque while deep ice is clear or translucent. This scattering enlarges the region of ice illuminated by the laser and can have tangible effects on the strength of the returned signal. This is discussed further in Section 6.3.

2.3.1 Photon counting modules

The 7 photon counting modules made by Hamamatsu come in three different flavors: five HC-135 mod 11, one H9319-02, and one HC-135-02. The HC-135 tubes are legacies from the BSL while the H9319-02 tube was purchased for this project. Each tube has onboard electronics to count the number of photons received and converts that information to a numerical value transmitted over RS-232 to the microcomputer controller. The HC-135 mod 11 tubes use bialkali anodes designed for wavelengths less than 650nm, and are used with the 300 to 380 nm filters. The other two tubes have multialkali anodes designed for long wavelengths and are used for the 670 and 710 nm channels. The multialkali tubes have a much lower work function and hence are subject to much greater thermal noise, with the HC-135-02 tube producing about 10 times as much noise as the newer H9319 tube.

The photon counters divide time into a sequence of bins with each bin either receiving a photon or not. Hence the maximum number of photons that can be counted in any interval Δt is $\Delta t / \delta$ where δ is the fundamental size of the bins. The fundamental clock speed on our photon counters is 50 MHz, giving a fundamental time of 20 ns or a maximum count of 5000 photons per 100 μs laser pulse. Further, for technical reasons, the photon counters only report counts as a multiple of 4, reducing the number of possible variations in output further. This is a smaller range of variation than would be preferred; however, a photon counting system with a faster

[1] "Firn" is the name given to the loosely consolidated glacial material intermediate between snow and ice. It generally consists of small, rounded snow and ice particles compressed into a loose network that has structural rigidity but also provides a continuous network of air channels throughout its volume. Further compression causes the initial ice particles to weld together than close of the air channels in order to form consolidated ice.

fundamental would mean that the pre-existing photon counting tubes could not be reused from prior research and hence require custom electrical engineering beyond the funds available for the project.

In Figure 13 we show the factory-measured counting efficiency of the photon counters as function of wavelength. The plot covers the H9319-02 / HC-135-02 and the default configuration of the HC-135 tube. However, there is no documentation for the "mod 11″ version of the HC-135 which used a fused silica window rather than a borosilicate glass typical of the HC-135 tube. This significantly increases the efficiency at ultraviolet wavelengths. Since we do not have an appropriate light source to calibrate this system in the ultraviolet and factory documentation is unavailable, we estimated the transmission difference by comparing the efficiency of similar HC-124 tubes with UV glass. Unfortunately, it is difficult to know if the currently produced HC-124 tubes will have the same properties as the HC-135 mod 11 tubes manufactured before 2001.

Even given the relatively limited range of variation, the photon counting modules were considered a considerable improvement over the TUCS phototubes. They eliminated the complex tuning of the dynamic range, and at for the lower wavelengths virtually eliminated the dark noise problem. While the phototubes often had a noise level of 2000 counts (out of 65000 max), the lower wavelength photon counters achieved a noise level of 0-4 counts (out of 5000 max). In addition, the photon counters eliminated the major problems associated with channel crosstalk and slow discharging of capacitors discussed above in section 2.1.4. Hence this equipment change allowed meaningful studies of changes in the bulk medium which were not practical previously.

In using the photon counters several new problems were encountered though. First, the reported number of photons would be a systematic undercount if more than one photon arrived during a single 20 ns bin. This Poisson process can be easily modeled via Monte Carlo methods if we assume that photons arrive uniformly during the 100 μs laser pulse interval. In Figure 12 we present a simple estimate of the apparent number of photons as a function of the true number of photons delivered in a 100 μs window. By applying this one-to-one relationship in reverse, one can estimate the true number of photons present as a function of the number observed, though this becomes increasingly uncertain as the reported number of counts approaches 5000. It is important to note that lifetime of the amino acid excitation in proteins is typically of order 1-10 ns (Beechem and Brand 1985), and hence we can generally neglect the possibility of fluorescence signals arriving appreciably after the end of the 100 μs laser pulse. This, however, is not a universal property of matter. Phosphorescent compounds can have light emission delayed by very long intervals from the original excitation, in which case the prompt model is not reasonable (and the apparent number of counts may greatly exceed 5000). In the process of materials testing, some generic glass of unknown composition was observed to have a long emission tail consistent with phosphorescent behavior though none of the biological or metallic samples tested appeared to have that property.

An additional problem with the photon counters is that they may become "charged" if exposed to bright lights, such as overhead room lights, due to a buildup of excess electrical charge within the internal electronics. When this occurs they generate higher levels of dark noise that decays exponentially over a period of time. All of the photon counters do this to a degree but the HC-135-02 counter remains charged for the longest time scale: a period of minutes. This can be countered by allowing the photon counters to sit in the dark for a few minutes before

taking data, and by not using bright lights between data runs. In addition, because a charged photon counter decays in a predictable exponential fashion, the effect can be captured by the dark noise measurements and removed from the data in a straightforward manner. With the photon counter system we routinely take one dark measurement for every 10 active measurements.

Because of the timing jitter in the laser firing, described in section 2.1, we generally set the photon counters to integrate for 40 ms in order to ensure that the 100 μs laser pulse occurs during the window of consideration. The length of the integration window is the only software-adjustable feature in the photon counter system. It should also be noted that because of communication lags in the process querying the photon counters, they are not guaranteed to be totally synchronized so the long integration window also helps to absorb the jitter created there.

In Figure 14 photon counter measurements are shown for the first six channels during an experiment where 20000 observations were taken from a fixed target. Aside from a slight upward trend (presumably related to 30 minutes of UV exposure), most of the measurements are remarkably consistent. However, we also note that for the HC-135 mod 11 phototubes approximately 0.5% of the measurements do not follow the normal pattern and appear to drop out by up to 50%. Such drop-out events appear to be unpredictable and uncorrelated between tubes. The cause of these events is unknown. They are infrequent and so can be largely neglected, but they do suggest that caution must be taken before asserting any significance to negative excursions localized to a single observation by a single channel. Discounting outliers and the slight trend, we note that the counts cluster around the mean value with a standard deviation of 2.2-3.2% depending on channel.

2.4 Mounting and Translation Stage

When at NICL, the whole BFS apparatus is usually cantilevered over a translation stage using a Velmex B6915W1 Elevating Table anchored through the use of C-clamps. Photos of this configuration are given in Figure 15. The translation stage, built by Cymatix, to our specifications, is a 2.5m screw-driven motorized stage with one driven and one free sliding mounting platform. The motor is a cold-rated multi-phase stepper motor originally manufactured by Danaher Motion and modified for cold use by Cymatix. It was controlled by a Parker Gemini GT6K motor controller. The motor is essentially overpowered for our application, but was chosen due to its guaranteed operation at -30 °C. Linked to the stage it operates smoothly at both a very slow crawl and at speeds up to 15 cm/s (though the control software was intentionally capped at 10 cm/s, and ice cores were rarely moved at speeds greater than 7 cm/s). The motor controller requires both 120 VAC and 24 VDC power supplies with the former directed to the motor and the latter dedicated to the internal electronics. The motor controller is highly programmable and responds to text commands through an RS-232 serial connection (Parker Automation 2001).

In order to initialize the motor controller a complex series of instructions must be provided to define the specifications of the motor. The key items and the commands for loading this information are stored in the Labview file *Motor Configure.vi* and current values are enumerated below.

Static Torque: 375 oz-in	Phase Resistance: 2 Ω	DIGNA: 3.5
Continuous Current: 3 A	Rotor Inertia: 402×10^{-6} kg m^2	DIGNB: 0.3136
Inductance: 7 mH	Number of Poles: 50	DIGNC: 1.2523
Hard Limit Option: 0	Electronic Viscosity: 5	DIGND: 0.98
ABS Damping: True	Load to Rotor Inertia: 5	Distance Factor: 196850
Stall Detect Sensitivity: 20	Stop on Stall: True	
Pitch: 1.9685 rev / cm	Velocity Limit: 15 cm/s	

Table 1: Motor configuration variables

As presently operated, the software and hardware must be manually configured to specify the translation stage's initial position and the numerical values associated with its limiting positions. As a result, the control software is solely responsible for keeping track of the stage's position and preventing a collision with the end of the track. This approach requires updating these limits whenever the control system is restarted, such as at the beginning of a new day of scanning. Both the stage and motor controller are capable of accepting limit and home switches, though to cut down on costs, neither was purchased and the software solution was used instead. (For this purpose "a switch" is any mechanical device that causes an electric circuit to close when the translation stage passes a predetermined position. It would probably be straight-forward to implement a home-brew switch for easier initializations and greater security against hard stops, but this has not been attempted.)

The motor controller is not rated for low temperatures and is the only significant portion of the apparatus which has not been operated at -25 °C other than the controlling laptop. The configuration chosen in 2008 allowed the motor controller to reside in a warm antechamber at NICL and be cabled to the motor through a wall. Approximately 50 feet (15.2 m) of cable is presently provided.

In order to carry ice cores, two metal troughs were constructed, one a half-cylinder and one with right-angled walls. Stainless steel was used in their construction due to ~70% lower fluorescent background than aluminum in our materials testing. We note that the plastic troughs routinely used at NICL are entirely unsuitable for our purposes due to high fluorescence. Small pieces of ice could be supported by additional materials placed in the bottom of the trough. One highly effective material was aluminum foil due to the ability of crumpled foil to be arranged into a wide variety of forms in order to support irregularly shaped ice.

2.5 Micromanipulator

During 2009 a large number of detailed raster scans on small pieces of ice were conducted at Berkeley. For this work we borrowed a Sutter Instruments MP-285 motorized micromanipulator from the Andrew Westphal group at Lawrence Berkeley National Lab. This computer-controlled three-axis stage has a 1″ range of motion on all three axes though we only used it for two-dimensional scanning. This system was less than ideal for our purposes because a 1″ range of motion was smaller than would be preferred given that our ice samples were typically 3" x 5". The micromanipulator was designed for movements with 0.2 μm precision, and had a top speed of only ~2 mm/s. Further, the motion control system was not designed to

communicate with the laptop while a move was in progress, so it was necessary to stop before each pulse rather than pulsing the laser during a continuous motion. As a result of these design factors, the stage became a limiting factor in the scan rate with detailed scans of a single square inch typically taking 30 minutes.

The stage is not officially rated for low temperatures, but we found no significant difficulties operating it at -20 °C. We did however apply a low-temperature grease to the exposed gears. According to Andrew Westphal, grease is necessary to prevent wear and deterioration of the gears; however, their standard grease became highly viscous during low temperature trials and hence was not considered acceptable. The specific stage we used had just been returned after being refurbished by the manufacturer and so there was no pre-existing grease on the gears. In addition, the motion controller for the stage occupied a large computer box. It is unknown if this controller will function at low temperature, and under an abundance of caution we chose to keep it warm by placing it at the bottom of the warm box described in Section 2.6.

To work with the micromanipulator, an improvised platform was created by disassembling a wire frame box and attaching it to a hook bolt with thin wire. This configuration is shown in Figure 17. The platform was then automatically moved under the BFS using a modified version of the Labview control software (Section 3.7). Typically the laser beam was focused into a ~0.5 mm diameter spot and the raster scan was conducted with 0.4 mm resolution. Experiments with higher precision scans suggest that this level of detail is about the best achievable with the BFS system and presumably limited by the laser focus. Data from these scans are shown in Section 5.3.

2.6 Miscellaneous Equipment

In order to operate the BFS system at low temperature, some additional miscellaneous items deserve mention. During the 2008 and 2009 trips to NICL, the control laptop was operated in a warm antechamber and communications to the BFS was accomplished by running wires through a port in the wall. To accommodate the distance and number of connections necessary, a heated USB hub was placed in the cold room. This hub was sold as a novelty USB hub / coffee warmer and has an internal heating coil which is active when plugged in and a switch is latched in the on position. The USB portion of the hub does not work effectively until the heater has been allowed to run for a few minutes. This solution was readily effective, whereas USB hubs designed to operate below 0 °C are not generally available and would have been far more expensive.

Secondly, at times we used a custom warm box to allow a laptop to be used in the NICL cold room. This was generally necessary when aligning the laser system as power sensor feedback needs to be immediately visible to the person performing the alignment. The box was also used when performing the two-dimensional scans described in Section 5.3. The warm box, designed by Ryan Bay for use with laptops in field camps at Antarctica and Greenland, consists of a heater in an insulating cargo container pumping warm area below a laptop that has been placed in a Lucite and metal enclosure. A movable Lucite flap allows the operator's hands to control the keyboard. When used, it is recommended that the laptop be powered by mains electricity rather than its battery as reduced temperatures tend to reduce battery performance. It should be noted that the capacitance based touchpad used by most laptop will not respond to cloth gloves. However it will respond if an outer layer of polyethylene gloving is present.

Alternatively, we have used a track ball as a substitute control interface which works effectively at low temperatures. If allowed to become cold, the laptop screen will first go dim (due to decreased illumination from the backlight) and then eventually the laptop will stop working entirely. At times when this has happened by accident, the laptop fully recovered after being returned to room temperature; however, such incidents should be avoided due to the possibility of permanent damage.

When transferring electronic equipment or rust sensitive metal implements from a cold environment to a warm one, substantial care should be taken to avoid condensation. Having being chilled well below 0 °C, all surfaces of the equipment will rapidly attract condensation out of the air if transported to a warm environment unprotected. Standard operating procedure is to enclose large items in garbage bags (often two layers) and small items in sealable Ziploc bags. This allows the equipment to warm up before being subjected to warm air. Particular care should be taken with respect to optical filters as condensation on these filters may in some cases cause permanent damage.

3 Labview Control Software

This section discusses the Labview control software used at NICL in 2008 and 2009. Other software versions, often adapted to specific tasks, will not be discussed in detail. In particular, the details of the TUCS with phototubes control software will be only briefly mentioned though it should be noted that the original TUCS software had a very different internal program architecture than the BFS software (discussed in Section 3.8).

The BFS software deployed at NICL operates on Labview version 8.0 for which UC Berkeley has a site license. Labview, developed by National Instruments, is a deeply multi-threaded programming language with specializations for instrument control and embedded systems. The BFS control software is based in a file denoted simply *Merged Controller.vi* and controls three essential systems simultaneously: the TUCS 224 nm laser, the photon counter microcomputer interface, and the translation stage motor controller. Each of these is connected to the laptop via a USB[m] connection though both the motor and microcomputer are converted to a RS-232 serial connection by means of two USB-to-serial converters.

The main software's user interface is organized into a series of panels designed to accomplish distinct tasks. The list below identifies the various control panels and their hierarchical relationship:

Control Window – The topmost view (Figure 18)

- Main Control Panel – The tabbed frame where most controls and frames are located
  - Initialization Panel
    - Communication Parameters Panel – Startup screen where communications settings must be provided and the very first initialization command is entered.

[m] "USB" stands for "universal serial bus" and is a ubiquitous computer technology that has displaced the older RS-232 based connections in modern computers.

        - "Frankenstein" Parameters[n]
        - High voltage – turn on/off the high voltage in the photon counters or query the current state.
        - PMT control – settings and test options for the photon counters
        - Shut Down – disables the photon counter microcomputer (system requires power cycling to reactivate after a shut down event)
        - Terminal – open command line for sending commands to the photon counter microcomputer.
    - Laser Control – configures and tests the laser status (Figure 19)
    - Data Logging – window used for scanning (Figure 20)
    - Configuration – miscellaneous configuration settings (Figure 21)
- Motor control panel – Feedback on the translation stage's current position and rate of travel and controls for repositioning the stage.
- Timing feedback panel – Statistics on the amount of time spent scanning (not used in 2009)
- Indicator lights – various diagnostic lights always visible
- Stop button – Kill button that attempts to immediately stop all operations and terminates the Labview session.

3.1 Communications Panel

Immediately after starting the program, one is shown the communications panel (main part of Figure 18) and is asked to input the corresponding serial port numbers for the three components (referred to as "COM" port numbers in the user interface). Since the instrument does not have any way of telling whether a COM port is in use, it may take some effort to locate the correct communications settings. One effective approach is to use Hyperterminal – a basic terminal client usually included with Microsoft Windows. Hyperterminal does have the ability to automatically detect connected ports. By adding connections one at a time and checking the list of available ports, it is possible to identify the port associated with each device. It should also be noted that the COM port numbers associated with a USB-to-serial converter will often change depending on which USB port is being used, so one may save time by being consistent about which ports are used for each connection.

Once the ports are correctly identified, the "Start Communications" button will attempt to initialize the TUCS laser, translation stage, and photon counters. The three indicator lights will illuminate. Only the TUCS light verifies a successful connection. The other two lights will illuminate when the connection is attempted but do not attempt to verify that it was successful.

3.2 Frankenstein Communication Panel

After the connection is initiated, the next stop should be the "PMT Control" on the "Frankenstein Communication" panel. This should be used to set the photon counter integration time (typically 40 ms) and verify that all seven channels are receiving signals.

Under normal start up conditions, no other actions are necessary. The "High Voltage" tab allows one to activate or deactivate high voltage to the photon counters. Under normal

[n] "Frankenstein" is the name used internally for the photon counter rig portion of the BFS.

operating conditions the high voltage is automatically turned on and off during data logging, and it is not necessary to manually modify turn this setting. However, the high voltage may be manually applied for diagnosing problems independent of data runs.

It is important that the high voltage not be activated unless the instrument is in a darkened environment. Exposing an energized PMT to direct room light can potentially damage the tube. Accidental and brief exposure to room light will leave the tube "charged" and require several minutes of rest in a dark environment before the dark noise returns to normal levels.

3.3 Laser Control Panel

The "Laser Control" panel, shown in Figure 19, allows one to test and configure the laser settings. The primary chart is a time series of the current applied to the laser tube and the power received at the internal power sensor during the last laser pulse, see Figure 6 for an example reading. The "Laser Energy" box and vertical indicator will denote the estimate of the integrated total power delivered by the laser in μJ. (See section 2.1.1 for cautions regarding the questionable reliability of this measurement.) In the event that the initialization of the laser was to fail, the laser energy would read -1.

The "Fire Laser" button can be used to trigger a single pulse of the laser, or setting the repetition rate can be used to start a continuous series of pulses. The "Bus Voltage" and "Current" can be adjusted to alter the power delivered to the laser, but in our experience the default settings are reasonable and variations from this make relatively little difference. The "Ontime" option determines the duration of the laser pulse. For most applications we also find that leaving this at the default 100 μs makes the most sense. Durations longer than 100 μs per pulse are not allowed by the laser controller.

The primary utility of the laser control panel is to test fire the laser while making adjustments to the alignment of the laser tube or the subsequent optics (see Section 2.1.1). By operating the laser at a low repetition rate while moving the optical elements, one can quickly determine the impact of one's adjustments both as measured by the onscreen power reading and by following the path of the laser as changes are made. A warm box (Section 2.6) is used to make readings available when alignment must be performed at low temperatures.

3.4 Data Logging Panel

The "Data Logging" panel illustrated in Figure 20 is used to conduct scans and collect data. At the beginning of a logging session, and optionally at other times, one is expected to specify a file into which data will be saved. If the file already exists, new data is appended at the end. For each scan the user provides a description, any long-form notes, a start depth and a stop depth. In addition, each scan is labeled with a run number. This number is automatically incremented with each scan, and only needs to be changed if one opens a file that has already been used. Ordinarily notes and all other comments are added to the file at the beginning of the scan, but notes may optionally be added at the end of the scan using the indicated button. The two charts record the time/depth sequence of measurements (left panel) and the current spectral shape (right panel). Toggles at the upper left adjust which channels are displayed (unselected channels display as zero); these functions only update the display when scanning is active.

The first four buttons at the upper right further adjust the on-screen displays. "Use Background" causes background counts to be subtracted from the scan before being displayed.

"Use Efficiency" scales the individual displayed channels by filter efficiencies stored on the "Configuration" page. "Use Energy" scales measured counts by the associated reading on the internal power sensor. "Position Plot" toggles the left chart between a mode where it displays a time series of measurements and a mode where it displays measurements versus depth in core.

The final button "Automate Motion" controls whether or not "Begin Logging" should automatically advance the stage across the entered length of the core and then return. By turning off the automate setting one can manually control which locations and speeds are scanned. Under most core scanning circumstances, automate should remain enabled. Assuming the system is operating in this normal mode, the scanning stage will begin in its "Home" position, which is located at the far edge of the stage and is intended for adding and removing ice cores. Prior to beginning a scan one would load the core and enter the start and end depth for the length of ice being examined. Following this, pressing "Make Ready" advances the start of the ice to a position ~3 cm from the laser emission port. At this position the ice is partially below the "dish" of the photon counter rig (see Figure 16) and allows the user to level the surface of the ice and adjust the height of the instrument. Finally, pushing "Begin Logging" causes the laser to start firing and the ice to slowly move under the apparatus. When the ice reaches the end of the scan length, the laser is automatically disabled and the ice rapidly returns to the "Home" position. At any point during a scan, pressing "End Logging" will abrupt stop the laser and the translation stage.

The structure of the data file generated by scanning is discussed in Section 3.9.

3.5 Configuration Panel

The last of the four main panels (Figure 21) is a catch-all for configuration information.

- Channel Centers – can be used to record the center of the filter bands, which will then be recorded in the data file. This information is not otherwise used in the operation of the device.
- Efficiency Factors – can store information about the transmission efficiency of the filters. It is used for visual displays if "Use Efficiency" is enabled to scale the "Data Logging" charts (Section 3.4).
- Measurements per Background – specifies how many real measurements should be made between dark noise measurements.
- Laser Firing Delay – specifies how many milliseconds should pass between asking the laser to fire and asking photon counters to begin reading. This captures the timing jitter in the laser system. This value should not be changed from 30 ms unless the hardware is modified.
- Position Set / Send Position Set – this option tells the motion controller that the stage is currently at the specified position in cm. Typically a meter stick will be taped next to the translation stage and used to specify the reference position. The motion controller will remember this position set as long as it is powered. This command should always be used when the system is first configured before attempting to translate the stage.
- Translation Stage Configuration
    - Max translation – the reference position in cm corresponding to the farthest position the stage may be moved before hitting the end of the track.

    - Min translation – the reference position in cm corresponding to the minimal position the stage may be moved before hitting the end of the track.
    - Home position – the position, near one end, used for loading and unloading ice cores.
    - Ready position – the position, a few cm from the laser port, where the core should be positioned for leveling the core and adjusting the vertical offset.
    - Additional edges – the amount of additional travel that should occur at both ends of the core to ensure that the full length of the core is observed even if the length measurements and positioning are imprecise.
    - Scan speed – the translation speed at which automated scans should occur.
    - Reset speed – the speed at which the translation stage should return to the home position
    - Max speed – the maximum speed that users are allowed to tell the stage to move at.
- Scan Reverse – If unchecked, increasing positions on the translation stage correspond to moving towards the motor; otherwise, increasing positions move away from the motor.
- Drive Reset – Reset and reinitializes the motor controller. Generally not needed.
- Clear Coms – Flushes the communications buffers for each parts of the system. This is recommended as a potential solution following any communication problem.

3.6 Motor Controller Panel

Located below the main panel is a permanently visible "Motor Controller" panel (Figure 22) that allows the direct manipulation of the translation stage. In the lower half of the panel are adjustable sliders to specify target positions and velocities. At the upper half of the panel are indicators of the current position and velocity. Further, on either side are preprogrammed settings for commonly useful positions and velocities.

One should be aware that changes to the target position or velocity are immediately applied. The feedback displays are also continuously updated whenever the stage is in motion. An indicator light next to the panel shows when the stage is moving. A second indicator is activated if there is read error in determining the position. This condition is generally uncommon, but does occur about once every few thousand measurements. In the event of a read error, a value of zero is recorded for the position and velocity.

3.7 Micromanipulator Variant

A variant Labview program, *Merged Controller for Raster Scans2.vi*, is functionally identical to the system described above, except that the motor controls for the translation stage are replaced with a control system for the micromanipulator described in section 2.5. In this case there are three position sliders and the velocity setting is fixed on the configuration page. Toggle buttons are used to decide which of the axes should be scanned over.

Unlike the large-scale translation stage, no feedback is available from the micromanipulator while moving so its position indicators will only update when the manipulator stops. One should also note that the communications will time out if the stage takes more than 10 seconds to reach its final destination, so at slow speeds one should consider making large

translations in multiple steps. In addition, movements of the micromanipulator occur only when the move button is pushed rather than being automatic whenever the slider is moved.

3.8 Labview Programming

The backend for the *Merged Controller.vi* consists of the typical Labview programming language block diagram structures. The details of this code are archived in the Electronic Supplement, but this section provides a schematic high-level overview.

Figure 23 shows an overview of the control software and its principal module. In the current design there are 6 top-level threads running in parallel:

- Event Manager – This is the thread responsible for reacting to interactive feedback from the operator, such as buttons being pushed.
- Main Panel Controller – This thread provides the primary functionality.
- TUCS Feedback Loop – This thread is dedicated to listening for data coming from the TUCS laser system and updating the associated indicators and values in software accordingly.
- Motor State Loop – Continuously queries the motor controller and updates the display regarding its speed and position.
- Timer Loop – This thread tracks the amount of time elapsed for the purpose of ensuring ice core handlers don't spend unreasonable amounts of time at low temperatures.
- Performance Tracker – Times various aspects of the scanning process to identify bottlenecks (only really used in 2008).

The Main Panel Controller provides the bulk of the processing. It has two initial branches corresponding to whether the "Initialization" and "Data Logging" tab is selected on the main control panel. As shown in Figure 23, the Data Logging consists of two initialization steps followed by an alternation in software between performing motion control and performing data collection.

Data collection can be further subdivided into a sequence of principle tasks steps, which begins with sending a command to fire the laser and read the photon counters. This provides the laser pulse and accompanying measurement. After each pulse, the software then waits up to 50 ms for additional power information to be returned from the TUCS. Once this data is returned, it is added to an internal buffer and to the visible charts. Lastly, when the buffer reaches at least "Data Buffer Size" number of measurements they are written to the hard disk and the internal buffer reset. Using an internal buffer avoids hard drive related input-output bottlenecks.

3.9 File Format

The results of a scan are stored as columns of data in a plain text format.

At the start of each scan is a header which records:

- The current date and time
- The scan description
- The contents of the "Notes" field when the scan was started

- The centers of the filter bands (nm)
- Several photon counter diagnostics
- The photon counter integration time (ms)
- The laser firing delay offset (ms)
- The specified number of measurements between dark noise measurements

Following the header, each line of data records:

- The run number
- The depth of the start of the ice core segment (m)
- The depth of the end of the core segment (m)
- The current inferred position on the core (m)
- The velocity of the translation stage (cm/s)
- The output of the seven counters during the laser pulse
- The output of the seven counters during the last background measurement
- The energy of the laser as reported by the internal sensor (μJ)
- A flag of 0 or 1 to denote a timing read error (1 is the error condition)
- The actual laser firing delay (ms)
- The current time (seconds since 1970)

The variant of the control software for the micromanipulator has three fields for inferred position (x, y, and z) and no entries for velocity.

3.10 Original TUCS Code

It should be noted that the original TUCS code, *C7ver7-7chTUCS.vi*, had a very different implementation model. One thread was allocated to sending commands to the laser system and a parallel independent thread was responsible for receiving responses. Rather than allowing actions to interrupt existing behaviors, the send process was implemented as a single monolithic thread using a command queue to preserve first0in, first-out ordering of instructions. This avoids problems with race conditions, but means that every control panel behavior has to be associated with either sending or receiving information. Given the increasing complexity of the BFS, it was decided to abandon this approach when merging the laser with the photon counter system.

4 Analysis Stack

This section will describe the approach to processing and normalizing data from the BFS collected in 2008 and 2009. Older data was processed in similar ways but with variations appropriate to differences in the instrument construction. Sample source code for the processing discussed in this section is provided in Appendix 10.2.

New data sets are first evaluated for data integrity. Problems such as repeated run numbers were removed and issues recorded as notes in the data files were addressed. The most common correction addressed through post-facto notes were incorrect start or end depths, often a result of miscommunication between the person loading the ice core and the person entering the depths. The notes were also used to record cracks and other ice defects which should be avoided

during later analysis and interpretation of the core. After this, runs that terminated with significantly less data than expected were removed. In most cases an absence of the expected amount of data indicates a communications failure with one or more components leading to an early abort and usually a subsequent rerun.

Next, the motor position data was smoothed to eliminate jitter caused by timing fluctuations (since the motor the reported position only every 100 ms and the laser was operating at ~12 Hz, variations in the response sequence had to be expected), and at the same time we interpolated to fill in any missing position data caused by motor communications errors. Such errors were observed approximately once for every ten thousand samples collected. Following this, we deleted any measurements where all channels reported zero counts, generally indicating a laser timing or counter communication issue. Such events were very rare. Also removed were events where the internal diagnostic for laser timing indicated that the photon counters may not have witnessed the full pulse. These misfires occur about once every thousand measurements.

Next we attempted to shift the reported positions of all data so that the first and last measurements made on the ice core fell as close as possible to the recorded start and end depths. It is easy to detect the start and end of the ice core as the counters will drop to near zero when the beam is being transmitted into open air. The maximum allowed translation was ± 2 cm. Lastly, the records were truncated to remove any measurements taken from the open air.

Following this, a record of true counts was created by subtracting the background dark noise rate. This was further rescaled by using the saturation function described in Section 2.3.1 and illustrated in Figure 12. Here, we implicitly assume that photons are uniformly distributed in time when modeling the saturation function. This is consistent with observations of photon counter response, but inconsistent with the timing data reported by the internal power sensor. As discussed in Section 2.1.1, it is our belief that the timing data generated by the power sensor is not reliable. In the absence of an alternative timing measurement, an assumption of uniformity seems the most reasonable choice and matches the current pulse. Also note that the dark noise background, which accumulates over the whole 40 ms integration time, is not affected by the saturation generated from the 100 μs laser pulse, and hence the background subtraction must occur prior to saturation rescaling.

Next the data is rescaled by the laser power estimated from the integrated value of the internal power sensor. This produces a normalized intensity that should be independent of laser performance, but also assumes that the internal power sensor is proportional to the true laser power. Given the discussion of Section 2.1.1 even that assumption may be subject to some doubt; however, observations of the WDC06A data (section 5.1) do appear reasonable when scaled with the assumption of linearity.

At this point all bad measurements should have been removed and the good data has been reprocessed to remove dark noise, saturation biases, and other effects. The resulting values should be linearly proportional to the abundance of fluorescent compounds in the ice.

The next step is to rescale the photon abundances at each counter to make an estimate of the true photon abundance at the emission site by accounting for the differences in transmission and counting efficiency for the various wavelengths considered. Ideally this will allow the true spectral shape to be determined for comparison to laboratory standards and other measurements. The primary method used throughout the majority of the document to account for transmission effects is to rely on a convolution of the measured filter transmission characteristics and the counting efficiency. The resulting theoretical response function as a function of wavelength is

shown in Figure 24. Integrating across wavelengths produces a relative measurement of efficiency for the seven channels noted in Table 2.

Wavelength Center (nm)	Theoretical Efficiency
300	4.8%
320	8.2%
340	12.1%
360	8.9%
380	11.9%
670	1.42%
710	0.98%

Table 2: Estimated acceptance efficiencies for the BFS channels

We note that the theoretical efficiency of the long wavelength channels is much lower than the other channels due primarily to the much poorer counting efficiency at the long wavelengths. Given these efficiencies and noting the 0.0789 steradian acceptance of the counters, it is possible to express the BFS measurements in terms of emitted photons per 20 nm filter band per 1 μJ excitation. These are the conventional units that will be used in describing BFS data. As noted in Section 5, typical intensities show $10^6 – 10^7$ photons generated per 1 μJ pulse. As 1 μJ at 224 nm has $1.12*10^{12}$ photons, this would imply a conversion efficiency of roughly 1 in 10^5 fluorescence photons detected per excitation photon. Tryptophan and tyrosine have an expected quantum yield of 13% and 14% respectively (measured in room temperature water; Lakowicz 1999), however the much lower conversion rate is mostly a result of few photons actually reaching microbes. At 10^4 cells / cm^3, a 1-micron cell diameter, and 1 cm of visible emission, the simple geometry argument (not including scattering) suggests that only 1 in 10^4 laser beam photons will intersects a microbe within the visible emission region. This encounter factor, combined with the quantum yield, makes the conversion efficiency appear reasonable to order of magnitude.

4.1 Uncertainty Analysis

The uncertainty analysis per measurement follows directly from the analysis chain described above. Each reported set of counts (both measured and background) is assigned an initial uncertainty that is the larger of either 3% or the square root of the number of counts. The square root estimate is based on the assumption of counting uncertainty associated with Poisson statistics. By contrast, a 3% floor is used as a limiting uncertainty based on the observed variation when attempting repeat measurements (see for example Figure 14 and Section 2.3). These two approaches intersect at 1111 counts with 3% applying above and the square root applying below.

These initial statistical uncertainties are then allowed to propagate forward through the analysis chain to create an estimate of the statistical uncertainty in the final measurement. Aside from applying scale factors, only two adjustments to the statistical error are necessary. First, the uncertainties in signal and background, assumed to be independent, add as the square root of the sum of their squares during background subtraction. Secondly, at the saturation adjustment step

the adjustment function leads the propagated error to become asymmetric with the upper bound being affected more than the lower bound due to the non-linearity of the saturation correction. The noise in the internal power reading was considered as another possible source of statistical error, but examination of the shot-to-shot variation in the power reading suggests this error is no more than 0.45%, which we regarded as essentially negligible. From these considerations we find that the statistical error per measurement is typically 3-10%.

The remainder of the analysis chain, such as the transmission coefficients, simply introduces scale factors. Any error that may exist in these factors is essentially systematic rather than statistical since it does not affect the comparison of separate measurements. Where included, plotted error bars in this thesis will be only statistical unless otherwise noted. Unfortunately, the systematic errors are largely unquantifiable by theoretical means since they depend on factors such as factory specified transmission characteristics that have no described uncertainty.

Given that difficulty, a natural recourse is to check the calibration of the measurement by comparison to a standard of known composition. With the TUCS in 2006 and 2007 we examined ice intentionally doped with *Escherichia coli* bacteria and/or bacterial endospores. These observations were similar to results obtained with the TUCS working directly with ice cores. At that time we found that many of the ice core spectra were broadly similar to the prepared biological spectra (Figure 25), though with enough dissimilarity to suggest further study was needed. From the similarity and work by Bramall (2007), we concluded that the 224 nm fluorescent excitation was likely to be effective at seeing microbes in ice. However the instrumentation used at that time had a variety of problems (see Section 2.1.4) and we generally expected to accept a larger margin of uncertainty than with the BFS, so the constraints obtained at that time were weak. In addition, the similarity between test samples and real samples only establishes that the technique is plausible; it doesn't provide an absolute calibration standard. Ideally we would like to use an alternative UV spectrofluorimeter with a proven track record to create calibration standards from which the transmission coefficients can be verified. To date this has not been available (see Section 7).

5 Fluorescence Scanning Results

5.1 2008 NICL Trip – WAIS Divide

During a two week trip to NICL in 2008, we produced 452 one-dimensional scans sampling 378.8 m of the WAIS Divide (WDC) 06A ice core. This represents 66% of the 576 m of WDC06A archived at NICL at that time. The sections scanned excluded core fragments less than 65 cm in length, and half of the ice cores above 88 m.

The U.S.-led WDC Coring Project is in the process of collecting the newest deep ice core from a WAIS Divide site (79°28.058'S, 112°05.189'W) in West Antarctica. The site was chosen for its high snow accumulation, approximately 20cm / year, and is intended to provide an expanded record of Antarctic conditions during the last ~150 kyr for comparison to the similarly expanded Greenland cores (Morse et al. 2002). The top 114 m of the WDC06 core was dry-drilled with a 10 cm bore. Following this, the existing borehole was reamed with hot water to accommodate a 12.2 cm bore and filled with a borehole fluid consisting of a mixture of two parts Isopar-K and one part HCFC-141B. Isopar-K is a mixed composition petroleum distillate having

a specific gravity of 0.761 g / cm^3. HCFC-141B is a synthetic densifier also known as dichlorofluoroethane and having a specific gravity of 1.227 g / cm^3. New manufacturing of HCFC-141B is banned under the Montreal Protocol on Substances That Deplete the Ozone Layer[o], so all HCFC-141B used at WAIS is reclaimed material from pre-existing industrial stockpiles and uses. In industry, the primary non-destructive use of HCFC-141B is as an industrial solvent, where it has historically been used as a degreasing agent and in the cleaning of electronic components after soldering. The reclaimed HCFC-141B appears visually as a pure substance but may contain unknown residues associated with prior use. This drill fluid, designed to match the density of ice, will be used to continue drilling operation until near bedrock. At present, there are no plans and no environmental permit to extend the WDC core into the bedrock.

A gross summary of the collected data is shown in Figure 26 as the per-core segment averages of the 320 and 670 nm channels. These channels are intended to be most diagnostic of amino acids and chlorophyll-like fluorescence respectively. As can be seen, the largest scale feature is a largely monotonic fall-off with depth that occurs most rapidly in the top 120 m and less rapidly below this.

In Figure 28, representative examples of individual measurements are provided. For a full-meter core, approximately 1300 such measurements can go into each segment average shown in Figure 26. The detail plots reveal several additional features. First, the apparent response is largely uniform over much of each core segment, suggesting that the properties being observed are relatively consistent from year to year. That said, there are also a number of interesting features, such as the 10 cm bump visible at 107.6 m in Figure 28. In Figure 29 we also highlight a narrow spike at 27.8 m extending only a few mm. It is assumed that the narrowest features correspond to local excesses of microbes (see Section 5.3). Fluctuations such as these occur throughout the core and are potentially interesting targets for removal and further analysis, though it will be important to exclude contamination or optical biases (see the discussion in section 6).

The second-clearest feature in Figure 26 is the variability in the 320 channel below 114 m. This is a result of contamination by the drill fluid used in retrieving core segments below 114 m. This contamination was obvious even though the scanned sections were from a planed interior surface with approximately ~5 cm of beam travel separating the target surface from the exterior. Subsequent review concluded that drill fluid was migrating from the exterior surface to the interior cuts during the several weeks between when the interior cut was made and when we examined the core. It is unclear if the migration occurs primarily via a liquid phase or a vapor phase. A small study of ours in 2007 suggested that Isopar-K residues (one half of the WAIS drill fluid) have an approximately 1-hour half-life to evaporation at -25 °C (Figure 27). This suggests a low enough vapor pressure that residues do not immediately dissipate, but also a high enough vapor pressure that the drill fluid can migrate within the sealed bags used for storing ice cores. Related work of ours in 2008 showed that the level of drill fluid associated fluorescence was roughly 10-20 times higher on the exterior core surfaces than on faces cut from the interior

[o] Yes, that's right, the WAIS drilling project is bringing more than 10000 gallons of a volatile ozone depleting compound directly to Antarctica. On top of which, since it can no longer be manufactured, the market for HCFC-141B is highly constrained. The WDC purchases consumed so much of the elasticity in the market that the price quadrupled leading directly to cost overruns. Not exactly the best choice that people have ever made.

of the core. In addition, there was also compelling evidence that drill fluid was being trapped under the plastic netting used to secure the core and hence the netting pattern led to exaggerated hot spots for drill fluid residues. In turn, such trapping of drill fluid appears to have caused the WDC ice core to retain significantly higher levels of fluid than the comparable GISP2D[p] ice core. In 2009, detailed two-dimensional scans (described in section 5.3) led to the conclusion that drill fluid on the outer surface had typically penetrated to a depth of 2 to 5 mm and become strongly fixed in the ice. By contrast, the lighter re-deposits on interior cuts reached only 1 mm or less in penetration. Based on these drill fluid contamination issues we decided to focus on dry-drilled cores in 2009. When it is necessary to examine wet-drilled cores, the surface considered should be freshly cut as recently as possible. Or if not possible to obtain a core just after cutting, then the surface should be replaned to a depth of at least 1 to 2 mm.

5.2 2009 NICL Trip – GISP2, Siple Dome, WAIS, RIDS, Vostok, and South Pole

During a one week trip to NICL in 2009, we examined selected ice core segments from eight different ice cores collected in both Greenland and Antarctica.

[p] GISP2 refers to the Greenland Ice Sheet Project 2, which collected a series of cores from the summit of Greenland in the late 1980s and early 1990s. The longest of these cores was GISP2D which extended over 3000 m and slightly penetrated into the sub-glacial bedrock.

Ice Core	Location	Number of Pieces	Details
GISP2D	Greenland summit (72°36'N, 38°30' W)	5	Deep segments, unplaned, wet drilled.
GISP2E	Greenland summit (72°36'N, 38°30' W)	6	Shallow core, dry-drilled, planed and unplaned comparisons
RIDS	Ross Divide Ice Shelf, Antarctica (77°44"S 116°20'W)	3	Dry-drilled, shallow core, planed and unplaned
Siple Dome	Antarctica (81°39.53'S 148°48.72'W)	10	Wet drilled, unplaned
South Pole 04 Hole 5	South Pole (90° S)	5	Dry-drilled, some planed, some unplaned
Vostok 5H	Antarctica (72°28’ S 106°48’ E)	10	Dry-drilled auxiliary core, unplaned
WDC 05A	WAIS Divide (79°27.777’ S 112°05.160’ W)	5	Planed, dry-drilled
WDC 06A	WAIS Divide (79°27.775’ S, 112°07.422’ W)	8	Planed and unplaned, wet drilled.

Table 3: Ice core sites scanned in 2009

The primary goal of this study was to look for similar fall-offs with depth of the fluorescence in the top ~100 m at other sites. Secondary goals included looking at the impact of planing the surface as a means of removing drill fluid and other contaminants, and testing the BFS as a detector of volcanic ash.

The resulting data is summarized in Figure 30. As with the 2008 data we found that the fluorescence signal was strongest at shallow depths and fell off to roughly uniform level by ~120 m depth. This broad pattern is consistent across all of the ice cores examined suggesting it is likely to be a universal property of the fluorescence signature that can be expected from ice cores. This will be discussed further in Section 6.3.

5.3 Two-dimensional scans

In 2009 we used the micromanipulator stage (described in Section 2.5) to create two-dimensional scans of selected ice core samples. The samples examined where a combination of old GISP2 samples left over from prior work (Tung et al. 2005, Tung et al. 2006) and stored in our freezer, together with new WDC06A samples which were cut from the core and delivered to us by NICL. The WAIS samples, each spanned 5 cm in core depth and had center positions of 16.6, 31.0, 52.85, 64.9, 84.11, 98.6, 139.51, 221.6, 320.4, 376.47, 455.7, and 530.58 m. These depths were chosen based on a review of the 2008 data. Eight of the depths were intended to represent normal, typical ice, while the remaining four samples (52, 84, 221, and 320 m) were selected because they were associated with unusual positive excursions in fluorescence intensity. The six pieces above 100 m came from the dry-drilled portion of the core and were significantly

smaller than the six lower wet-drilled pieces. Figure 31 provides photographs of representative pieces of both kinds.

The ultimate goal with these samples has been to perform wet biology to characterize the microbial types and abundances directly. This wet biology program, in collaboration with Nathan Bramall of NASA Ames, is only just beginning and unfortunately definitive results are not yet available (see Chapter 7). However, we can gain insights from the detailed scans of these pieces.

While the scans along a single vertical strip at NICL used an unfocused beam with a spot size up to 4 mm in diameter, the raster scans intentionally focused the beam to ~0.5 mm diameter in order to maximize the available detail. Coupled with the focused beam, we found that a 0.4 mm step size seemed to maximize the available detail and kept the scan time down to approximately 30 minutes per square inch. Scans were conducted in the cold room on the 5th floor of Latimer Hall at UC Berkeley.

Figure 32 shows a selection of the resulting raster scans. As can be seen these also show fluorescence intensity varying with core depth in a manner consistent with the observations made in Figure 26. Secondly, we note that some of the scans show small-scale heterogeneity and features. We assume that the localized spikes are generally caused by isolated impurities, most probably conglomerations of microbes.

Of note, the highly localized structure of the impurities makes it unlikely that two observers scanning slightly displaced parallel segments of the same ice core would report a similar pattern. This was also observed during the TUCS work, where in several cases we attempted to make parallel scans of the same ice core with tracks displaced by 5-10 mm from each other. In general, the pattern of spike-like details showed little to no similarity amongst the parallel tracks (Figure 33). This limits the usefulness of highly focused studies in understanding ice cores since many sharp features will reflect low-probability encounters with localized impurities rather than large scale trends which would be of general interest. The desire to capture big-picture information rather than fine details was a key motivation in deciding to use a less focused excitation beam with the BFS in 2008 and 2009 rather than the highly focused excitation beam of the TUCS.

An important feature of the raster scans is their ability to characterize the presence of surface contamination, especially that created by exposure to drill fluid. Our observations from 2008 are consistent with high levels of contaminants on the exterior surface of all cores exposed to drill fluid and nearly all such cores also have substantial contamination on their interior cut faces when examined a few weeks after cutting. Using the raster scans, we find that drill fluid contamination typically penetrates 2 to 5 mm inward from the exterior drill surface of the core (see Figure 32 panels D and E). Hence it appears that the exposure of ice to drill fluid at high pressure during the mechanical drilling process allows for substantial penetration. It is possible that drill fluid propagates inward through microcracks that subsequently reseal themselves after trapping microscopic thicknesses of drill fluid. A consequence of the relatively deep penetration is that the drill fluid cannot easily be removed except by removing the corresponding ~5 mm of ice. The diffusion rate for the drill fluid is unknown, but molecules of lower molecular weight such as CH_4 and CO_2 are generally expected to have diffusion constants for solid ice of order 10^{-14} to 10^{-15} m^2/s (Neftel et al. 1983, Rohde and Price 2007). At that rate, 2 mm of diffusion ought to take of order 10 years making it impractical to wait for appreciable dissipation. By contrast, deposition of drill fluid on interior cut faces appears to extend only 1 mm or less in the

typical case (see Figure 32 panel F). This is consistent with our interpretation that contamination observed on the interior faces is secondary deposition of drill fluid that has migrated (either as a liquid or a vapor) from the exterior drill surfaces.

In most cases dry-drilled core pieces showed no or modest changes at their exterior surface, suggesting that dry drilling is not a significant source of contaminants. However, one notable exception was the exterior of the piece of WDC06A from a depth of 84 m (see Figure 32 panel C) which did show a bright contamination layer at the exterior interface. Given that drill fluid was not used at this depth, we can only assume that a contaminant was introduced in some other way. The most likely scenarios are either transfer during handling of the ice core or transfer from residues left on the equipment used to cut and process the core. The statistics are limited, but finding high contamination on one core segment among the six dry-drilled pieces examined suggests that such contamination may be somewhat common.

6 Analysis

6.1 Comparison of 2008 and 2009 intensities

In comparing the data collected in 2008 and 2009, we became aware of a significant discrepancy such that the 2008 data had substantially higher average fluorescence intensity than was observed in 2009. Performing a direct comparison of the 670 nm channel on 7 pieces of WDC06A that were scanned during both years, it was estimated that the intensity reported in 2009 was only 42% of that reported in 2008. The 670 nm channel was used due to its insensitivity to drill fluid contamination, which allowed a direct comparison without having to be concerned that drill fluid may have shifted during the intervening year.

It is believed at this time that this discrepancy is entirely an instrumental artifact created by differences in system alignment or performance during the two years. Since the discrepancy persists even though the laser's internal power reading has been incorporated into the data, the two most likely artifacts that could cause a substantial shift in apparent intensity are: 1) partial blockage of the laser beam in 2009 at some point between the laser power reading pickoff mirror and the incidence at the ice, or 2) a misalignment at the power sensor in 2008 leading to a systematic underestimate of the emitted power. Since an occluded beam path in 2009 would be associated with readily visible clipping and non-circularity in the beam, we believe it is unlikely that such an alignment problem would have occurred without being recognized and corrected.

Hence, we consider the second scenario more likely. We estimate that a misalignment of approximately 2 mm would be necessary to reduce the intensity on the active surface of the photodiode by 40%. Given the competing demands in aligning both the primary emission beam and the power sensor and the difficulty in directly verifying that the beam is centrally incident on the photodiode, it seems possible, though still surprising, that a 2 mm misalignment at the power sensor could have occurred without being caught. We did note during 2008 that the power sensor was reporting lower than typical beam intensities on average, but at the time we attributed this to reduced laser emission from a laser tube that suffered from persistent instabilities during most of the 2008 trip. In retrospect the poor performance from the laser tube may have also been masking a secondary problem associated with measuring the emitted laser power.

Based on this interpretation, and the comparison of 2008 and 2009 data described above, we have chosen to downscale all of the 2008 data by 0.4196 to make the two data sets consistent when plotted together.

6.2 Artifacts

6.2.1 Drill fluid contamination

An important experiment conducted in 2009 was to make direct comparisons of ice cores before and after 1 to 2 mm of material was removed by a mechanical planer. Initially this planing was accomplished by a stationary planing rig incorporated into the NICL workspace; however, this primary planar broke during the middle of our visit, so some planing was done with a less precise handheld motorized planar.

As illustrated in Figure 34, the signal generated in the 320 nm channel after planing is generally smoother and of lower intensity that the signal before planning. This strongly supports the conclusion that even interior cut faces can acquire significant levels of surface contamination. In fact, it appears likely that a majority of narrow spikes in the 2008 data are the result of surface contaminants that settled on the surface some time after cutting. From the wet drilled core (e.g. Figure 34, panels A and B) we also note a systematic downward offset between the planed and unplaned data, suggesting the removal of redeposited drill fluid across the entire core length. We note that in the dry-drilled GISP2 core (e.g. Figure 34, panels C and D) the fluorescence intensity after planing appears to more often match the same intensity of features of the unplaned core. We suggest that the absence of drill fluid is partially responsible for the similarity. However even for dry core we note that deviations are common suggesting that contamination by handling is also likely to be common.

A notable surprise is that in nearly all cases the planing resulted in an *increase* in the intensity at 670 nm. In most cases, this increase is smaller in magnitude than the decrease in the 320 nm channel. We can posit several possible explanations, though all are subject to factors that seem to make them seem unlikely. First of all, planing could have changed the optical texture of the ice surface in a way that created enhanced scattering, though visual inspection argues against this and if anything the surface texture appears smoother. Secondly, the planer could be depositing some residue that happened to have a 670 nm response. Given that two different planers were used during the ice work, this also seems unlikely. Lastly, the contamination removed from the ice core during planing might have been absorbing so much of the laser beam that it interfered with the excitation and transmission of the 670 nm channel from the underlying ice. Given the lack of any apparent disruption in the 2008 WAIS data during the dry core to wet core transition, this explanation also seems unlikely. So we have no clear answer for why planing would increase the intensity of 670 nm fluorescence.

6.2.2 Edge effects

We frequently observed that ice cores exhibited anomalously enhanced fluorescence at the top and bottom core limits. This was most notable in 2008 when a particular pattern of excess fluorescence was frequently visible at the limits of the core and extended along the core up to 10 cm (though usually less). Figure 36 illustrates this effect using selected pieces of the WDC06A core scanned in 2008. We note that the specific core section shown in Figure 36 was

dry-drilled, so even though drilling fluid is a common contaminant, it cannot the source of the edge effect seen here. Edge contamination was seen during every trip to NICL with both the BFS and the TUCS predecessor; however, the magnitude and characteristics of the effect varied from core to core. Indeed, a minority of cores did not show a change in average fluorescence intensity at their edges. When present the edge effect was nearly always manifested as a positive excursion across most or all of the channels (though 670 and 710 nm did seem exempt in some cases). We note that the edge effects observed in 2008 WDC06A cores were generally more consistent in magnitude and structure than observations made from other cores. This suggests that some factor in the handling or processing of the WDC06A core was systematically creating a large edge effect.

We posit that a combination of two factors is likely responsible for edge effects acting either alone or in combination. The first possibility is the presence of optical artifacts. Micro- or macro-fractures introduced into the ice due to cutting or breaking can affect the scattering of light in the core. As discussed in the following section, such fractures can lead to an increase in the effective volume of ice excited by the beam and enhance the resulting signal. However, if present at all, such fractures are likely to vary significantly from one core section to another and hence do not explain the consistently high edge effects in WDC06A. A second factor is that the angled phototubes will partially see through the edge of the ice core once the edge is reached. However, the fact that contamination can often be seen as far as 10cm from the edge suggests that the optical effects are unlikely to be the full story. We also note that the raster scans shown in Section 5.3 often lacked any abrupt changes at the edge of the core.

The second effect is contamination by handling. Core handling is generally done by NICL staff wearing thermal gloves with a polyethylene outer cover. The poly cover is of the same general type used in the food service industry and is intended to be clean but not sterile. It is fairly common for NICL staff to shift ice cores around by pushing or grabbing one end of the core, while it would be rare for a staff member to touch the middle of the core. It is difficult to know what possible cross-contamination sources might be present. However, we note that 10^3 – 10^5 colony forming units[q] / cm^2 are present on many common surfaces (Rusin et al. 1998), while up to 10^7 bacteria / cm^2 can be present on human skin (Fredricks 2001). Given that the expected concentration of bacteria in the samples is only 10^4 / cm^3 it is easy to see how even trivial amounts of cross-contamination could distort the signal. This increases the importance of planing the samples to remove surface contaminants, as discussed in Section 5.2. However, as seen in Figure 34 (especially panels B and D), an apparent edge enhancement can remain prominent even after planing. We speculate that this results from a combination of optical effects and contamination of the top and bottom surfaces, which were not planed when the surface along the core length was planed.

Our standard operating procedure for dealing with edge effects is to discard regions of core adjacent to any cuts or breaks when doing analysis or creating per segment averages (such

[q] A colony forming unit, often denoted simply as CFU, is an approximate measure of the number of cells in a population are viable and can be cultured using standard techniques such as agar plates. Functionally, the goal is to dilute and disperse a population of microbes and introduce them into a growth environment in such a manner than individual cells remain separated. Once they start to grow, the number of visible cell colonies is then used to infer a lower bound on the number of initial cells in the population. However, since many bacteria cannot be easily cultured, it must be noted that this is only a lower bound.

as appear in Figure 26 and Figure 30). With WDC06A every core segment was at least 65 cm, and we felt comfortable consistently discarding 10 cm at both ends of the core. With other cores we often needed to work with smaller fragments and so, when possible, attempted to discard 5 cm or less based on observational judgments about how far the edge effect extended.

6.2.3 Ice fractures

Fractures in the ice are a dramatic source of signal bias primarily due to optical effects such as refraction and internal reflection. Most macroscopic fractures in the ice core are visible to the naked eye due to scattering and reflections at the fracture surface. In many cases they can be easily seen unaided though in some cases they are detected only when illuminated by bright visible light. Assuming both segments of the fractured ice core remain adjacent to each other they will often fuse back together. In some cases, especially fractures occurring at high pressure during the core retrieval, the fusion will be so perfect that no visible fracture line remains. In most cases, however, a prominent visible fracture surface remains even after the broken segments fuse back together.

The same features that make fractures prominently visible in ordinary light also cause them to scatter both the incident excitation beam and the emitted fluorescent light. Scattering at the fracture plane is significantly stronger than scattering from bubbles and alters the effective volume illuminated by the laser. This increase in the effective excitation volume in turn leads to an increase in the fluorescence emission reaching the BFS (further discussion in Section 6.3). The net result is that fractures nearly always appear as very bright positive excursions. This is illustrated in Figure 37 with a fracture witnessed by the naked eye in a planed segment of the dry-drilled GISP2E core. The example used a dry core because it demonstrated that drill fluid could not have been trapped in the fracture, which would further contribute to the apparent signal. It is also possible that microbes might find the fracture surface an attractive place to grow; however, because of the optical biasing it is generally impossible to tell if this is ever the case.

Because of the effect of fractures on the received emission, it is essential to keep an accurate record of any fractures and defects observed in each ice core scanned. It also implies that one is unlikely to obtain usable results from the heavily fractured brittle ice region of WDC. The brittle ice, so named because its mechanical properties tend to cause spontaneous fractures when transferred from depth to atmospheric pressure, extends from approximately 600 to 1400 m at WAIS Divide. Though the WDC staff has created a system of netting to keep the core from falling apart, the high density of healed fractures makes this ice largely unusable for fluorimetry and it is likely to be omitted from future scanning.

6.3 Trend with Depth

In Figure 26 and Figure 30 we observe a steep fall off in both 320nm and 670nm emissions as a function of depth down to about 120m. This is the most prominent feature of our scans and appears to be a quasi-universal feature of ice cores with similar trends supported in the wide variety of cores scanned in 2009. At present there are two non-exclusive hypotheses for the nature of this change. This change evolves over the same depth scale during which the firn is being compressed into ice at WAIS Divide (Figure 38). Though there are some variations as a function of the temperature of the glacier and granularity of the originating snow, the

densification of firn into ice follows a qualitatively similar evolution versus depth at all glacial sites.

The trend could be a real feature indicating changes in the microbial population in the ice. Several factors could be posited to cause such a result. First, cells could simply die off over time due to exposure to the cold environment and an inability to adapt to the lower temperatures. This can occur because ice crystals may grow within and rupture the cell, because low temperatures interfere with cellular functions, or because the ice draws water out of the cell causing dehydration and death. Similarly some phototrophs could die as they become buried below the photic zone (the available sunlight is reduced by ~50% for every 10-15 m of depth, Bramall 2007). Secondly, the mechanical compression of the firn may rupture some cells, especially the large eukaryotes. Nathan Bramall has observed that snow algae tend to rupture quite easily under applied stress, such as that applied by a microscope cover slip (personal communication). Further the veins formed at the boundaries between ice grains tend to be only ~1 μm in size at the -50 °C temperature characteristic of WDC, which will exclude the larger eukaryotic cells (Price 2000, Rohde and Price 2007). Lastly, the veins themselves contain high concentrations of salts and other impurities that are excluded from the growing ice crystals. In most Antarctic sites the concentration of SO_4^{2-} and the absence of sufficient neutralizing agents (such as carbonate dust, which is more common in Greenland) leads to highly acidic veins (Price 2000, Wolff and Paren 1984, Langway et al. 1985). The combination of high acidity and other impurities may create an environment highly toxic to many bacteria, though it is known that some bacteria do survive in this microenvironment (Junge et al. 2004, Mader et al. 2006).

It is also worth noting that the tryptophan observed by the BFS need not be in a living cell in order to fluoresce. However, it does need to be at roughly neutral pH as acidity will quench the fluorescence (Lakowicz 1999). So, a cell that ruptures in an acidic vein would almost certainly to have its fluorescence quenched. Hence an alternative interpretation of the fall off in fluorescence is that many cells died and ruptured shortly after deposition into the ice, but it was not until the formation of vein networks that the local environment became acidic to a degree that the fluorescence of dead cells would be quenched.

An alternative explanation, not involving any real change in organic content, is that the fall-off with increasing ice density is entirely a result of changing ice optical properties. As evidenced in Figure 31, the firn and deeper ice look distinctly different due to the closure of pore spaces and the consolidation of ice grains. As already discussed in Section 6.2.3, optical changes associated with fractures can have a dramatic impact on the perceived fluorescence. It appears likely that a similar process affects the signal during densification. Figure 39 provides a schematic illustration of how this is likely to occur. For pure ice, the scattering and absorption length at 224 nm are of order meters at depths where bubbles are not a major factor in scattering (Ackermann et al. 2006). Furthermore, the absorption length for 10^5 1-micron cells / cm^3 is also at least meters due to low encounter frequency even if the cells are assumed to be fully absorbing. The primary ice property impacting beam propagation is bubble density, and hence effective scattering length. In the limiting case of an effective scattering length much shorter than the dimensions of the ice, the laser beam will tend to diffuse throughout the ice from the point of impingement, illustrated schematically by the left panel of Figure 39. This has the effect that an area much larger than the beam itself is brightly illuminated by the scattered laser light. Since the photon counters can also receive light from a volume much larger than the laser beam (Figure 11), this has the effect of significantly increasing the volume of fluorescence emission

that could be received by the BFS. By contrast, relatively clear ice (right panel of Figure 39) will scatter only a small amount of light while most of the beam passed through. As a result, relatively little of the visible area will be illuminated and the emission will be largely limited to bacteria that lie directly in the beam path.

The scale of the optical effect is hard to quantify without an independent measure of the concentration of bacteria in the ice. Qualitatively the effect can be observed by shining a visible laser onto the ice and comparing the size and intensity of the diffusive glow; however, this would be hard to quantify. It is entirely possible that both a real fall-off in cell concentrations and an artifact caused by changes in the optical properties of the ice are co-occurring. It is unlikely that these possibilities will be disentangled until direct cell counts can be made on the ice (see Chapter 7). One possibility to consider for future scans might be to convert one of the seven channels into a detector targeting scattered laser light. It is unlikely that the effective volume of the illuminated region would be linearly dependent on the intensity of 224 nm scattering, but the relationship could probably be computer-modeled without too much complexity, which would provide a way to back out that effect. Until ground-truth measurements of the cell concentrations and sizes can be made, one should assume that the fall-off in fluorescence intensity with depth may be entirely an optical artifact of changing ice properties.

6.4 Spectral Analysis

Relatively little interpretation has been performed of the spectral distribution of the fluorescence observed by the BFS. The 300-380 nm channels broadly capture tyrosine and tryptophan fluorescence. Assuming that tyrosine and tryptophan have an abundance ratio of roughly 2.2:1 as observed in mammals (Tourasse and Li 2000) and given the relative absorbance of 1:2.9 (Figure 2) then we can naively estimate their contributions to the total fluorescence to be roughly equal, with tyrosine emitting at a lower wavelength than tryptophan (Figure 40). However, it would be surprising if their fluorescence actually occurred in roughly equal proportions due to a phenomenon known as “resonant energy transfer”. This describes a process by which excited tyrosine molecules de-excite by laterally transferring their energy to nearby tryptophan molecules within the same protein (Lakowicz 1999). Hence it is widely expected that the observed fluorescence emission will be dominated by tryptophan, which is enhanced at the expense of any potential tyrosine signal. Bramall (2007) generally observed that fluorescence spectra from preparations of microbes in solution would peak around 320 nm, suggesting tryptophan dominated the emission spectrum albeit with a large environmental shift. Free tryptophan has an emission peak around 350 nm (Figure 3, Lakowicz 1999). This can be shifted anywhere from ~0 nm to ~40 nm through the action of environmental factors such as contact with water, bonds to other amino acids, and pH (Ladokhin 2000, Vivian and Callis 2001). Bramall’s (2007) observations suggest a shift of ~30 nm may be typical for microbes when considered in bulk within an aqueous environment.

Our fluorescence spectra are not consistent with Bramall. They do not turn over and trend towards zero intensity in the lowest wavelength channel. Instead, we find that most spectra appear to show the greatest emission in the 300 nm channel. In Figure 40, the mean fluorescence spectrum for the dry-drilled portion of the WDC06A core is presented. This mean curve shows a spectrum which peaks in the 300 nm channel and monotonically declines with increasing wavelength. This behavior is not specific to WAIS Divide and similar observations are made at other core sites.

It is possible to fit this data with a combination of tryptophan and tyrosine emissions. However, to do so we have to make several assumptions. First, we must assume that the shift in the tryptophan emissions peak is only about half that expected from Bramall (2007). If allowed to shift 30 or 35 nm, it is impossible to resolve the relative intensities of the long-wave components of the spectrum (i.e. 360 and 380 nm). A shift of 10-20 nm is more consistent with our observations. Given that the environmental factors affecting old microbes in ice may be very different from new cultures in solution, it is not unreasonable that the degree of shift might be different. Hence this difference might be considered plausible. More importantly however, in order to accommodate the 300 nm peak, we have to assume a very large contribution from tyrosine in the total emission spectrum. The best fit assumes 30% more tyrosine emission than would be expected even if no resonant energy transfer occurred. This would imply extremely high levels of tyrosine in our samples. We cannot immediately exclude that possibility, since bacterial endospores[r] created at times of stress can be heavily enriched in tyrosine (Ricca and Cutting 2003). However, Yung et al. (2007), found the fraction of endospores relative to all cells was small in the samples of GISP2 they examined.

More likely though the fit to tyrosine is spurious, and the true solution is that the ice contains some unidentified third component whose fluorescence properties are similar to tyrosine over the range of wavelengths we have observed. For example, dissolved organic matter – a generic name for poorly constrained mixtures of small free floating hydrocarbons (Grannas et al. 2006) – generally has an overall spectrum that peaks at 300 nm (or shorter) and decays towards longer wavelengths. We know such dissolved organic matter is present in ice cores (Grannas et al. 2006), but the relative importance to fluorimetry is not well-characterized.

Lastly, we should acknowledge the possibility that there is a systematic error in our calibrations and/or a fluorescent contaminant from the instrument itself. With respect to calibrations, we have had to rely on the factory measurements for instrumental responses because we do not have access to a fluorimeter with the appropriate sensitivity and range to independently calibrate the response of each component at 224 nm. We have verified that the signals observed at NICL are broadly similar to those we observed in laboratory microbe cultures (Figure 25, Rohde et al. 2007), but there are also unresolved differences. At the present time we don't know if this is because the glacial ice has different components than the lab cultures or because the lab cultures are tainted by other substances. In particular, it has proven very difficult to produce lab cultures that have not been exposed to plastics/rubber. Pure water tends to leach organics from plastic that are fluorescent at a low level and difficult to correct for. Finally, we should note that the construction materials of the BFS itself will also fluoresce. Essentially no practical material will not fluoresce at least a little at 224 nm, so the instrument is designed such that there are no natural paths by which scattered laser light can excite the BFS material and also have a direct line to a photon counter which can see that excitation. However, at the sensitivity of our instrument it is difficult to rule out the possibility that repeatedly scattered photons might sneak into the detectors.

In summary, the shape of our typical fluorescence spectrum is not well understood and does not easily match the expectations produced by Bramall (2007) and similar prior work.

[r] Endospores are durable, metabolically inactive forms created by some bacteria as a reaction to stress or food deprivation. They are intended to allow the cell to survive hostile conditions for long periods. If local conditions improve the cell would eventually convert back to its metabolically active form.

Though we can "fit" the results with high precision using amino acids alone, practical considerations suggest that approach is unlikely to provide a complete explanation. A more natural explanation is to assume there is an unidentified extra component affecting the fluorescence intensity near 300 nm.

6.5 Annual Cycle

We note that a weak oscillation in the 670 nm channel is visible during the top 100 m of WDC06A that is consistent with an annual cycle (Figure 41). It is unknown if this fluctuation represents a variation in the arrival of the fluorescent material or a modulating effect of optical variations in the ice associated with the annual cycle. Since annual banding is generally visible by eye, we suggest that the optical effect is a possible explanation for reasons similar to those discussed in Section 6.3. However we do not see a clear signal in the other channels which would favor a real modulation in bacterial deposition rather than an optical bias. This cycle does not appear to be recognizable in the fully dense ice. Hence, it is unlikely that this fluctuation will be useful for dating or determining the age of the ice.

6.6 Greenland versus Antarctica

It is instructive to compare Figure 1 to Figure 30. In Figure 1 there appears to be a qualitative difference between microbial samples in Greenland and those from Antarctica with the Greenland samples roughly an order of magnitude higher. This is not observed in Figure 30 where there is no clear separation between Greenland and Antarctica and in fact most of the samples lie within a single order of magnitude. This is an interesting observation suggesting that the microbial concentrations at the two sites are similar. Since the data presented in Figure 1 for Greenland largely came from different research groups than the data for Antarctica, it is possible that the apparent difference in Figure 1 is an artifact of differing approaches used by the various groups. This could imply contamination inflating the Greenland numbers, or more subtle differences in methodology. For example different approaches to determining the number of microbes in a sample, different criteria for distinguishing dust from microbes, or different processes for extracting intact microbes from ice could also influence the value that is ultimately measured.

Alternatively, the prior authors could be correct, in which case the similarity between Greenland and Antarctica represents a problem with our data. The worst case scenario would be if our data reflected only some non-microbial content that is similar in fluorescence intensity at both poles. The arguments in Rohde et al. 2008 and Rohde and Price 2007 generally oppose that interpretation since those works appear to show a correspondence between fluorescence variations and indicators of in situ cellular metabolism. Further, the calculation in Section 4 showing that the fluorescence intensity is reasonable for a microbial source also supports the conclusion that our data is primarily driven by microbial components. Hence we prefer the conclusion that our data is accurate and that the difference between poles reported in prior studies is potentially spurious. Ultimately, the way to resolve this issue is to perform both fluorimetry and cell counting on samples from both poles. Ideally, the cell counting would be performed in a single lab to minimize experimenter specific variations (see also Section 7).

6.7 Volcanic Index

A serendipitous discovery was made by noticing that volcanic ash layers were brightly fluorescent in both the 670 and 710 nm channels. Figure 42 shows an example of the fluorescence scans of a visible ash layer at Siple Dome and the Z2 layer at GISP2. The fluorescence is likely due to trace concentrations of transition metals in the ash particles. We note that Bramall (2007) found that many igneous minerals had some fluorescence and that this was more likely than with clays and other sedimentary minerals. In fact, the volcanic layers are virtually the only material in ice that ever triggered the 710 nm channel to any significant degree.

In order to better find and characterize volcanic ash falls we experimented with different ways of characterizing volcanic signals in the ice. Ultimately a volcanic index was created that consisted of the integrated anomaly-weighted deviations in the 670 and 710 nm channels The approach with WDC06A was somewhat different than with later cores. With WDC06A, the normal intensity and variance were defined by taking a Gaussian weighted moving average of each channel with an effective width of 15 m. Then each data series was re-expressed such that:

$$y_i^{'} = \frac{y_i - m_i}{s_i}$$

where y_i is the original intensity, m_i is the moving mean, s_i is the moving standard deviation. An index is then defined by:

$$\text{Volcanic Index} = \sum_{i=a}^{b} F\left(y_{i,670}^{'}\right) + F\left(y_{i,710}^{'}\right), \text{ where } F(y) = \begin{cases} 0, if\ y < 2 \\ y, otherwise \end{cases}$$

and the interval $[a, b]$ is a maximal interval such that:

For all $i \in [a, b]$
There exists a $j \in [i - 4, i + 4]$
Such that $y^{'}_{j} \geq 3$ for the 670 and 710 channels
and $y'_j < 2$ for all other channels

In this way we sum over consecutive points with anomalously high fluorescence in the 670 and 710 nm channels. The exclusion of high signals in the 300-380 nm channels is to prevent healed fractures from being mistaken as volcanic signals since such fractures correspond to abrupt increases in all channels (see Section 6.2.3). In practice, the main contributor to the index is from the 710 nm channel since it has low mean and variance under nearly all conditions.

While the mean and standard deviation used for the WDC data consisted of a multi-meter moving average, this was in general not possible with many of the other cores we studied because data was often not collected from adjacent meters. In these cases an ad hoc *y'* was created by separating data with exceptionally high 710 values and treating the remainder of the core as background for the purposes of defining a mean and standard deviation value. Taking this approach with the Siple Dome layer in Figure 42 produces a volcanic index of 3400 and two layers with indices of 1600 and 1400 for the Z2 ash layer in GISP2. So far the highest encountered index was 74000 on a different piece of Siple Dome ice.

The volcanic indices computed from the 2008 scans of WDC06A are shown in Figure 43. Though the scans of WDC06A contained greater than 410,000 spectra, only 162 non-zero volcanic index points were generated. As shown in the figure most of these points have index

values below 100 and are believed to comprise a background of windblown mineral grains that merely by chance had a composition similar to that of volcanic ash. However, such isolated grains would not correspond to a layer of particles the way that a volcanic ash fall would. The six higher outliers, depths 194.645, 250.446, 462.860, 499.692, 506.163, 549.360, and 566.521 m, were sent to Nelia Dunbar at New Mexico Tech who analyzed their content using microscopy and energy-dispersive x-ray spectroscopy. She found that five of the samples, identified as yellow circles in Figure 43, were composed simply of mineral dust; however, the abundance and size of the particles were anomalously large in all of these samples. Dunbar stated that the amount of dust observed in those layers was nearly unprecedented in her experience analyzing polar ice cores. By inference, based on the frequency of such outliers, we would suggest that these events correspond to exceptional dust storms of a kind to be expected every few hundred years. The final point, marked in green at 194.645 m and having an index value of 333.6, was found to have a few volcanic ash shards in it, though the concentration was exceptionally low. This demonstrated that the BFS is capable of detecting ash at concentrations far below what can be found through visible examination, though an index of 300 is probably about the limit of what can be distinguished from dust. Follow-up review led to the discovery that there was a more prominent (and optically visible) layer at 190.39 m which was not scanned in 2008 due to its position on a small core segment adjacent to a core break. Since Dunbar determined that these two layers have the same chemistry, we conclude that the 194 m ash was from a small pre-cursor eruption about 20 years before the main eruption.

Follow-up work in 2009 confirmed the BFS's ability to detect ash falls in Siple and GISP2 that were not visible to the naked eye. Several additional layers were located that had been found by borehole dust logging (Bay et al. 2005, Bramall et al. 2005) but not previously found in the cores. It appears plausible that the use of 710 nm fluorescence is the most sensitive non-destructive technique yet discovered for detecting volcanic ash layers in the returned core.

7 Future Work

Several of the goals of the BFS development remain unfulfilled. The most significant of these is calibrating the signal response to the actual concentration of microbes in the ice. Some work towards this end was done during 2008 and 2009. Two basic strategies are possible. First, one can make a target material with a known concentration of microbes and measure the instrument response. This is certainly achievable with water, but signal response in ice is heavily dependent on the optical qualities of the ice such as bubble density (see Section 6.3). Though it is easy to freeze microbes, it is very hard to reproduce the optical qualities of glacial ice ranging from firn, to recently consolidated ice, to deep ice with large grain sizes. As a result we have not yet come up with any method of constructing a calibrated ice samples that would be consistently representative of true glacial ice.

The second approach is to measure some samples of glacial ice with fluorimetry and then to directly measure the cell concentrations in the same samples using other cell counting techniques. This approach is certainly possible in principle and has been performed in the Berkeley lab previously (e.g. Tung et al. 2005). However, given that the environmental abundance of microbes is nearly always much higher than the $10^3 – 10^4$ cells / cm^3 that we expect from glacial ice (Figure 1, Section 6.2.2), this is still a very challenging measurement to

perform without introducing contamination. In previous work in our lab, such counts had been limited to deep ice. Deep ice is non-porous which allows its surfaces to be cleaned with antibacterial astringents such as HCl, NaOH, and NaOCl. This means that one can clean the ice with liquid reagents after cutting, and one does not need to focus as intensely on the cleanliness of the cutting implements and environment.

Unfortunately the most interesting large-scale signal seen in the BFS data is the decline in fluorescence from the near surface to the deep ice. This implies we need a method of studying the porous firn ice, even though it cannot be washed in astringents. So we have spent time trying to develop clean cutting methodologies. Most recently this has focused on using sterilized saws in a sterile glove box. Unfortunately, our tests with sterile ice reference samples continue to indicate that our techniques are not clean enough to work with the real ice samples. Given the complexity of the task, we may consider outsourcing the sample preparation and cell counting work for at least some of the ice to a lab with prior experience in this area.

Assuming sample preparation was to continue locally, there are several factors to consider. First, during existing attempts we have generally used bleach and purified water to clean and sterilize a portable glove box to serve as a working environment within the Latimer Hall cold room. However, we recently became aware of a very large autoclave at Koshland Hall that appears capable of accepting the entire glove box, and this should be considered in the future. In addition, the improvised holders and stands currently used should generally be replaced with custom implements better designed for holding and manipulating ice. The samples are small and irregular, so designing appropriate holders will be challenging. Often we have resorted to manipulating samples with the glove box gloves directly. Even if the gloves have been adequately sterilized, this creates a risk that body heat will lead to melting. Also, the act of directly holding small pieces of ice during sawing is potentially dangerous to the holder. Ideally aluminum should be used for most implements since it is among the easiest materials to clean. Nearly all organic residues will vaporize if heated to ~400 °C in an oxygen environment without damaging the material. Steel and iron implements are less effective in this regard since they will start to rust and recrystalize at ~200 °C. Though 200 °C is more than adequate for killing microbes it is much less effective at vaporizing organic residues. The saw blades used may also need to be replaced as longer blades without logos or decorations[s] would be desirable. Current tests suggest that saws with large teeth and relatively few teeth per inch (such as generally used for wood) are more effective at cutting ice than metal or stone saws. Because ice is hard and potentially breakable at -20 °C, it often has taken more than an hour of gentle sawing per sample to cut down a piece.

Regardless of how and where the samples are ultimately prepared, the analysis of samples for cell abundances and types is a key outstanding piece of work that is needed to help differentiate optical effects in ice from biological ones. Calibrating the instrument across a sampling of depths is also viewed as necessary for establishing the accuracy of our interpretations.

Related to calibrating the absolute microbial abundances and their variations with depth and core site, it would also be valuable to return to the ice core archives and further study

[s] The concern about logos is that they typically consist of a paint-like substance bonded to the blade, and these decorations will shed organic particles due to friction during the cutting process. Depending on the size of the particles they may be confused with cells.

variations and local spikes to understand their origin. As noted in the introduction, some microbial excesses may have the potential to materially affect the chemistry of the ice, for example through the metabolic generation of greenhouse gases such as methane and nitrous oxide. Similarly, the largest collection of ice that has been systematic scanned was the WDC ice at depths < 577 m, which was all Holocene in age, so we have not yet been able to determine if there are systematic variations across glacial / interglacial boundaries or to establish trends over the full lifetime of the ice. Similarly, microbes in the deepest and oldest ice should be studied because this is the region where a long history of metabolic activity has the greatest possibility of materially affecting the chemistry of the ice. In general, after building systematic records of the ice's organic content, these should be compared to other records of climate and chemistry to search for unexpected patterns.

The last outstanding goal for the BFS is to develop a self-contained system that will allow it to be incorporated into the NICL core processing line and/or taken into the field. The focus of that future work would be to develop a light-tight box which would allow ice to be scanned in local darkness even though bright lights were present in the core-processing laboratory. The operation of the BFS has until now occurred in rooms that could be sealed and darkened by turning off the lights, but that would not be practical in the core processing line or in the field. Because we are counting individual photons the seal would need to be of a very high quality while also quickly opened and closed. Further, we would have to develop processes for aligning and positioning ice within the box. These are tenable goals but will require a significant input of time and money for design and construction. So far, NICL has been receptive to including the BFS in the core processing line.

7.1 Recommendations for a Future BFS

In addition to the proposals discussed above to develop data to better understand the existing work and further apply the existing technology, it is constructive to consider what changes might be made to improve a future BFS-like instrument.

One of the most obvious conclusions from the discussion in Section 6.2 and Figure 37 is that ice optical quality matters a great deal. We suggest that a future instrument have a dedicated scattering channel targeted at 224 nm instead of one of the 360 or 380 nm channels. This would hopefully allow the operator to determine when signals are responding primarily to variations in ice optical quality (e.g. Figure 39) rather than changes in ice content. A scattering channel was actually tried in 2006 with the TUCS, but it had a very different view (side facing) than the primary channels. Dedicating a primary channel to scattering is probably necessary.

Whenever possible, one should arrange to only look at freshly cut or planed surfaces. Both the drill fluid transfer (Section 6.2.1) and the potential for contamination by handling cannot be ignored. Even in the case of dry-drilled core it appears that handling contamination is still likely to be a problem for a non-trivial fraction of all cores. For the study of recently collected cores, joining the core processing line at NICL appears scientifically ideal. That would allow one to systematically examine cores that had just been cut for the first time, ensuring both a clean surface and a large ice volume. The primary drawback with this approach is that the core processing line at NICL generally moves through only 15-20 m of core per day necessitating a much longer trip compared to the BFS's ability to process 100 m per day.

The programming problem with the Prometheus microcomputer (Section 2.3) should either be fixed or that system should be replaced. Right now this controller for the photon

counting modules represents a dangerous single point of failure with no spares and potentially weeks of downtime. In addition it is also the limiting factor in determining data rates due to its slow 9600 baud connection.

If possible a future system should also replace the laser. The laser provides an effective UV excitation but it is frustrating both in terms of alignment and stability. Learning to align the system is difficult and even with experience can take hours. At 1 μJ it is somewhat underpowered, but more importantly the pulsed design interacts sub-optimally with our preferred photo counting approach. A continuous wave laser, even at a power as low as of 50 μW would provide more total excitation power, avoid the saturation problems noted with the photon counters, and allow the photon counters to exploit their full dynamic range. Historically we have looked for alternative UV sources, but they tend to either have short operating lives, poorly positioned wavelengths, or are vastly more expensive than the TUCS. The growth of UV light emitting diodes should be watched closely though as it may provide a viable alternative.

Even if the laser is not replaceable one should look at improving the process of measuring laser intensity. The internal sensor has proven itself to be unreliable in at least timing, and difficult to maintain with appropriate alignment (Section 2.1.1). We recommend that a calibrated light meter suitable for UV should be acquired and used to verify the laser output at the target surface before and after every day's worth of scans. In addition, it may make sense to also replace the photodiode with something having a larger active surface and shorter separation between itself and an analog-to-digital converter. Under very fortunate conditions, a USB based light meter that was detachable might be able to perform both roles, but this might be challenging to set-up.

To better calibrate the instrument, one should locate and acquire time on a calibrated spectrofluorimeter known to operate reliably in the deep UV and measure the full spectral range we are interested in. Unfortunately, 224 nm is outside the range of most spectrofluorimeters as it is not easy to generate and many common construction materials and organic contaminants will fluorescence at this excitation making background controls more strenuous. In addition many fluorimeters do not extend into the red and infrared meaning that the 670 and 710 nm channels could not be tested. Building up a library of known standards would provide a point of comparison from which to verify the behavior of the BFS and eliminate concerns about systematic bias in the calibrations. Nathan Bramall had some success obtaining spectra using a salvaged spectrofluorimeter and an alternative UV light source. It is possible that his approach could provide some information again, but the laser he used is not currently functional and one would risk trading one calibration uncertainty for another since his interpretations rely on 10-year-old factory reports.

The photon counting modules and filter combination in general is well understood and the behavior is satisfactory. However, if one ever were to start over (and had unlimited funds) we suggest replacing this arrangement with a set of multi-anode photon counting modules coupled to diffraction gratings for wavelength selection. In principle, this approach could allow one to provide more than 100 simultaneous channels covering the entire emission space of interest with a similar data rate and only somewhat lower sensitivity per channel. Similar technology is in use in some modern spectrometers. Covering the emission space more broadly and in more detail would make it plausible that one could reconstruct more detailed information about the chemical composition of samples.

If work is to continue in cold rooms we also suggest that attention be paid to the quality of that working environment. Being in a cold enclosed space where one must frequently turn off the lights for fluorescence measurements is unpleasant and potentially dangerous. Historically a significant part of the work in the Latimer cold room was performed alone, but during part of 2009 a second student was available to assist with the work and that was a great improvement. We highly recommend finding ways to share this burden if work is continued in that environment.

8 References

1. Abyzov, S. and D. K. Perovich, *Climate Change and Polar Research*, Luso-American Development Foundation, Lisbon, Portugal, 63 pp. (2007).
2. Abyzov, S. S., I. N. Mitskevich, M. N. Poglazova, N. I. Barkov, V. Ya. Lipenkov, N. E. Bobin, B. B. Koudryashov and V. M. Pashkevich, "Antarctic Ice Sheet as a model in Search of Life on Other Planets," *Advances in Space Research* vol. 22, pp. 363–368 (1998).
3. Abyzov, S. S., R. B. Hoover, S. Imura, I. N. Mitskevich, T. Naganuma, M. N. Poglazova, and M. V. Ivanov, "Use of different methods for discovery of ice-entrapped microorganisms in ancient layers of the Antarctic glacier", *Advances in Space Research*, vol. 33:8, pp. 1222–1230 (2004).
4. Abyzov, S., I. N. Mitskevich, M. N. Poglazova, N. I. Barkoti, V. Ya. Lipenkos, N. E. Bobin, B. B. Kudryashoti, and V. M. Pashkevich, "Antarctic Ice Sheet as Object for Solving Some Methodological Problems of Exobiology," *Advances in Space Research***,** vol. 23:2, pp. 371–376 (1999).
5. Abyzov, S., M. Fukuchi, S. Imura, H. Kanda, I. Mitskevich, T. Nagamuna, M. Poglazova, L. Savatyugin, and M. Ivanov, "Biological investigations of the Antarctic ice sheet: review, problems and projects," *Polar Bioscience*, No. 17, pp. 106–116 (2004).
6. Ackermann, M., and many others (IceCube Collaboration), "Optical properties of deep glacial ice at the South Pole," *Journal of Geophysical Research*, v. 111, pp. D13203 (2006).
7. Bay, R. C., N. Bramall, P. B. Price, G. Clow, R. Hawley, R. Udisti, and E. Castellano, "Globally synchronous ice core volcanic tracers and abrupt cooling during the Last Glacial Period," *Journal of Geophysical Research* 111, pp. D11108 (2005).
8. Bay, Ryan, Nathan Bramall, and P. Buford Price, "Searching for microbes and biogenic compounds in polar ice using fluorescence", *Life In Ancient Ice*, S. Rogers, J. Castello, eds. (Princeton Press, 2003).
9. Beechem J. M. and L. Brand, "Time-Resolved Fluorescence of Proteins," *Annual Review of Biochemistry*, vol. 54, pp. 43–71 (1985).
10. Bhartia, Rohit, William F. Hug, Everett C. Salas, Ray D. Reid, Kripa K. Sijapati, Alexandre Tsapin, William Abbey, Kenneth H. Nealson, Arthur L. Lane, and Pamela G. Conrad, "Classification of Organic and Biological Materials with Deep Ultraviolet Excitation," *Applied Spectroscopy*, vol. 62:10, pp. 1070–1077 (1985).
11. Bidle, Kay D., SangHoon Lee, David R. Marchant, and Paul G. Falkowski, "Fossil genes and microbes in the oldest ice on Earth," *Proceedings of the National Academy of Science*, vol. 104:33, pp. 13455–13460 (2007).
12. Bramall, N. E., R. C. Bay, K. Woschnagg, R. A. Rohde, P. B. Price, "A deep high-resolution optical log of dust, ash, and stratigraphy in South Pole glacial ice", *Geophysical Research Letters* 32:21, Article Number: L21815 (2005).
13. Bramall, N. E., *The Remote Sensing of Microorganisms*. PhD thesis, University of California at Berkeley (2007).
14. Brozen, Reed and Christian Fromm, "Ultraviolet Keratitis" [online], December 9, 2009, available: http://emedicine.medscape.com/article/799025-overview [accessed: January 5, 2010].

15. Christner, B., E. Mosley-Thompson, L. G. Thompson, V. Zagorodnov, K. Sandman, and J. N. Reeve, "Recovery and Identification of Viable Bacteria Immured in Glacial Ice", *Icarus* 144, pp. 479–485 (2000).
16. Christner, Brent C., George Royston-Bishop, Christine M. Foreman, Brianna R. Arnold, Martyn Tranter, Kathleen A. Welch, W. Berry Lyons, Alexandre I. Tsapin, Michael Studinger, John C. Priscu, "Limnological conditions in Subglacial Lake Vostok, Antarctica," *Limnology and Oceanography* vol. 51:6, pp 2485–2501 (2006).
17. Fredricks, David N. "Skin Microbial Ecology," *Journal of Investigative Dermatology Symposium Proceedings* 6, 167–169 (2001).
18. Gailitis, Ray P., Qiushi Ren, Keith P. Thompson, J. T. Lin, and George O. Waring III, "Solid state ultraviolet laser (213 nm) ablation of the cornea and synthetic collagen lenticules," *Lasers in Surgery and Medicine* vol. 11:6, pp. 556–562 (1991).
19. Gartry, David S. (editor), *Excimer Lasers in Ophthalmology: Principles and Practice*, 1997, Informa Healthcare: London, UK, 472 pages.
20. Grannas, A. M., W. C. Hockaday, P. G. Hatcher, L. G. Thompson, and E. Mosley-Thompson, "New revelations on the nature of organic matter in ice cores", *Journal of Geophysical Research*, 111, pp. D04304 (2006).
21. Junge, K., H. Eicken, and J. W. Deming, "Bacterial Activity at -2 to -20°C in Arctic Wintertime Sea Ice," *Applied Environmental Microbiology* 70, pp. 550–557 (2004).
22. Ladokhin, A. S., "Fluorescence Spectroscopy in Peptide and Protein Analysis," *Encyclopedia of Analytical Chemistry*, John Wiley & Sons Ltd, pp. 5762–5779 (2000).
23. Lakowicz, Joseph R., *Principles of Fluorescence Spectroscopy, Second Edition*, Kluwer Academic / Plenum Publishers: New York (1999).
24. Langway, C. C., H. Oeschger, and W. Dansgaard, *Greenland Ice Core: Geophysics, Geochemistry, and the Environment*, American Geophysical Union (1985).
25. Mader, Heidy M., Michala E. Pettitt, Jemma L. Wadham, Eric W. Wolff and R. John Parkes, "Subsurface ice as a microbial habitat," *Geology* 34*:*169–172 (2006).
26. Miteva, V. I., P. P. Sheridan, and J. E. Brenchley, "Phylogenetic and Physiological Diversity of Microorganisms Isolated from a Deep Greenland Glacier Ice Core," *Applied and Environmental Microbiology* vol. 70:1, pp. 202–213 (2004).
27. Miteva, Vanya, Catherine Teacher, Todd Sowers, and Jean Brenchley, "Comparison of the microbial diversity at different depths of the GISP2 Greenland ice core in relationship to deposition climates," *Environmental Microbiolog* vol. 11:3, Pages 640–656 (2009)
28. Morse, D. L., D. D. Blankenship, E. D. Waddington, and T. A. Neumann, "A site for deep ice coring in West Antarctica: Results from aerogeophysical surveys and thermal-kinematic modeling", *Annals of Glaciology*, 35, pp. 36–44 (2002).
29. Moseley, H. "Ultraviolet and laser radiation safety," *Physics in Medicine and Biology* 39, pp. 1765–1799 (1994).
30. Neftel A, H. Oeschger, J. Schwander, and B. Stauffer, "Measurement of direct current conductivity on ice samples for climatological applications", *Journal of Physical Chemistry* 87, pp. 4116–4120 (1983).
31. Parker Automation, "Gemini GV6K and Gemini GT6K Programmer's Guide", [Online]. (2001) Available: http://www.parkermotion.com/manuals/gemini/Gem6K_PG_RevA.pdf, version 88-019934-01 A [Accessed: December 20, 2009]. Parker Motion, Cleveland, OH.

32. Photon Systems, “Deep UV Lasers”, [Online]. (2007) Available: http://www.photonsystems.com/pdfs/duv-lasersource-rev2.pdf, version 050207-rev2 [Accessed: December 20, 2009]. Photon Systems, Covina, CA.
33. Photon Systems, “TUCS Data Sheet”, [Online]. Available: http://www.photonsystems.com/pdfs/TUCSDataSheet.pdf [Accessed: December 20, 2009]. Photon Systems, Covina, CA.
34. Price, P. B., “A habitat for psychrophiles in deep Antarctic ice,” *Proceedings of the National Academy of Science*, 97, pp. 1247–1251 (2000).
35. Ralchenko, Yu., A. E. Kramida, J. Reader, and NIST ASD Team (2008). *NIST Atomic Spectra Database* (version 3.1.5), [Online]. Available: http://physics.nist.gov/asd3 [2009, November 25]. National Institute of Standards and Technology, Gaithersburg, MD.
36. Ricca, Ezio and Simon M. Cutting, “Emerging Applications of Bacterial Spores in Nanobiotechnology,” *Journal of Nanobiotechnology* 1:6 (2003)
37. Rohde, R.A., P. B. Price, R. C. Bay and N. E. Bramall, “In situ microbial metabolism as a cause of gas anomalies in ice,” *Proceedings of the National Academy of Sciences* vol. 105:25, pp. 8667–8672 (2008).
38. Rohde, Robert A. and P. Buford Price, “Diffusion-controlled metabolism for long-term survival of single isolated microorganisms trapped within ice crystals,” *Proceedings of the National Academy of Science*, vol. 104:42, pp. 16592–16597 (2007).
39. Rusin, P., P. Orosz-Coughlin and C. Gerba, “Reduction of faecal coliform, coliform and heterotrophic plate count bacteria in the household kitchen and bathroom by disinfection with hypochlorite cleaners,” *Journal of Applied Microbiology* 85, 819–828 (1998).
40. Schilta, Adrian, Matthias Baumgartnera, Thomas Blunierc, Jakob Schwandera, Renato Spahnia, Hubertus Fischera, and Thomas F. Stockera, “Glacial–interglacial and millennial-scale variations in the atmospheric nitrous oxide concentration during the last 800,000 years,” *Quaternary Science Reviews*, in press.
41. Sheridan, Peter P., Vanya I. Miteva, and Jean E. Brenchley, “Phylogenetic Analysis of Anaerobic Psychrophilic Enrichment Cultures Obtained from a Greenland Glacier Ice Core,” *Applied Environmental Microbiology* 69:4, pp. 2153–2160 (2003)
42. Souchez, R., “The buildup of the ice sheet in Central Greenland,” *Journal of Geophysical Research* 102:C12, pp. 26317–26323 (1997).
43. Souchez, R., M. Lemmens, and J. Chappellaz, “Flow-induced mixing in the GRIP basal ice deduced from the CO_2 and CH_4 records,” *Geophysical Research Letters* 22, pp. 41–44 (1995).
44. Stauffer, B., T. Blunier, A. Dallenbach, A. Indermuhle, J. Schwander, T. F. Stocker, J. Tschumi, J. Chappellaz, D. Raynaud, C. U. Hammer, and H. B. Clausen, “Atmospheric CO_2 concentration and millennial-scale climate change during the last glacial period,” *Nature*, 392, pp. 59–62 (1998).
45. Stauffer, Bernard, Jacqueline Fluckiger, Eric Monnin, Jakob Schwander, Jean-Marc Barnola, and Jérôme Chappellaz, “Atmospheric CO2, CH4 and N2O records over the past 60 000 years based on the comparison of different polar ice cores,” *Annals of Glaciology*, vol. 35:1, pp. 202–208 (2002).
46. Tourasse, Nicolas J. and Wen-Hsiung Li, “Selective Constraints, Amino Acid Composition, and the Rate of Protein Evolution,” *Molecular Biology and Evolution* 17, pp. 656–664 (2000).

47. Tung, H. C., N. E. Bramall, and P. B. Price, “Microbial origin of excess methane in glacial ice and implications for life on Mars,” *Proceedings of the National Academy of Science*, vol. 102:51, pp. 18292–18296 (2005).
48. Tung, H. C., P. B. Price, N. E. Bramall, and G. Vrdoljak, “Microorganisms metabolizing on clay grains in 3-km-deep Greenland basal ice,” *Astrobiology* vol. 6:1, pp. 69–86 (2006).
49. Verdeyen, J. T., *Laser Electronics*, Third ed., Prentice Hall series in solid state physical electronics (Prentice Hall, Upper Saddle River) pp. 326–332 (2000).
50. Vivian, J. T. and P. R. Callis. “Mechanisms of tryptophan fluorescence shifts in proteins,” *Biophysical Journal*, 80:2093–2109 (2001).
51. Willerslev, Eske, Anders J. Hansen, Brent Christensen, Jørgen Peder Steffensen, and Peter Arctander, “Diversity of Holocene life forms in fossil glacier ice,” *Proceedings of the National Academy of Science*, vol. 96:14, pp. 8017–8021 (1999).
52. Wolff, E. W. and J. G. Paren, “A two-phase model of electrical conduction in polar ice sheets,” *Journal of Geophysical Research*, vol. 89:B11, pp. 9433–9438 (1984).
53. Yung, Pun To, Hannah S. Shafaat, Stephanie A. Connon, and Adrian Ponce, “Quantification of viable endospores from a Greenland ice core,” *FEMS Microbiology Ecology* 59, pp. 300–306 (2007)
54. Zhang Xiaojun, Ma Xiaojun, Yao Tandong, and Zhang Gaosen, “Diversity of 16S rDNA and environmental factor influencing microorganisms in Malan ice core,” *Chinese Science Bulletin* vol. 48:11, pp. 1146–1151 (2003).
55. Zhang, X. F., T. D. Yao, L. D. Tian, S. J. Xu, and L. Z. An, “Phylogenetic and Physiological Diversity of Bacteria Isolated from Puruogangri Ice Core,” *Microbial Ecology* 55, pp. 476–488 (2008).

9 Figures

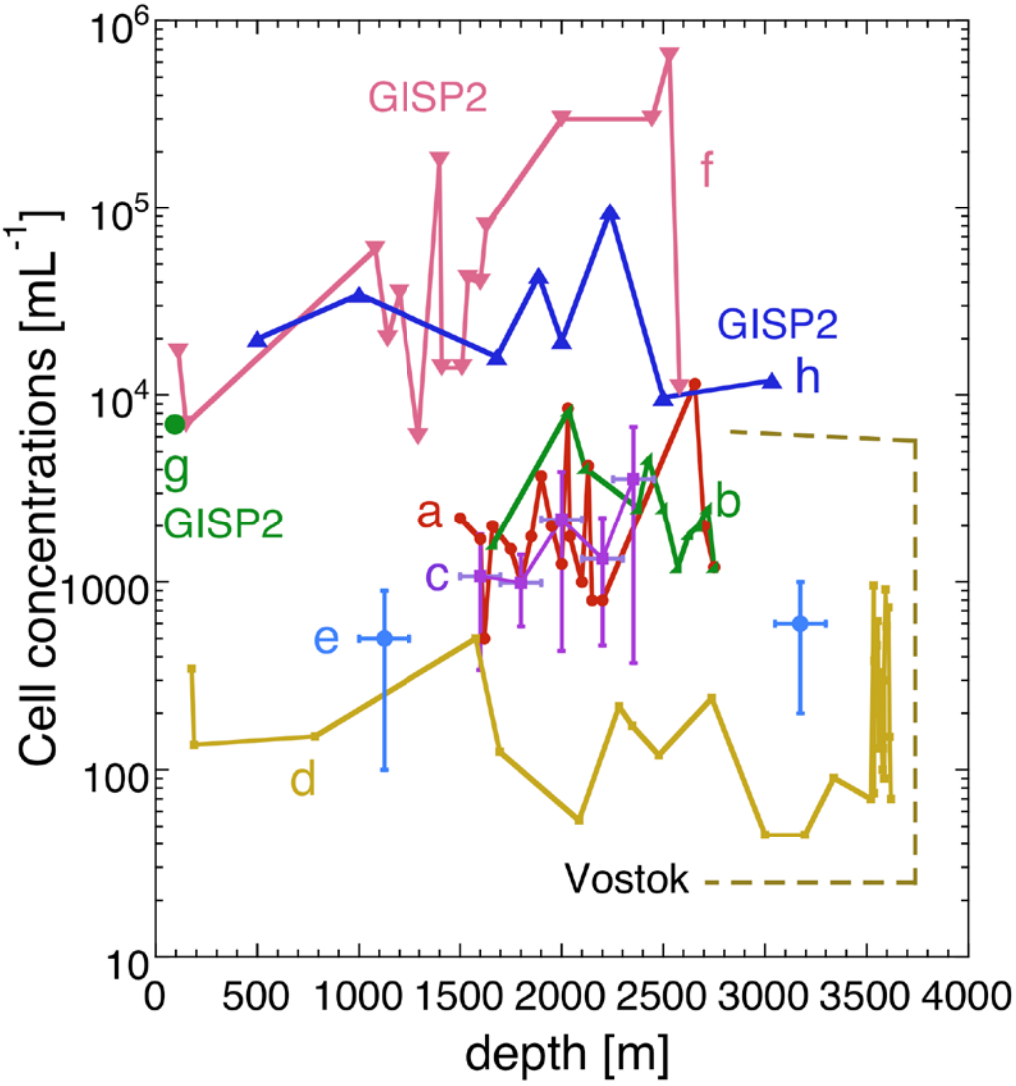

Figure 1: Measured microbial concentration versus depth for a variety of ice cores and depths. Labels refer to a) Abyzov et al. 1998, b) Abyzov and Petrovic 2007, c) Abyzov et al. 2004a, d) Christner et al. 2006, e) Abyzov et al. 2004b, f) Miteva et al., 2009, g) Yung et al. 2007, h) Tung et al. 2005. Samples a through e are from Antarctica while f through h refer to GISP2 in Greenland. Figure prepared by P. Buford Price for Astrobiology Science Conference 2010.

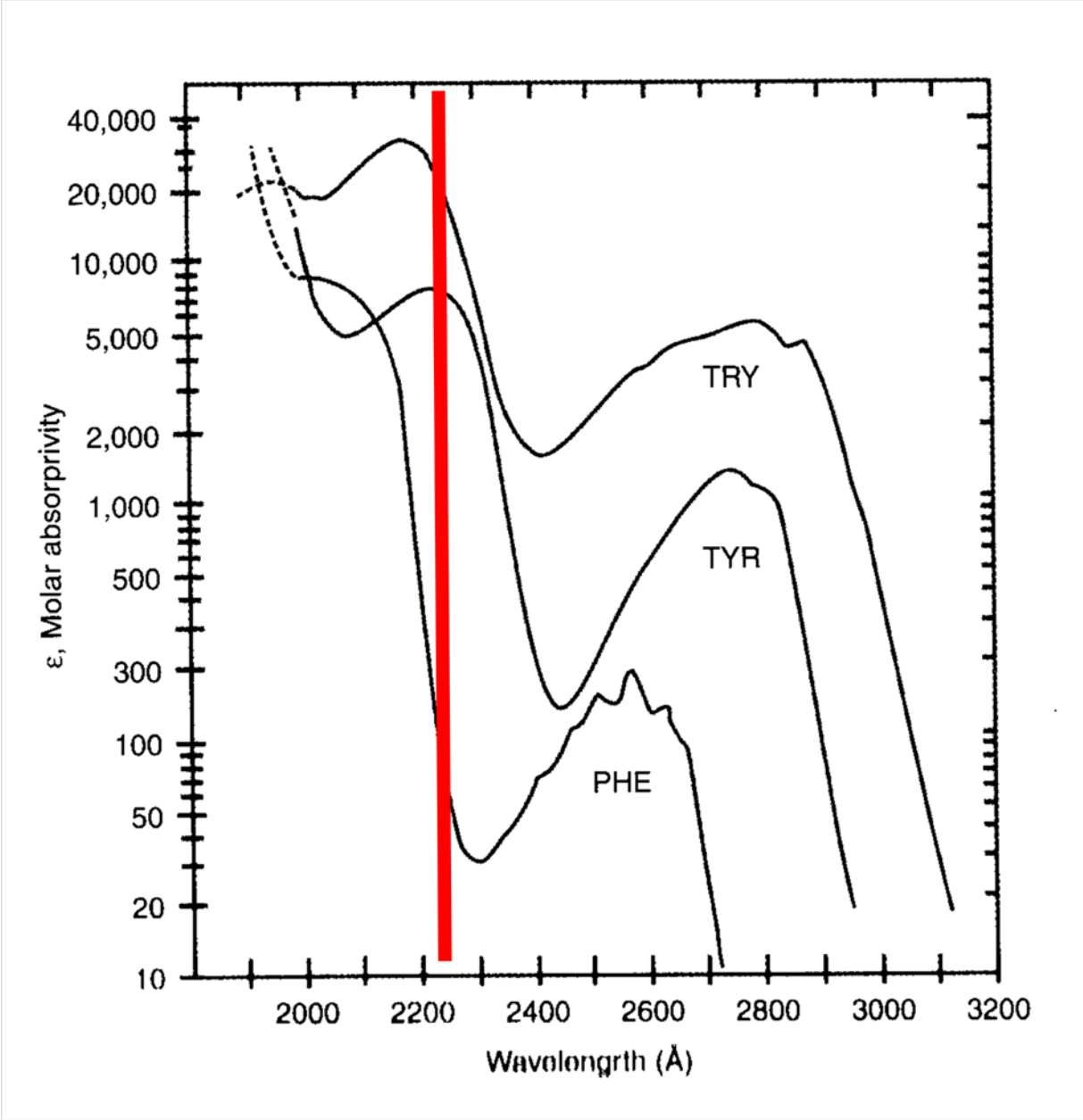

Figure 2: Absorbance spectra for tryptophan (TRY), tyrosine (TYR), and phenylalanine (PHE) as a function of wavelength as reported by Lakowicz 1999. The vertical red line indicates the wavelength used to operate the BFS.

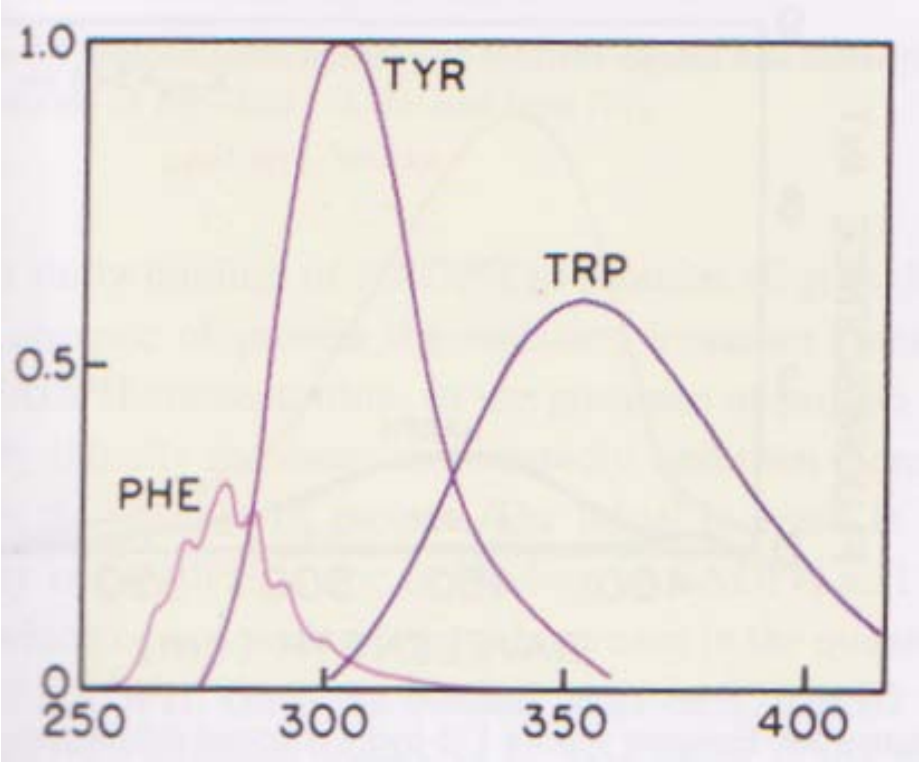

Figure 3: Relative emission spectra versus wavelength per absorbed photon for the free amino acids tryptophan (TRP), tyrosine (TYR), and phenylalanine (PHE), as reported by Lakowicz 1999. The scale is arbitrarily set to 1 at the tyrosine peak. It should be noted that the emissions spectra peak of protein-bound tryptophan – as opposed to free tryptophan – will be shifted shortward by up to ~40 nm in actual cells compared to its position on this plot (Bramall 2007, Lakowicz 1999).

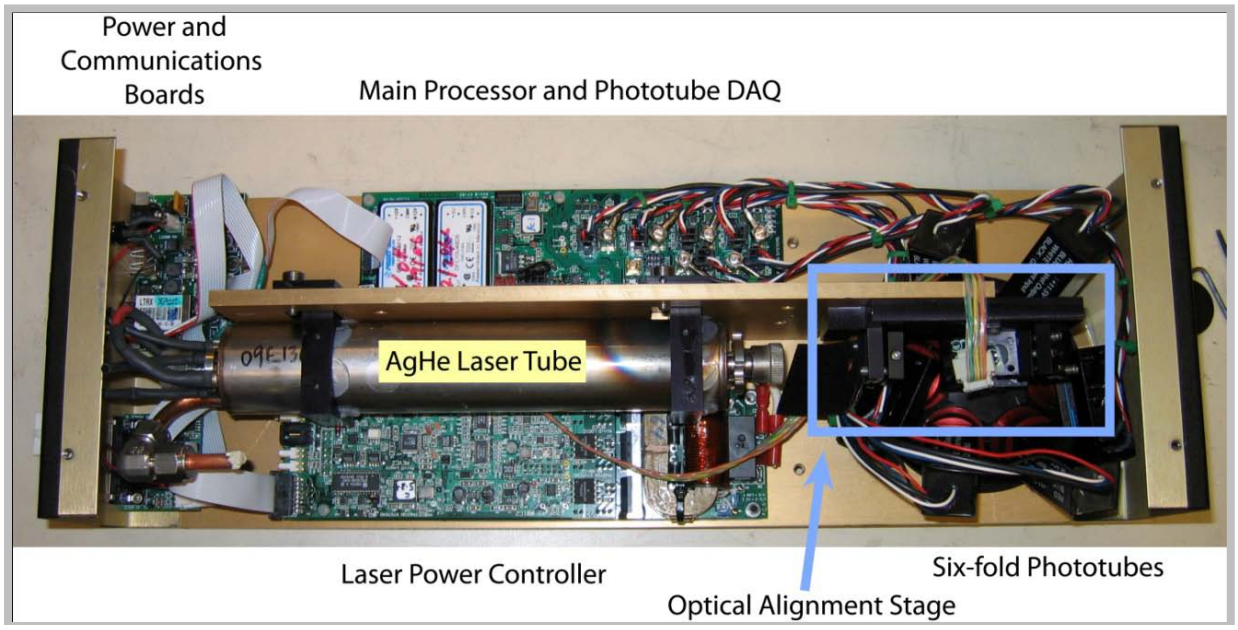

Figure 4: Photograph of the TUCS internals showing the AgHe laser tube, the optical column, the main processor board and prior data acquisition system, the power control board, the communications boards, and phototubes. See Section 2.1.

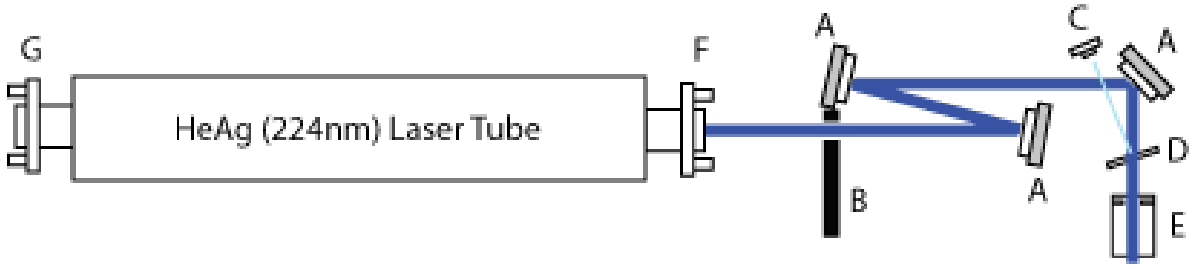

Figure 5: Side-view illustration of the TUCS optical path. A) Alignment and filtering mirrors, B) felt screen, C) internal power sensor, D) 1% partial mirror, E) exit port, F) secondary laser alignment coupler, G) primary laser alignment coupler. See Section 2.1.

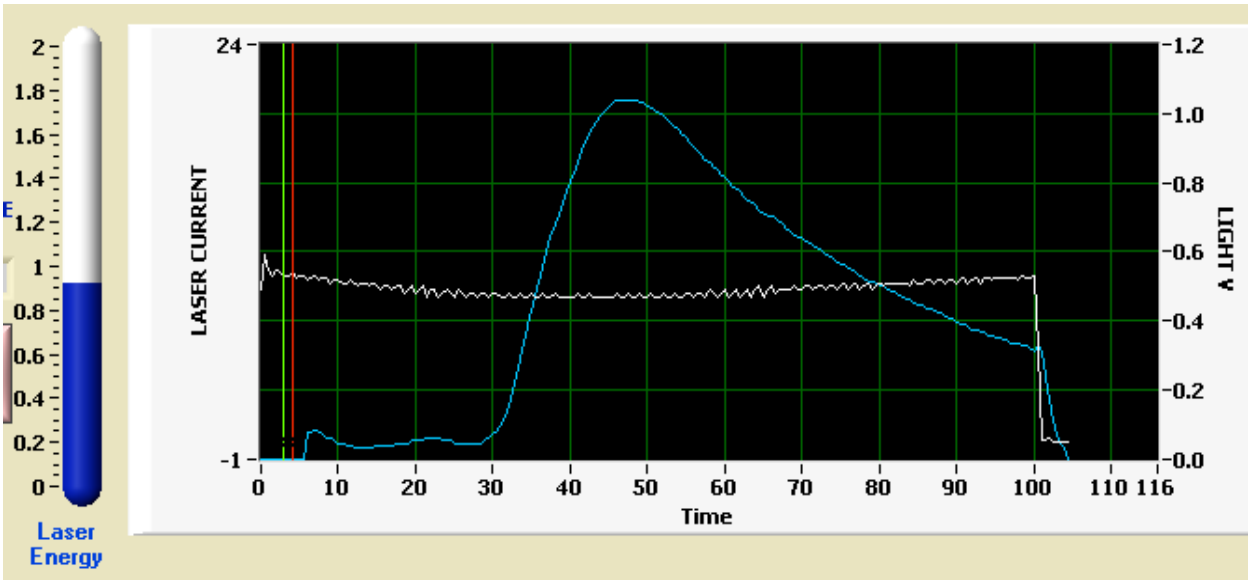

Figure 6: Time series plot of the internal power sensor as displayed to the operator. The white, flat curve shows the current in amps delivered to the laser, while the blue curve is the laser power reading from the internal sensor (uncalibrated units). Time is in μs. The total integrated energy is shown in the leftmost indicator in μJ. This panel is taken from a different version of the software than is currently used with the BFS and hence has slightly different coloring and labeling. It should also be noted that the TUCS laser often reports a true zero until the rise begins at ~30 μs, rather than the small but non-zero curve indicated here. The power sensor has been found to be unreliable with respect to the accuracy of the time series, as discussed in Section 2.1.1.

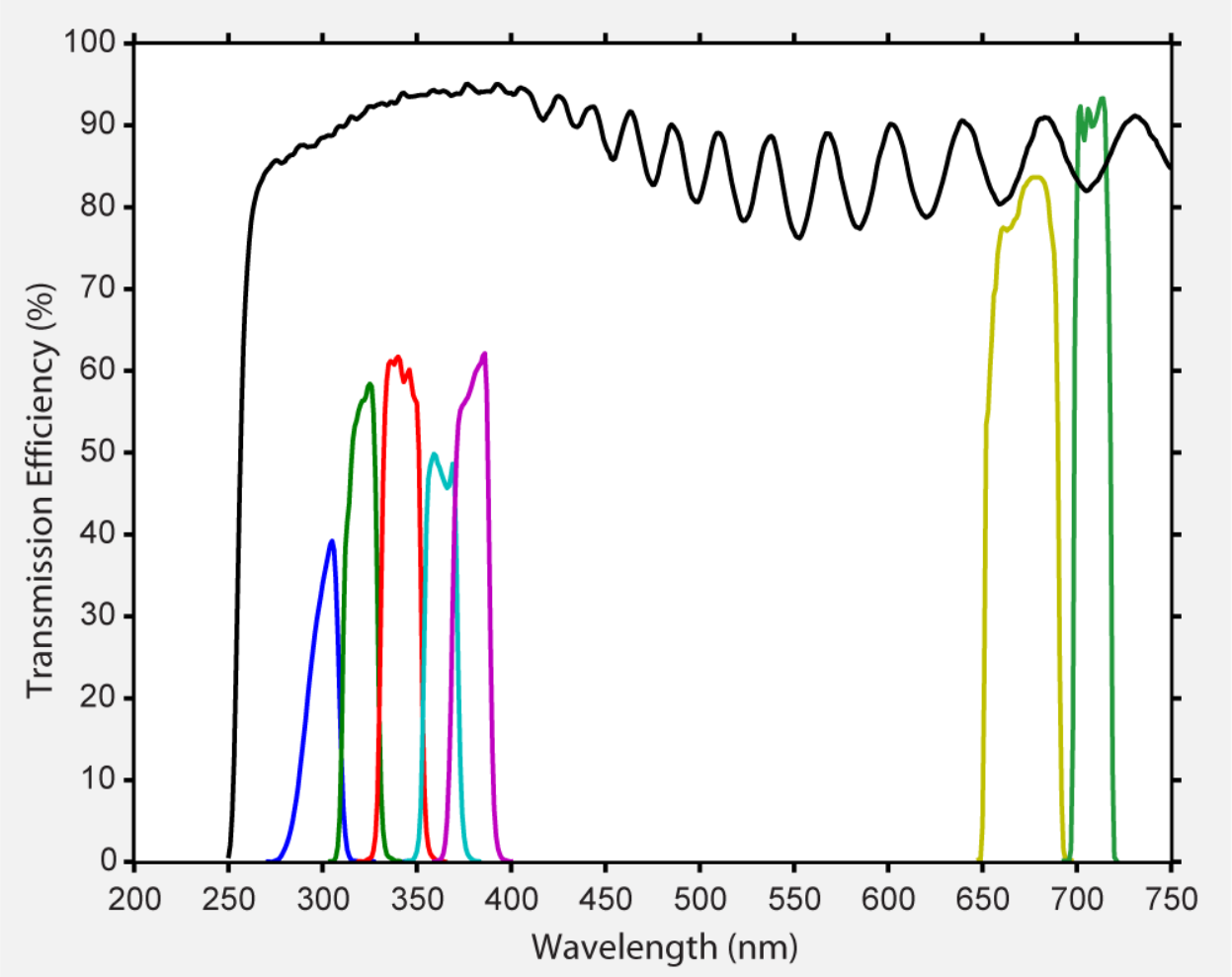

Figure 7: Transmission spectrum of the seven band-pass filters and laser blocking filter used in the BFS. The band-pass filters have centers 300, 320, 340, 360, 380, 670 and 710 nm. The width of each filter is 20 nm except for the 670 nm filter, which has a width of 40 nm. A laser-blocking filter is based at the start of each optical column and is used to prevent scattered 224 nm laser light from entered in the viewing system.

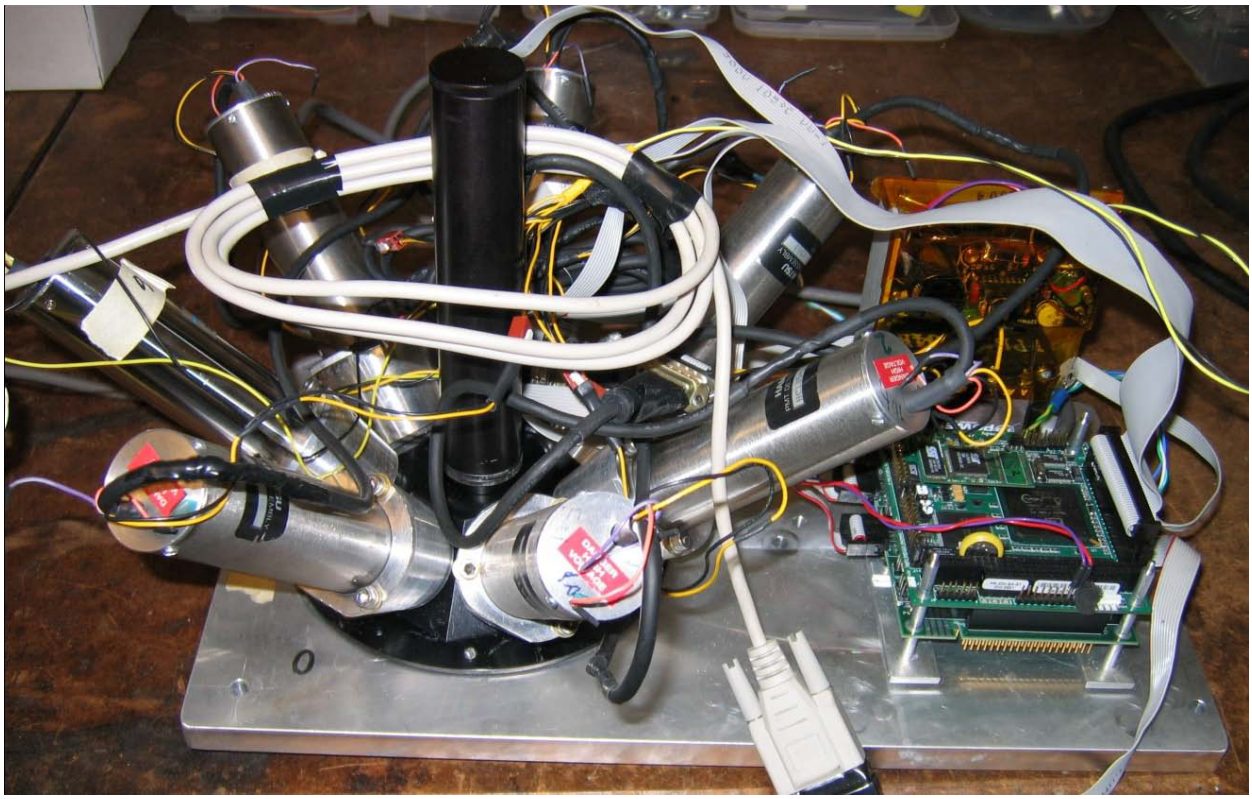

Figure 8: Photograph of photon counter system. The seven-fold photon counters are visible on the left, the microcomputer on the forward right and the power controller on the back right. The TUCS laser system (or any other laser system) would mount above the vertical black column and inject laser light into the center of the photon counting ring. The central point of visibility lies slightly below the bottom surface of the base plate and is subsequently shown in Figure 16.

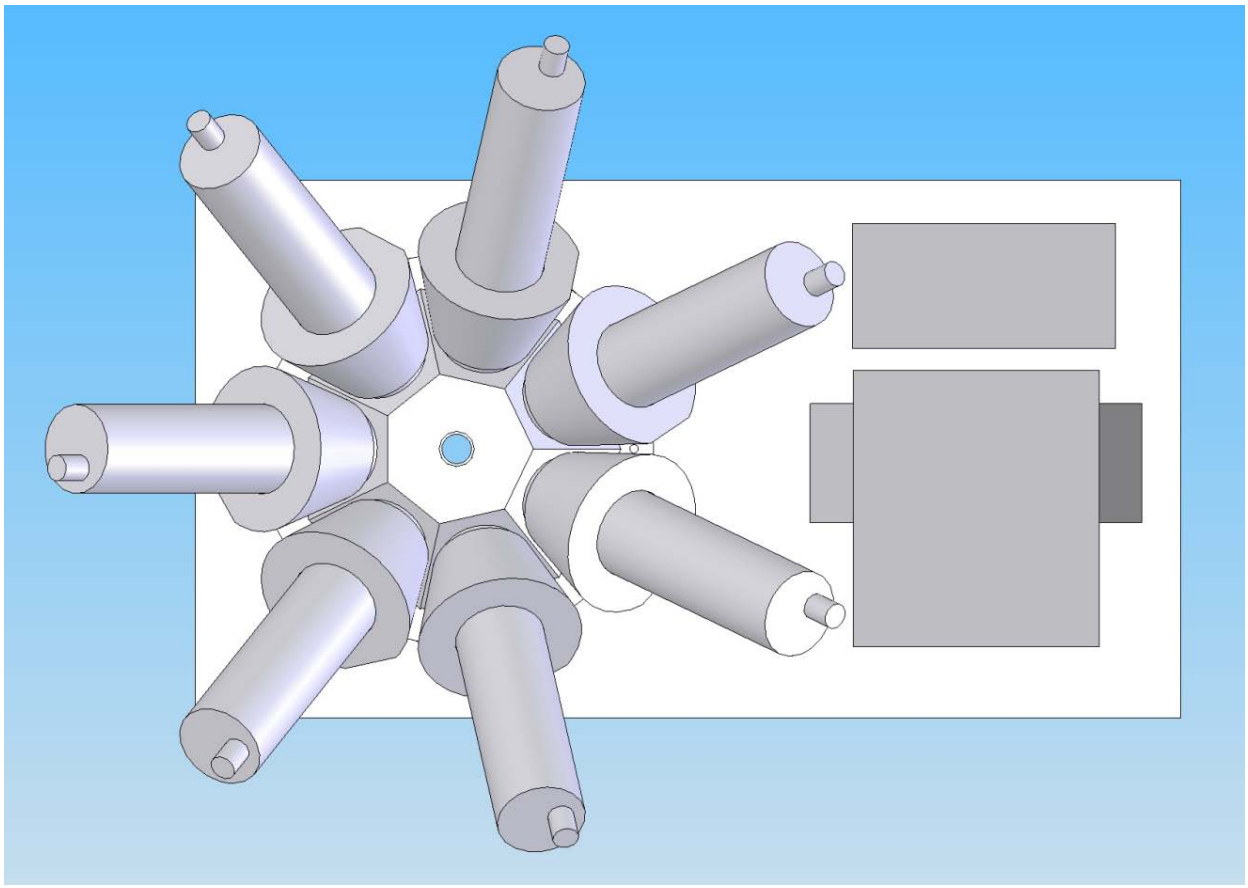

Figure 9: Top down view of the photon counting rig. On the left side are the seven photon counters attached to o-ring sealed collars and positioned at 45 degree angle to the vertical. The central hole provides entry for the laser beam and the whole system focuses on a point just below the system on the obverse side. At the upper right is the power converter and at the lower right is the microcomputer which communicates with the seven photon counters and then relays results back to the controlling laptop computer.

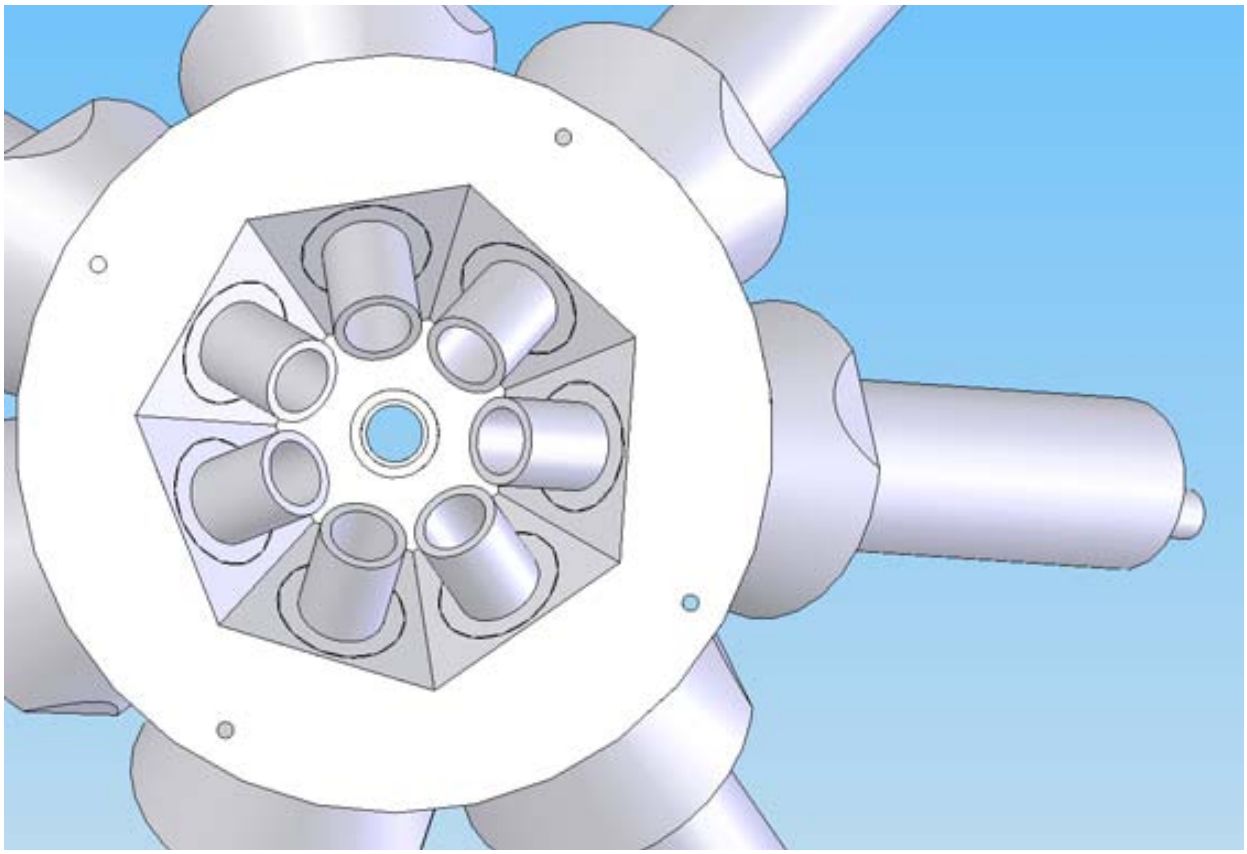

Figure 10: Underside of the mounting assembly showing the 1/2" tubes that extend towards the sample and ultimately define the geometry and visibility of the instrument.

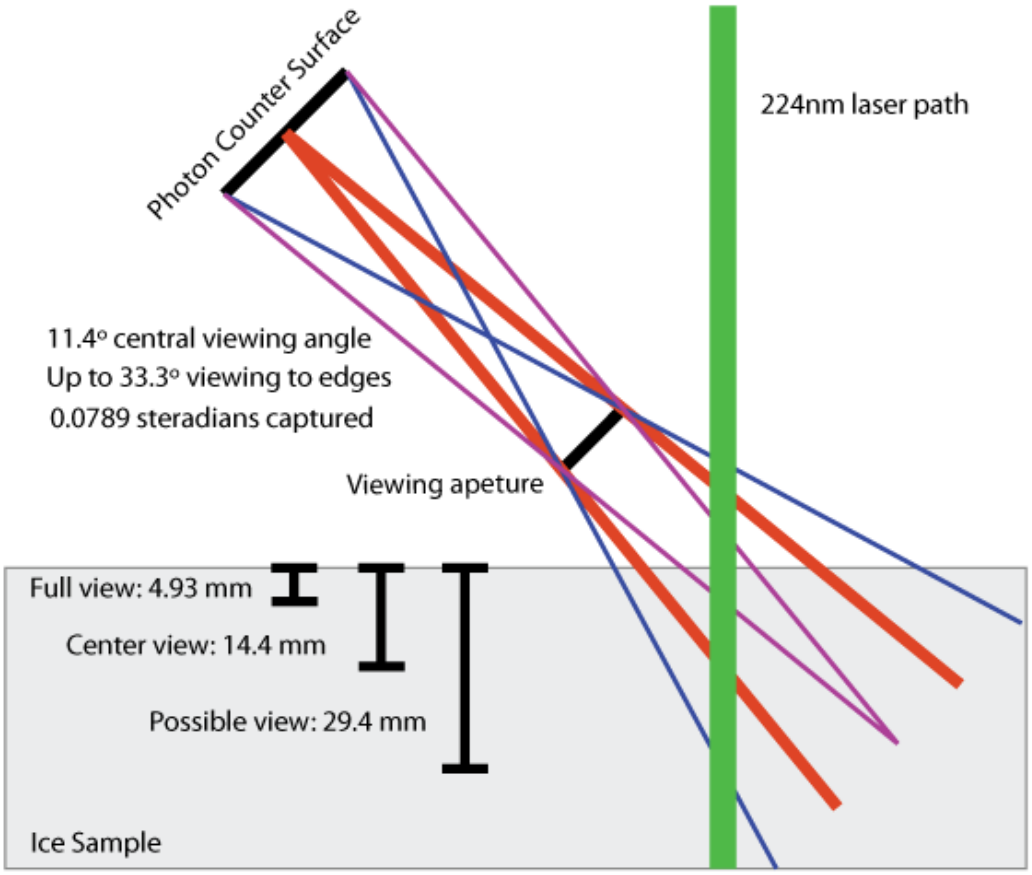

Figure 11: Scale diagram of the viewing geometry of the photon counter system. In its unfocused condition a laser beam approximately 4 mm in diameter should encounter the ice just below the exit port on the lower surface of the photon counting rig. This point is coincident with the central line of the seven photon counters. The view is primarily controlled by a ½″ viewing aperture positioned near the surface of the ice. This window allows fluorescent emissions up to ~5 mm in depth to be visible to the entire active surface of the photon counter. Deeper emissions will be visible to progressively smaller fractions of the active surface of the photon counters, until at ~30 mm no direct path exists between the ice and the photon counter. Initially these views were limited further by a horizontal apeture just above the surface of the ice, but it was found that stray light hitting this metal surface was producing a systematic background and that aperture was removed.

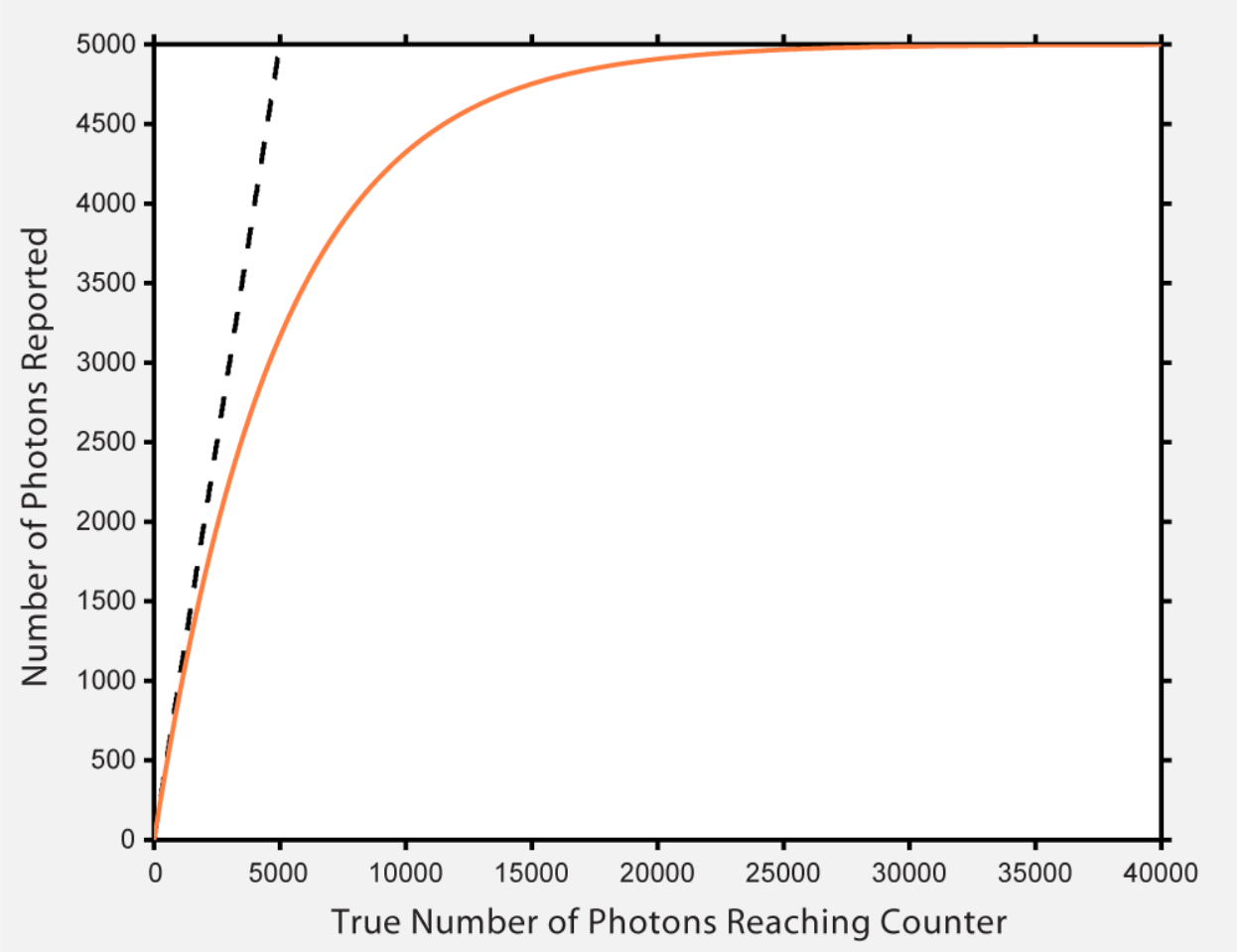

Figure 12: Monte Carlo model comparing the true number of photons delivered in a 100 μs window to the apparent number of photons reported by a photon counter than can register only one pulse per 20 ns bin assuming a uniform Poisson process. The dashed line indicates the expected number of counts for a one-to-one process.

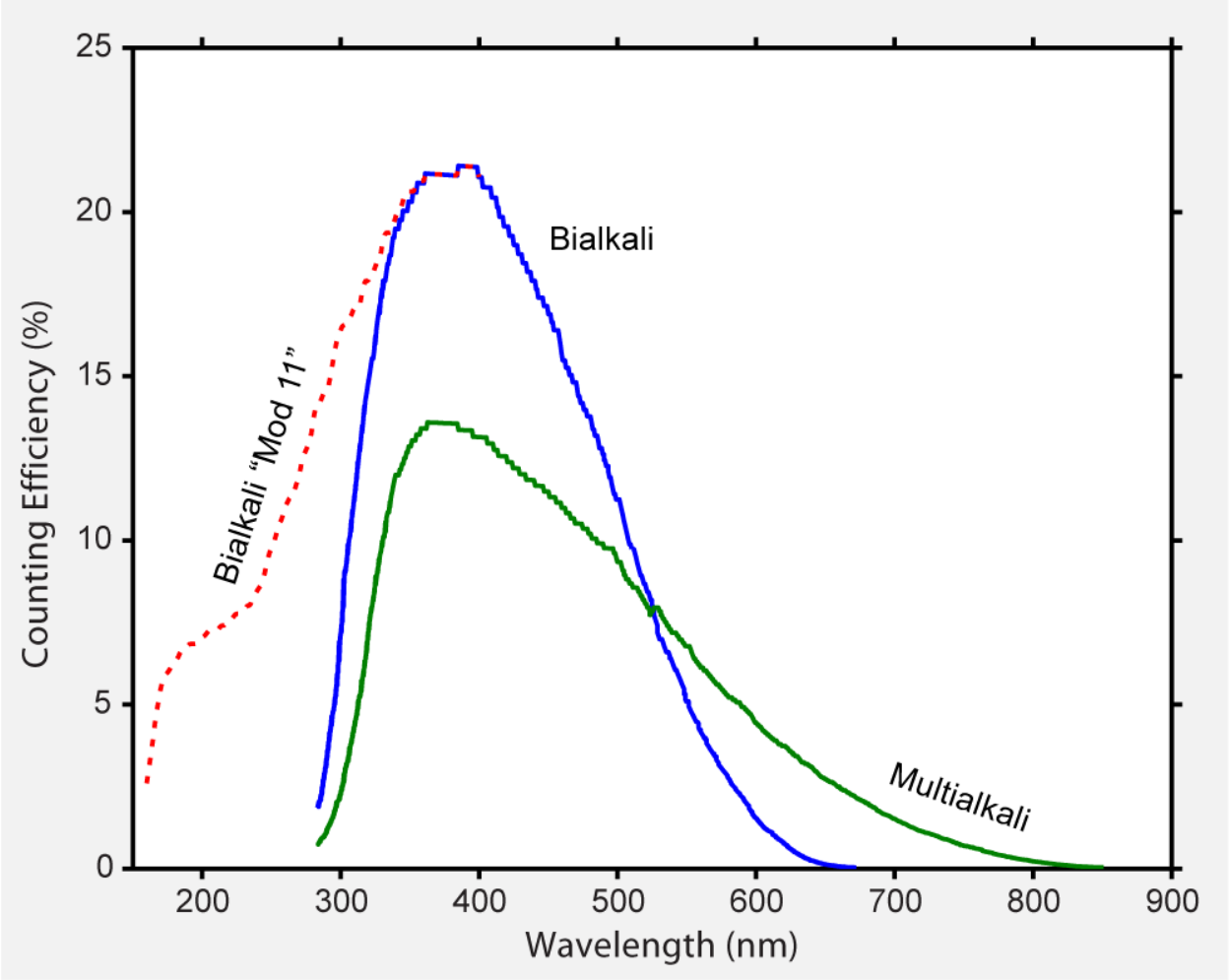

Figure 13: Counting efficiency of the photon counters versus wavelength. Multialkali counter is shown in green and bialkali with borosilicate glass window is in blue. The dashed red line is an estimation for the increased visible range of the HC-135 mod 11 tubes based on comparison to modern counters with UV glass installed since no factory record is available for the "mod 11″ type.

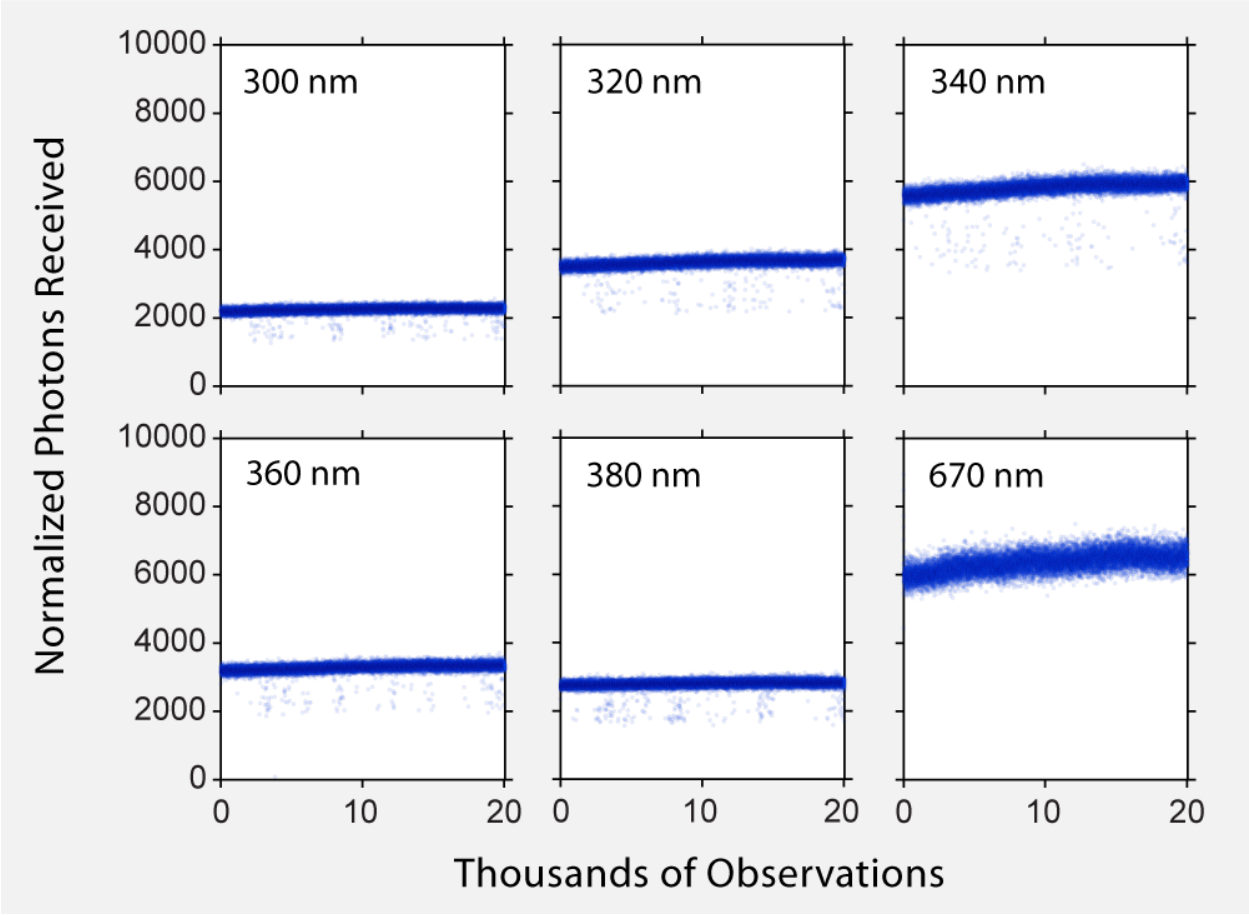

Figure 14: Variability in first six photon counter measurements across 20000 samples on a fixed ice target. In this plot, normalized photon counts refers to the number of photons received after adjusting for fluctuations in laser power and counter saturation effects (see Sections 2.3.1 and 4). However, this plot does not include adjustments for the transmissivity of filters or counting efficiency (shown subsequently in Figure 24), and hence this plot reflects received intensity not emitted intensity. Individual measurements are plotted in a semi-transparent blue so that outliers appear lighter than the primary population. We note that approximately 0.5% of the measurements in the HC-135 mod 11 channels (300-380 nm) show a negative excursion of up to 50% of their nominal value. Those negative excursions are uncorrelated from channel to channel. Discounting those low values, we note that the typical measurement population has a standard deviation of 2.2-3.2% of its mean. The seventh channel, 710 nm, is omitted because it was essentially zero for the selected target and so its fluctuations are not informative. The slight long-term trend shown in the above plot is assumed to reflect chemical alteration in the target as a result of long-term exposure to 224 nm radiation.

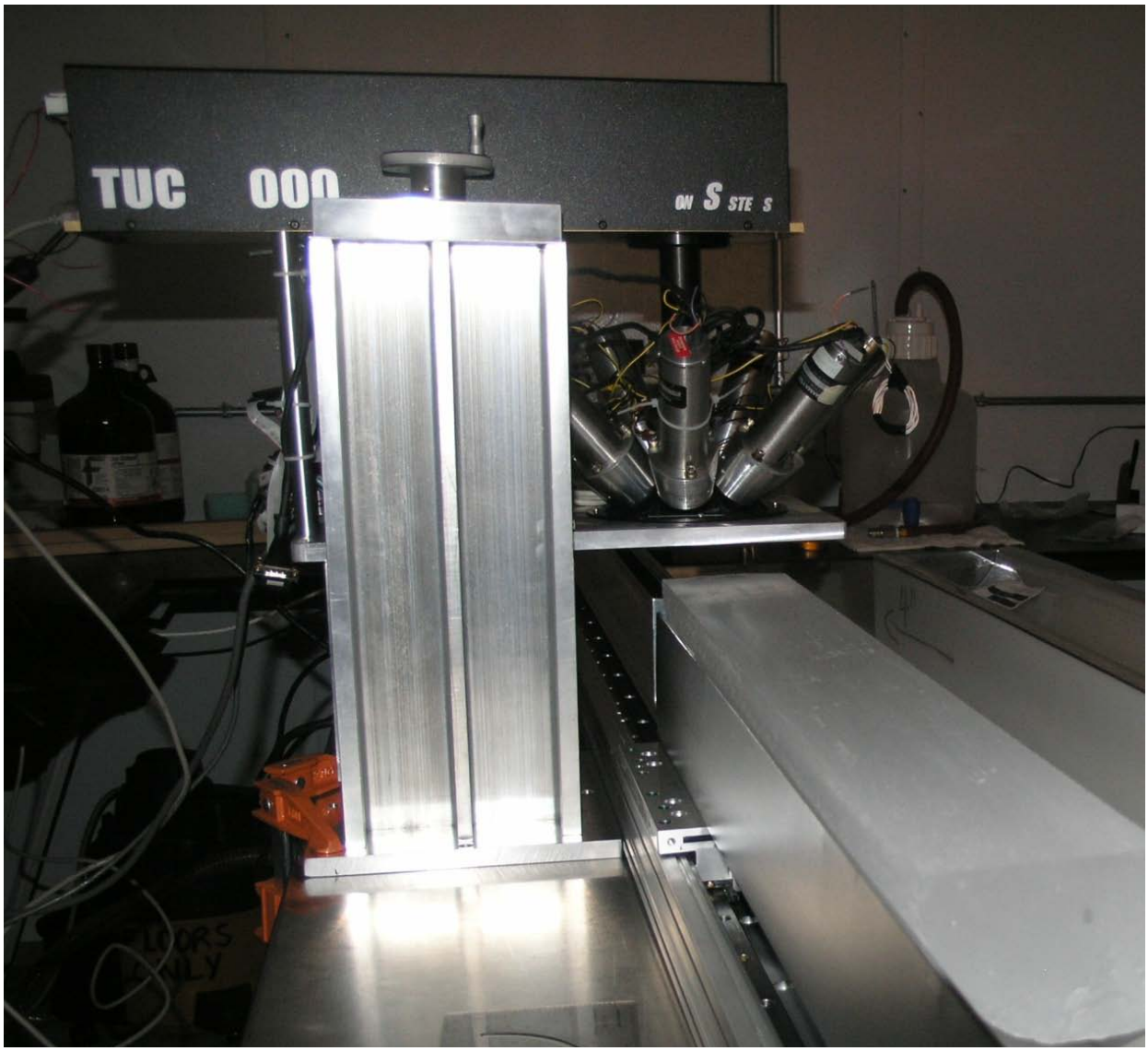

Figure 15: BFS configuration at NICL. The vertical Velmex stand is immediately visible. It supports the BFS system as it is suspended over a translation stage which holds the ice and moves it smoothly under the instrument. The TUCS laser system is visibly suspended above the photon counting rig.

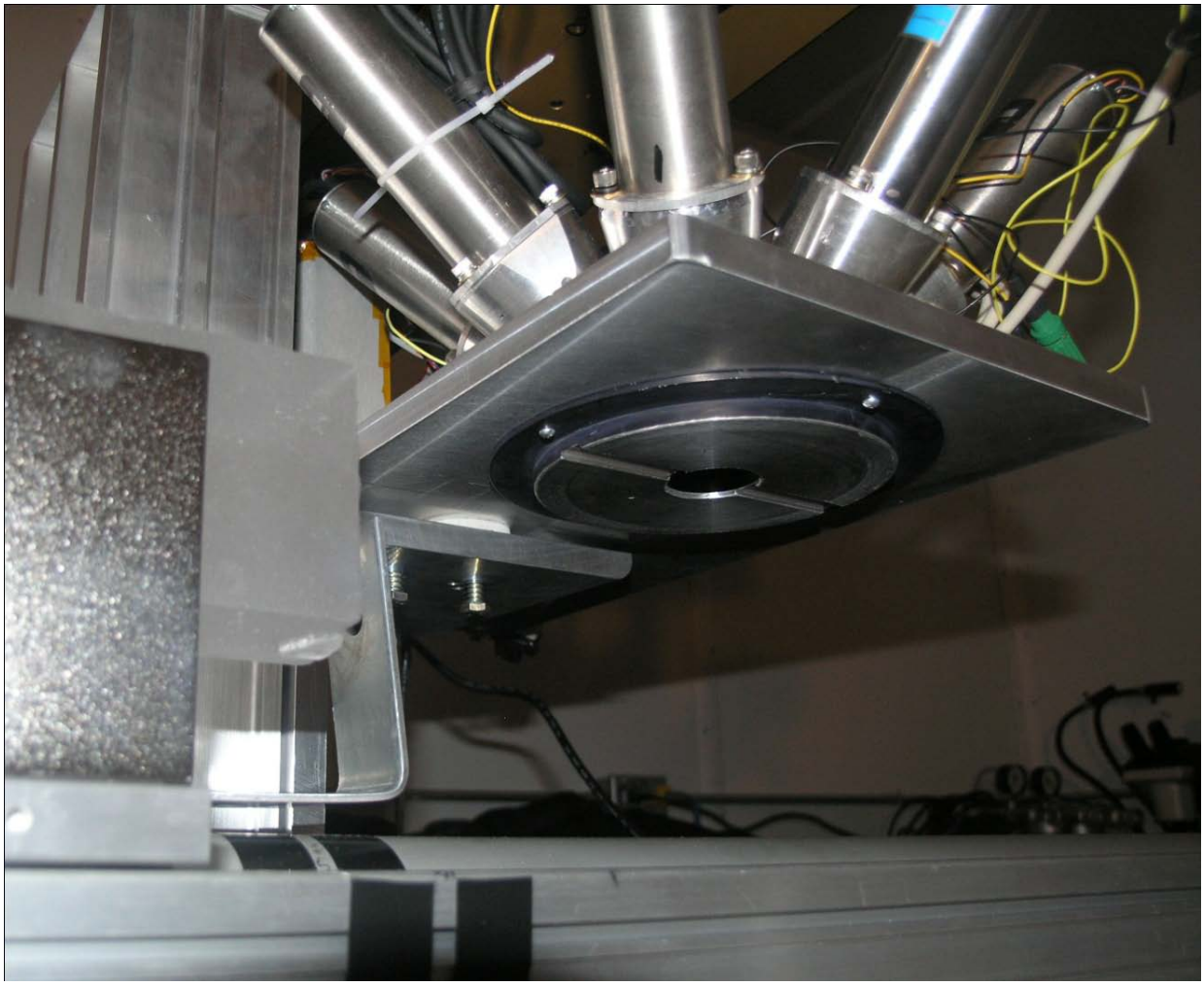

Figure 16: Close-up of the BFS showing the “dish” at the underside of the instrument which serves as the final viewing port. Also visible is ice moving from left to right on a stainless steel tray towards the BFS. The vertical height of the instrument is adjusted so that the ice passes 1-2 mm below the exit port in the dish.

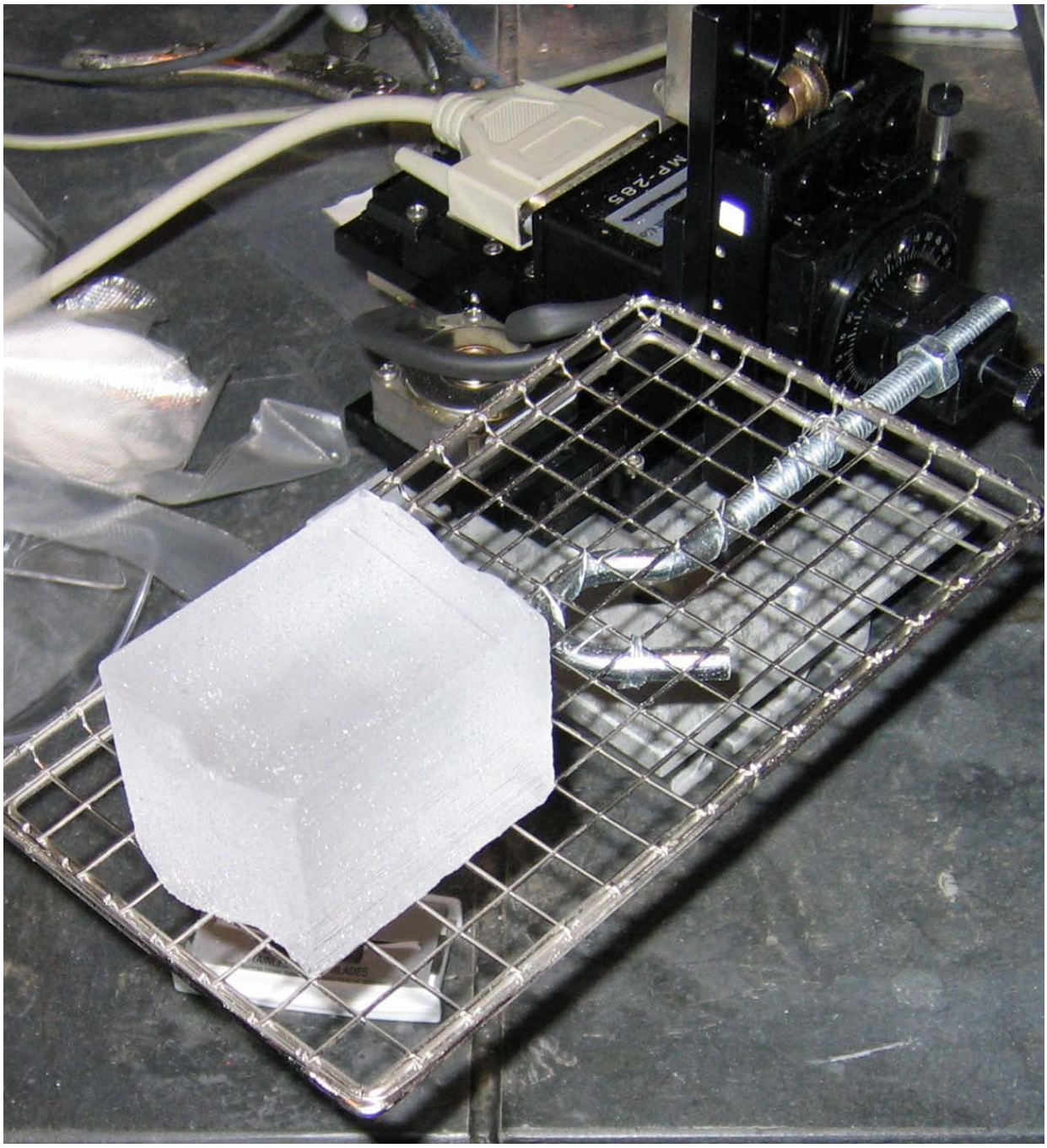

Figure 17: Two-dimensional scanning configuration. The MP-285 micromanipulator is visible in the background while the ice is placed on the wire frame stage. The entire platform is then positioned under the BFS and moved in two directions to create the raster scan images.

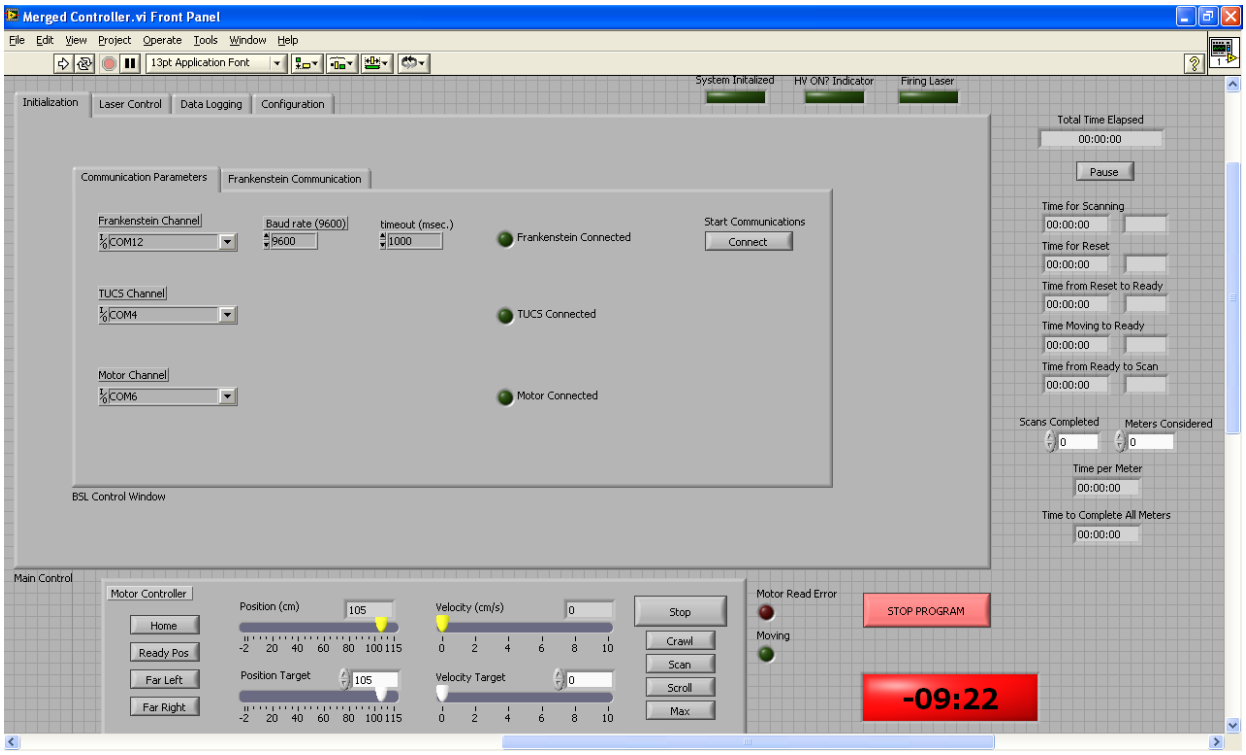

Figure 18: Topmost control window for the BFS software, as configured at startup. The communications panel occupies the main tab. At the bottom is the motor control panel (expanded in Figure 22) and stop program button. At the right are work-flow timing diagnostics that are largely unused in the present operation. Program operation begins by pressing the forward arrow on the menu bar.

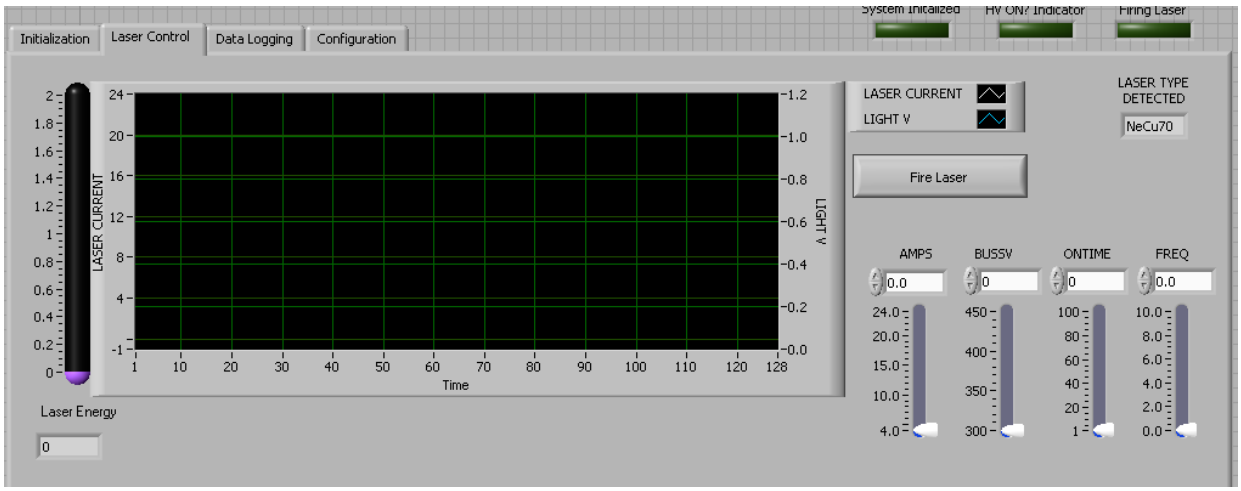

Figure 19: Laser control panel. The primary plot of this panel is a diagnostic window that shows μs time series of the laser power (uncalibrated units) and the laser driving current (A) for the last laser pulse (same as Figure 6). At left is a calibrated measurement of the integrated laser power (μJ). The "Fire Laser" button allows for diagnostic test firing, while the sliders at right allow for configuration of laser settings.

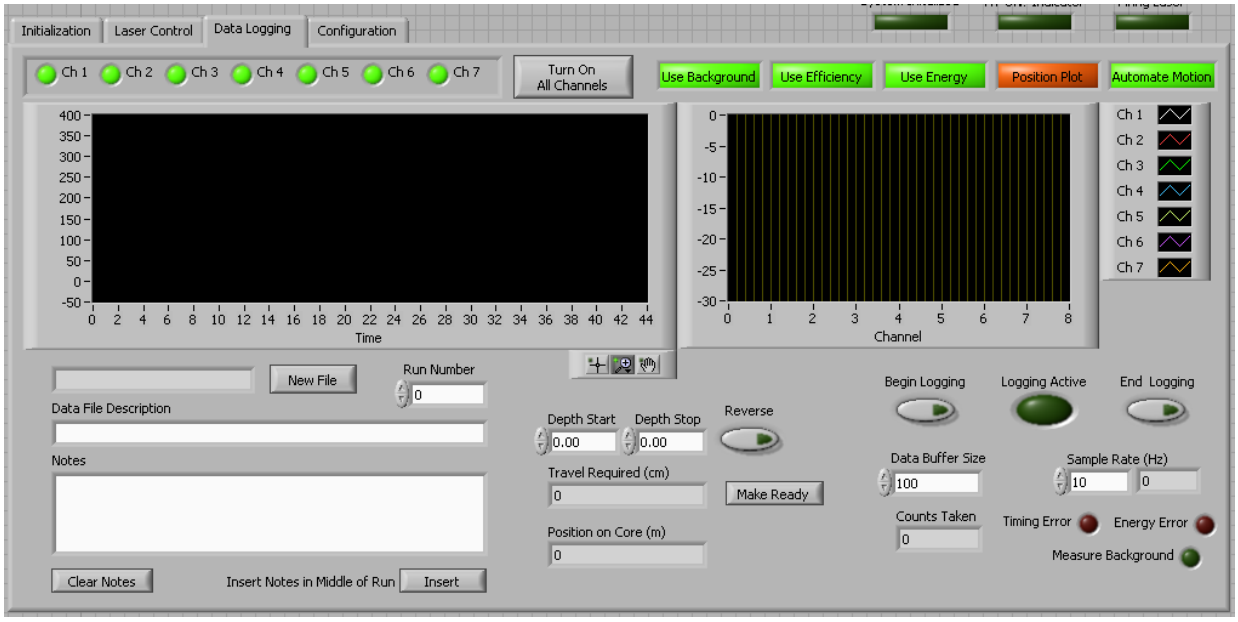

Figure 20: Data Logging Panel. This is the primary interface used during data acquisition (described in Section 3.3). At left is a time / depth display of collected data, while at right spectral plot of the seven channel intensities during the most recent laser pulse. Lower left provides text fields for describing the current data set. The center controls records ice core length parameters and display current position during data runs. Finally, the lower right provides controls for beginning and ending runs and well as performance diagnostics.

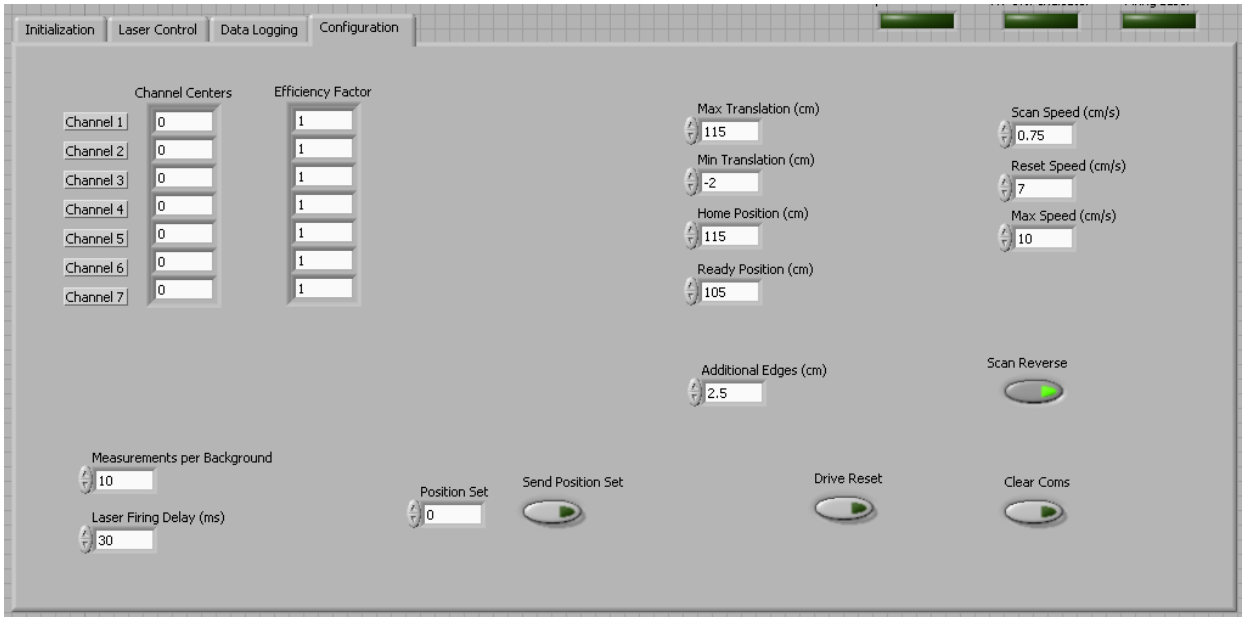

Figure 21: Configuration Panel. Allows configuration of various operating parameters described in Section 3.5.

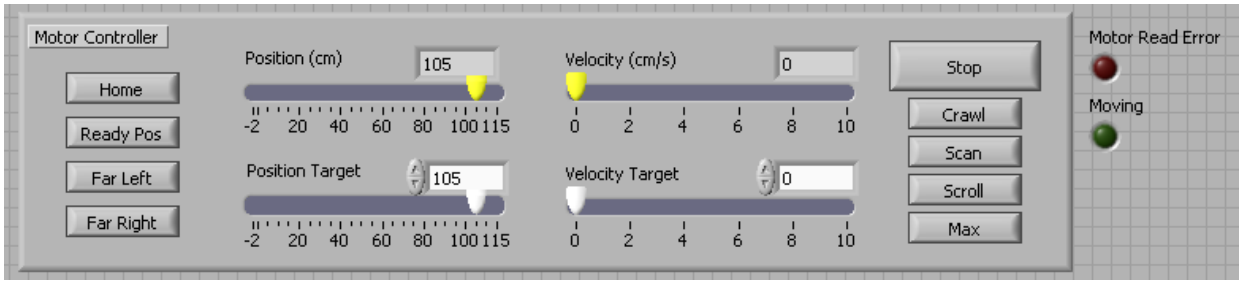

Figure 22: Motor Control Panel. This panel is visible at the bottom of the main display and available during all actions. It provides direct control of the translation stage and real-time feedback on its position and velocity. The topmost sliders are read-only indicators noting the current position of the stage and its velocity. The lower sliders provide direct control of the system. To the degree that it is possible, the stage will immediately attempt to adjust its location and speed to match new settings when the lower sliders are repositioned. Control buttons at the left and right provide a collection of preset positions and velocities.

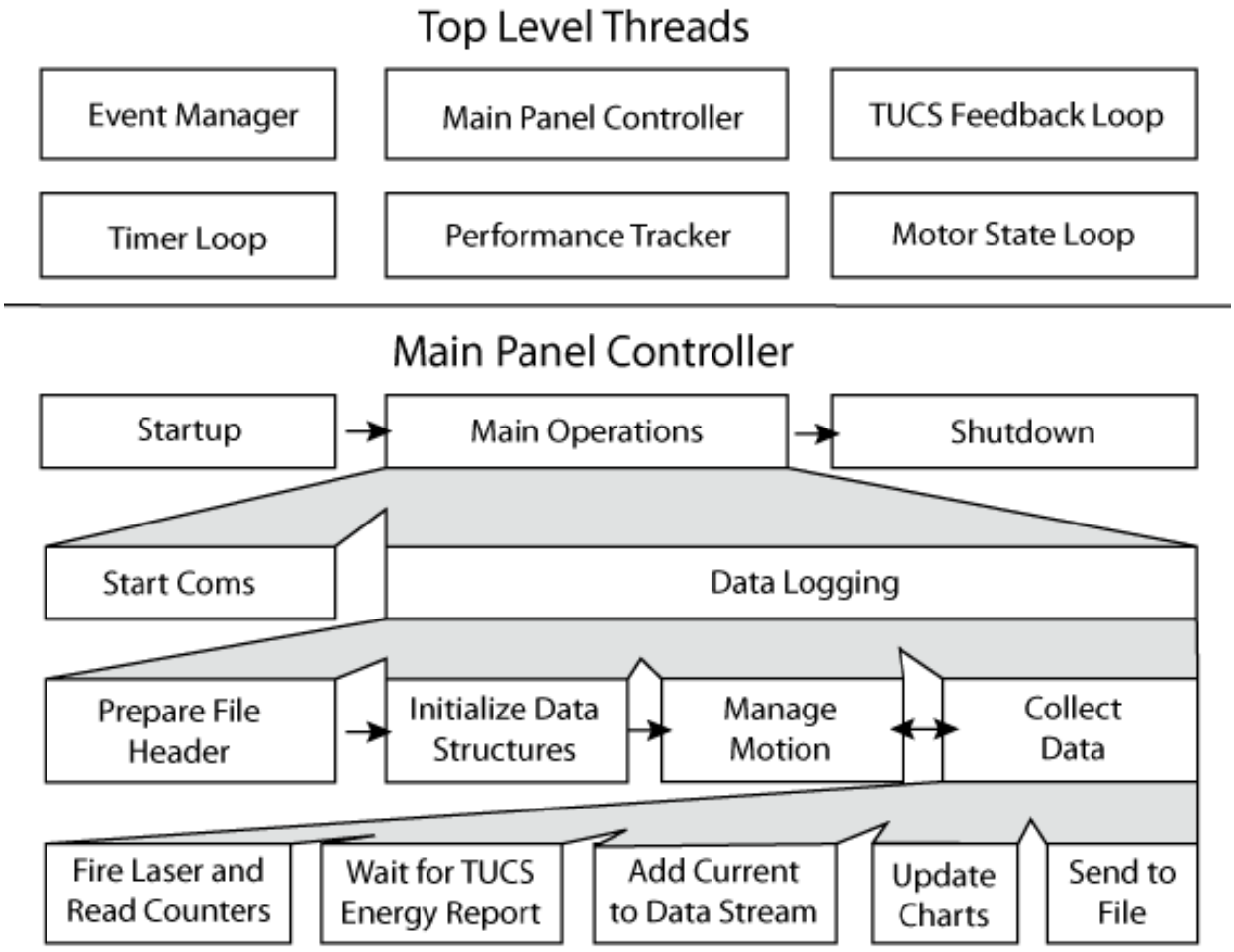

Figure 23: Schematic of Labview Program Flow, described in Section 3. Top panel notes the six independent top-level threads that operate within the BFS control software. The lower panel provides a schematic of the operations and workflow performed by the Main Panel Controller. See text for additional details. Full source code appears in the Electronic Supplement.

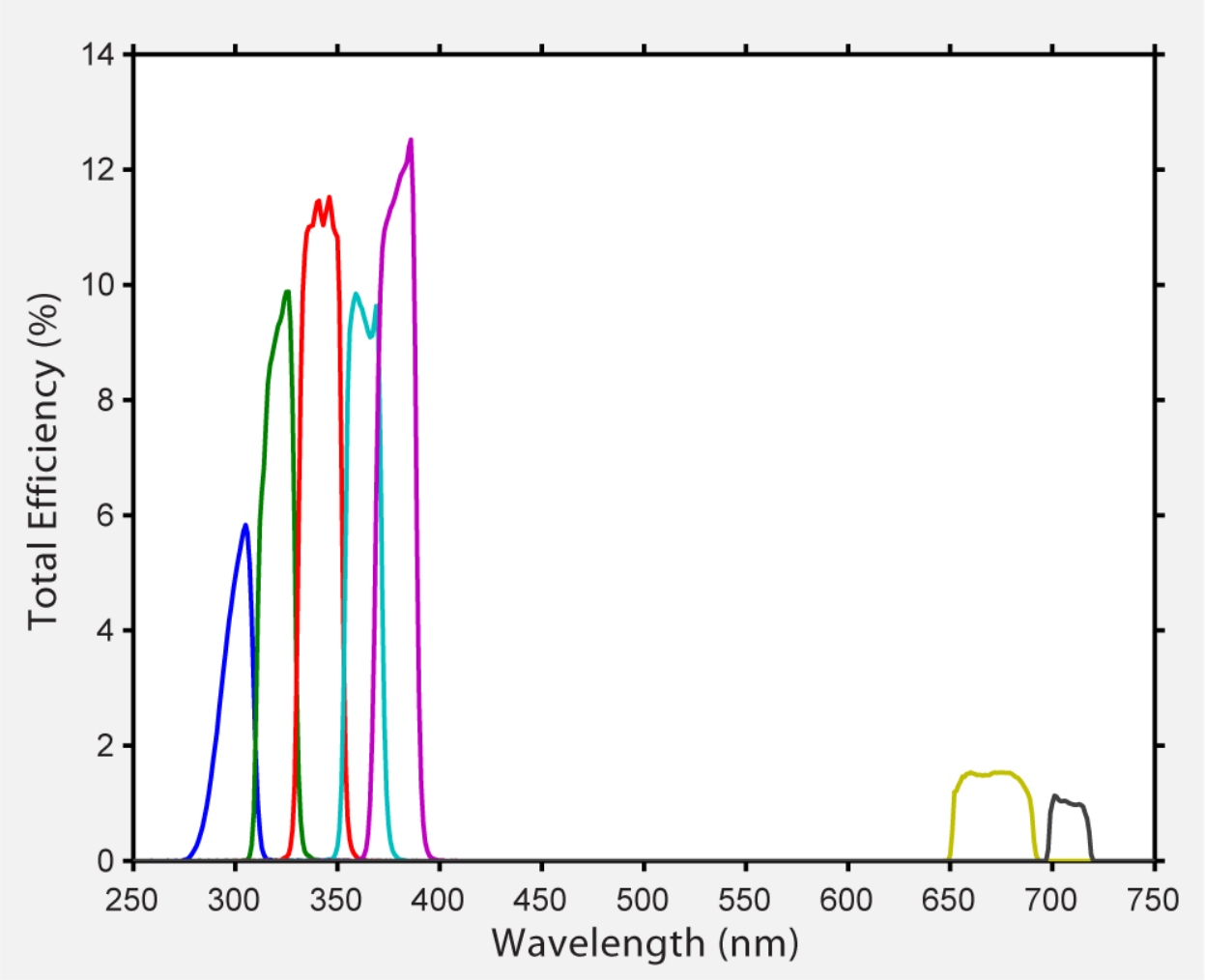

Figure 24: Theoretical total efficiency – number of photons counted as a fraction of the number of photons emitted in the direction of the photon counter – expressed as a function of wavelength. This figure is based on a convolution of the information in Figure 7 and Figure 13.

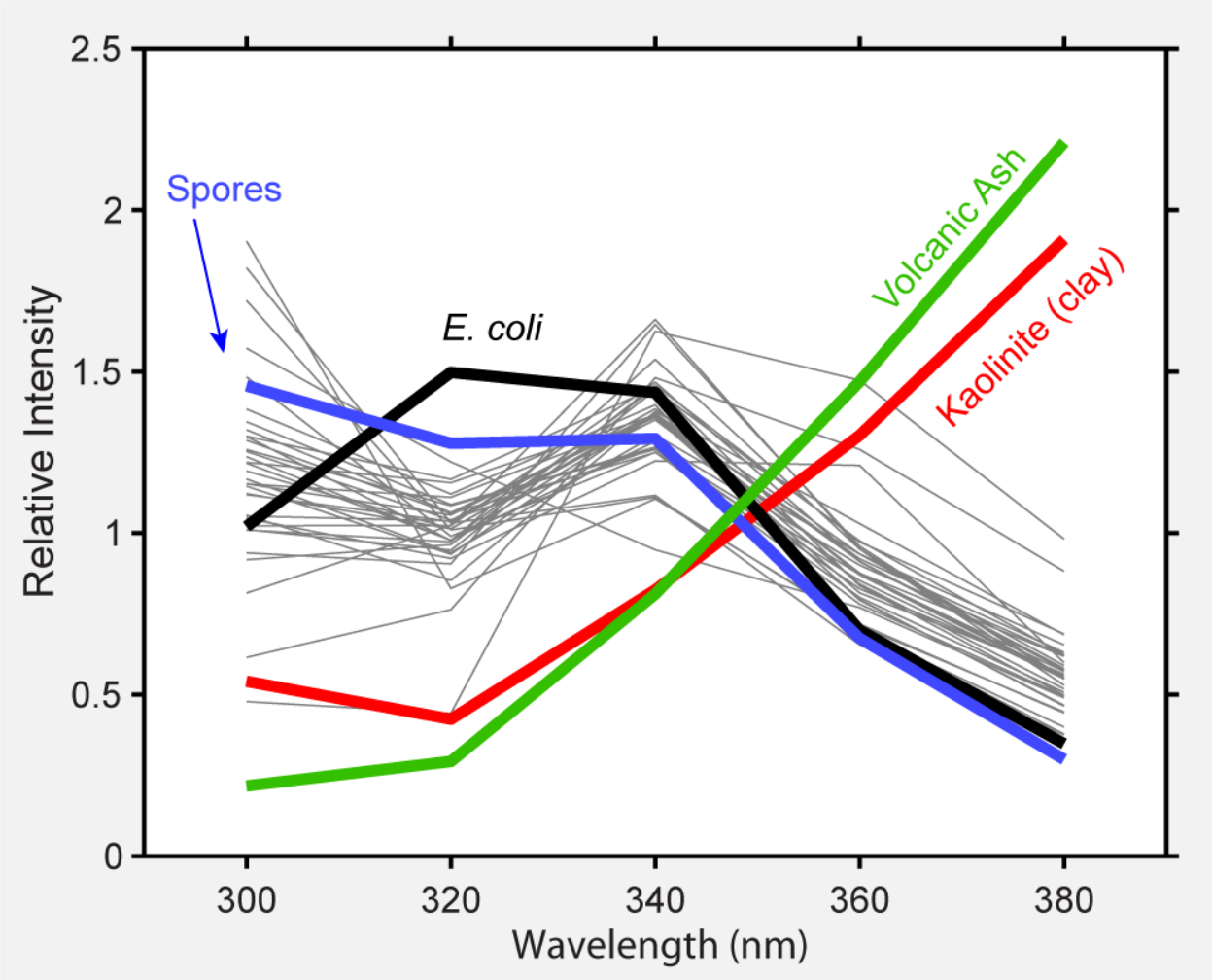

Figure 25: Comparison of 2007 TUCS spectra to standards prepared with the same instrument (a predecessor of the BFS, see Section 2.1). The thin gray lines are 34 fluorescence spectra from WAIS Divide, Siple Dome, and GISP2D. Each spectrum was produced by taking a mean of the above background fluorescence spikes from a scanned ice core segments that was 10 to 100 cm in length. To facilitate simple comparison, each spectrum was then scaled so that its average intensity across the five channels was one. Since the spectra are all similar, it provides evidence that the fluorescent components within ice cores are likely to be similar from depth to depth and location to location. These spectra were compared to a set of reference spectra taken with the same instrument: *E. coli* doped into laboratory ice, a bacterial endospore solution doped into ice, a solid sample of volcanic ash, and a solid sample of Kaolinite clay. The organics are clearly more similar to the measurements than the mineral samples, though differences remain. In addition, though all spectra are plotted with relative intensity equal to one, we also note that the intrinsic intensity per absorbed excitation photon of the mineral samples is 100-1000 times lower than the organics. See Section 4.1 for additional discussion of this plot. Also, note that the above plot reflects only the TUCS response to these samples and should not be considered reliable as an absolute standard. For a general discussion of limitations and problems with the TUCS implementation see Section 2.1.

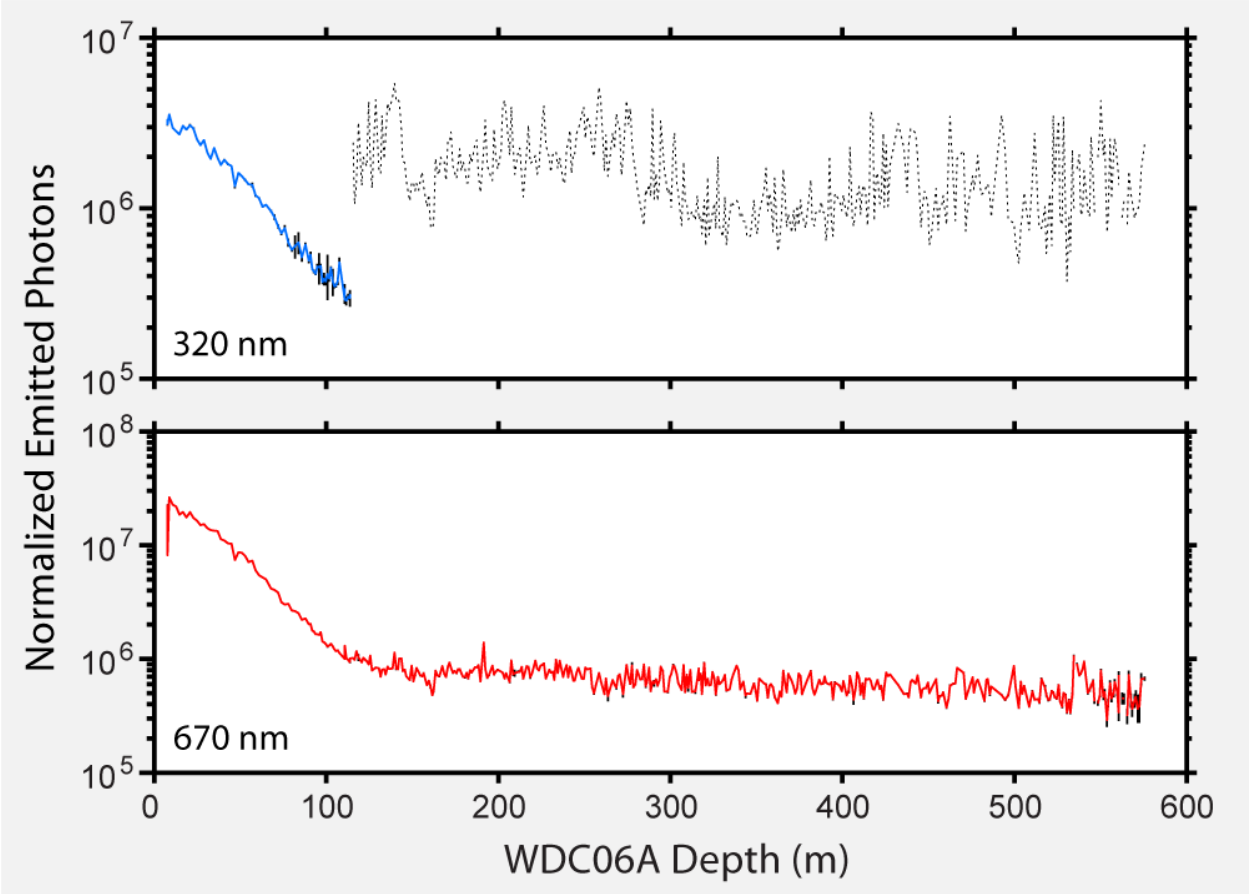

Figure 26: Summary of WDC06A fluorescence taken in 2008. Each core segment scanned, involving up to 1300 measurements per meter, is condensed to a single average value for that segment. The top panel shows emissions at 320 nm. Down to 114 meters the core was dry-drilled and the emissions, shown in blue, are assumed to be a reliable reflection of the ice. Below 114 m, the short wavelength spectra are dominated by a contribution from the drill fluid and its fluorescing constituents, shown here as a dashed gray curve. The bottom panel shows the equivalent data at 670 nm, though in this case the record is continuous as the drill fluid does not fluorescence at 670 nm. In both panels, vertical black bars are added to indicate the 1-sigma uncertainty in the per segment averages. In most cases, the uncertainties are smaller than can be resolved visually at the scale of this plot.

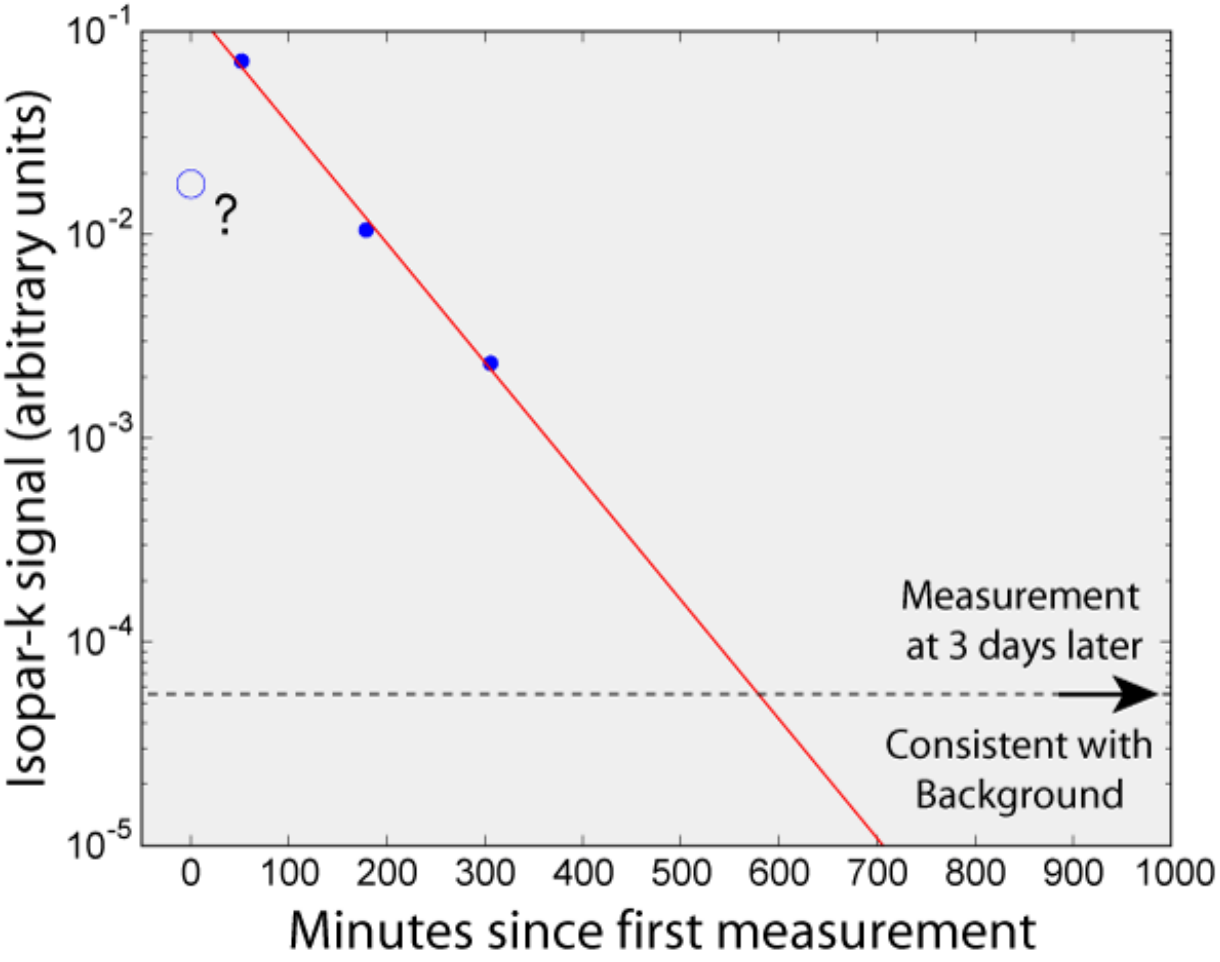

Figure 27: Study on the dissipation of drill fluid residues based on drenching a solid block of ice in Isopar-K, wiping it "dry", and allowing it to sit in an open box at -25 °C. The very first measurement was anomalous perhaps because it was taken immediately after the ice had been wiped down and the resulting residues were not evenly distributed yet. The following three measurements were all consistent with an exponential decay with a half-life of order an hour. When we returned after a weekend, no detectable residues remained, which is consistent with any half-life shorter than about 7 hours.

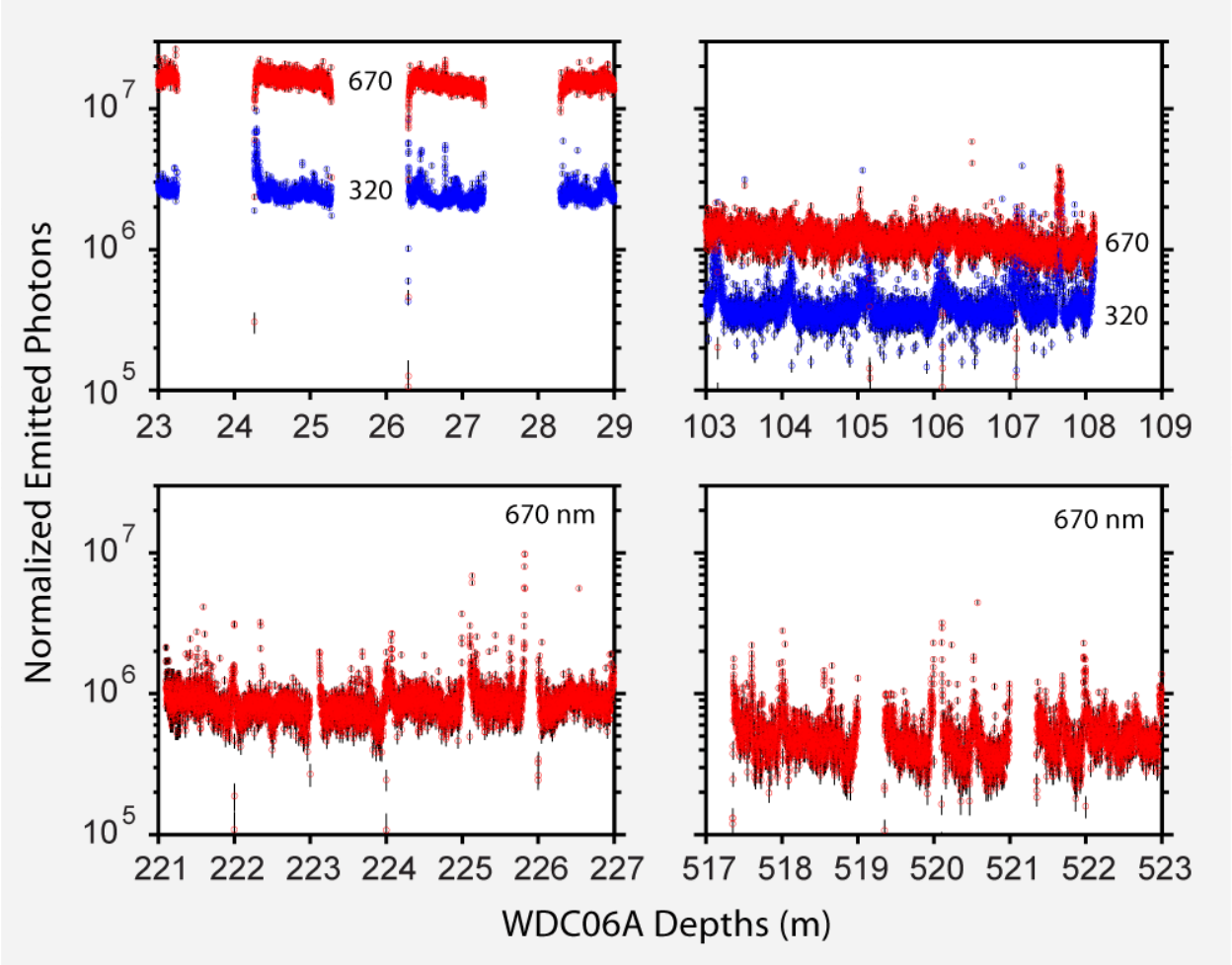

Figure 28: Representative intensity versus depth curves showing individual measurements for selected portions of WDC06A. All four panels are plotted on the same vertical scale to make direct comparisons possible and note the fall-off versus depth. The blue and red curves show the 320 and 670 nm fluorescence respectively. The 320 nm channel is not included in the lower two panels because those two depths were drilled with drill fluid and hence the signal at 320 nm is heavily contaminated (i.e. Figure 26). Error bars are included as vertical black lines, but as the typical error bar is only a few percent they can be difficult to resolve at this scale. In addition to considering the evolution of the bulk trend, deviations from the trend are also of interest. The most common form of deviation is a localized positive excursions such as are visible at 26.9, 107.6, and 222.3 m

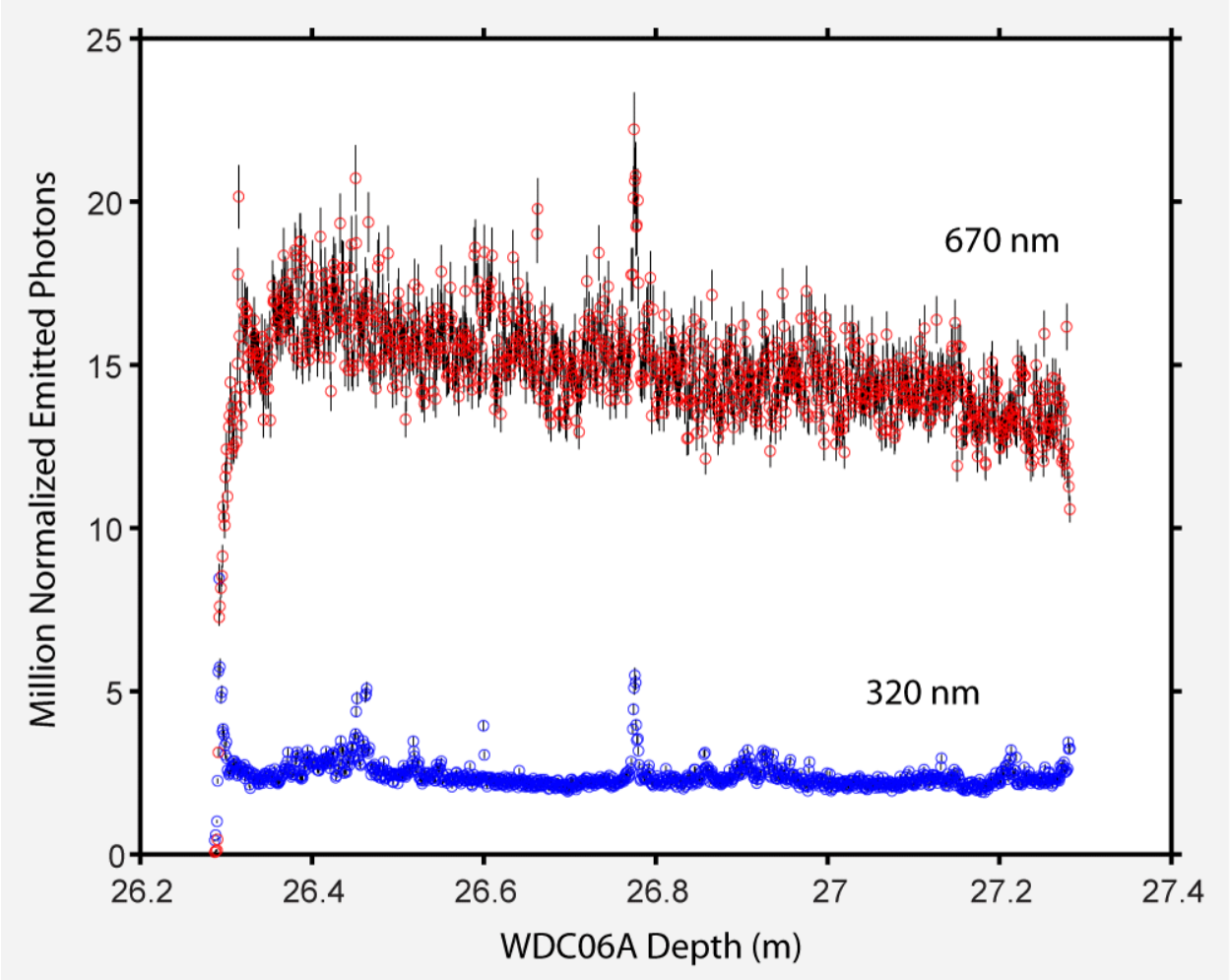

Figure 29: Detailed view of WDC06A scan at 26.8 m depth. Blue shows the 320 nm channel and red is the 670 nm channel. This piece was chosen in particular to show the narrow spike at 26.78 m lasting only a few mm. As is the case with many ice cores, most of the core appears consistent with a smoothly varying bulk trend within the limit of the observed statistical uncertainty. However, many cores exhibit one or a few localized spikes such as are observed here. We believe such spikes most commonly represent localized concentrations of microbes.

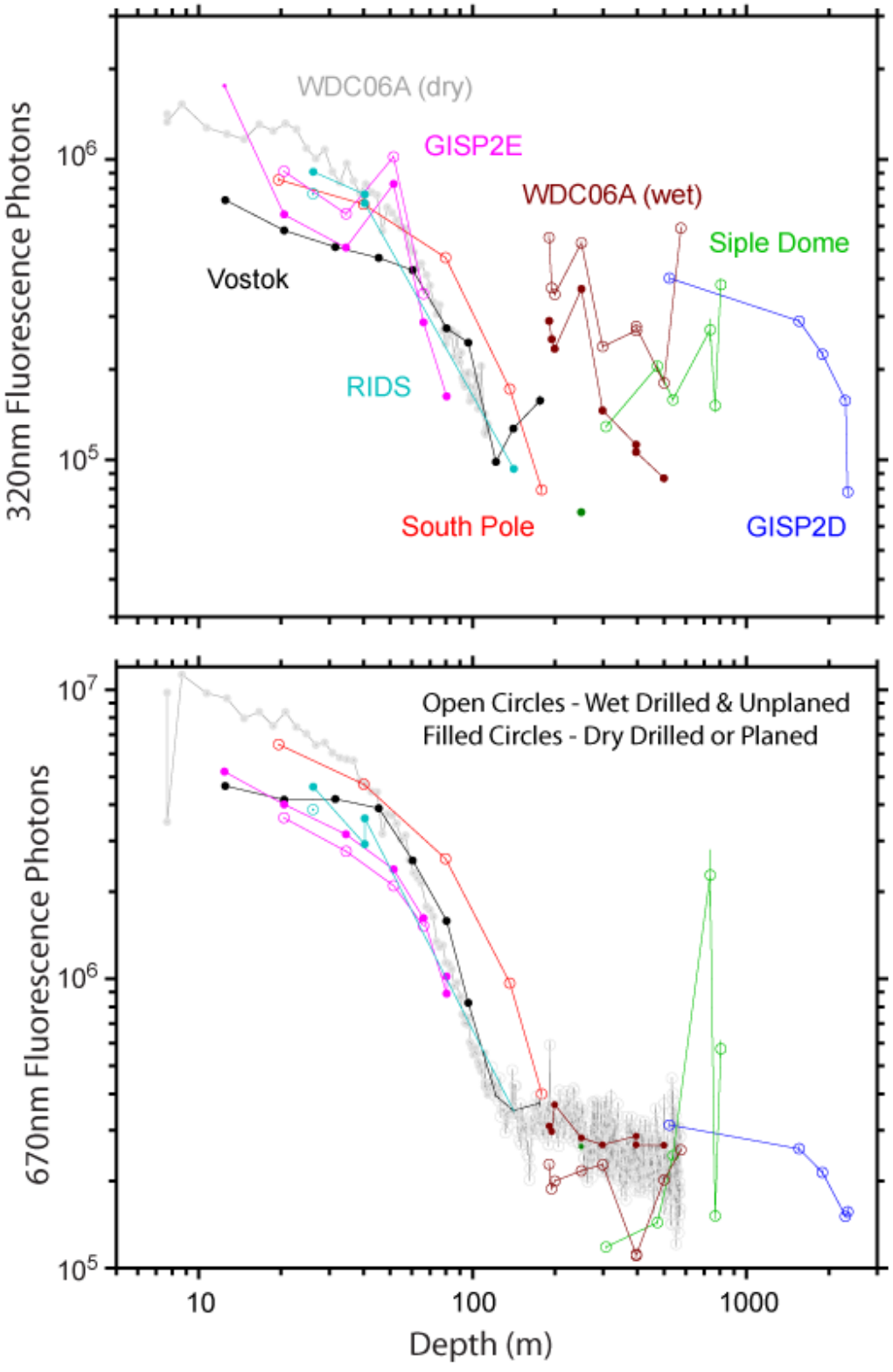
320nm Fluorescence Photons
10^6
10^5
WDC06A (dry)
GISP2E
WDC06A (wet)
Siple Dome
Vostok
RIDS
South Pole
GISP2D
670nm Fluorescence Photons
10^7
10^6
10^5
Open Circles - Wet Drilled & Unplaned
Filled Circles - Dry Drilled or Planed
10
100
1000
Depth (m)

Figure 30: Summary composition of all scanned ice core data. The plot shows per segment averages for 320 nm (top) and 670 nm (bottom) emissions. The filled circles represent core segments that were either dry-drilled or planed immediately before scanning. The open circles are core segments that were wet drilled and not freshly planed. The cores are labeled by core and identified in the top plot. A specific core may have both a filled and open circle trace. The data collected in 2008 from WDC06A is shown in gray. All other data was collected in 2009. Core segments which were less than 10 cm in length were not included as there was no way to compensate appropriately for potential edge effects (see Section 6.2.2)

Figure 31: Photographs of representative ice core segments from WDC06A used for detailed raster scanning (Section 5.3). Left: Deep, wet-drilled, optically translucent core segment identified as cut "DD06" showing fully dense ice with approximate dimensions 5x5x7 cm. Right: Shallow, dry-drilled core segment from "Stick B" showing firn. This piece is optically opaque due to multiple scattering from bubble and pores between grains. Approximate dimensions: 3x3x5 cm.

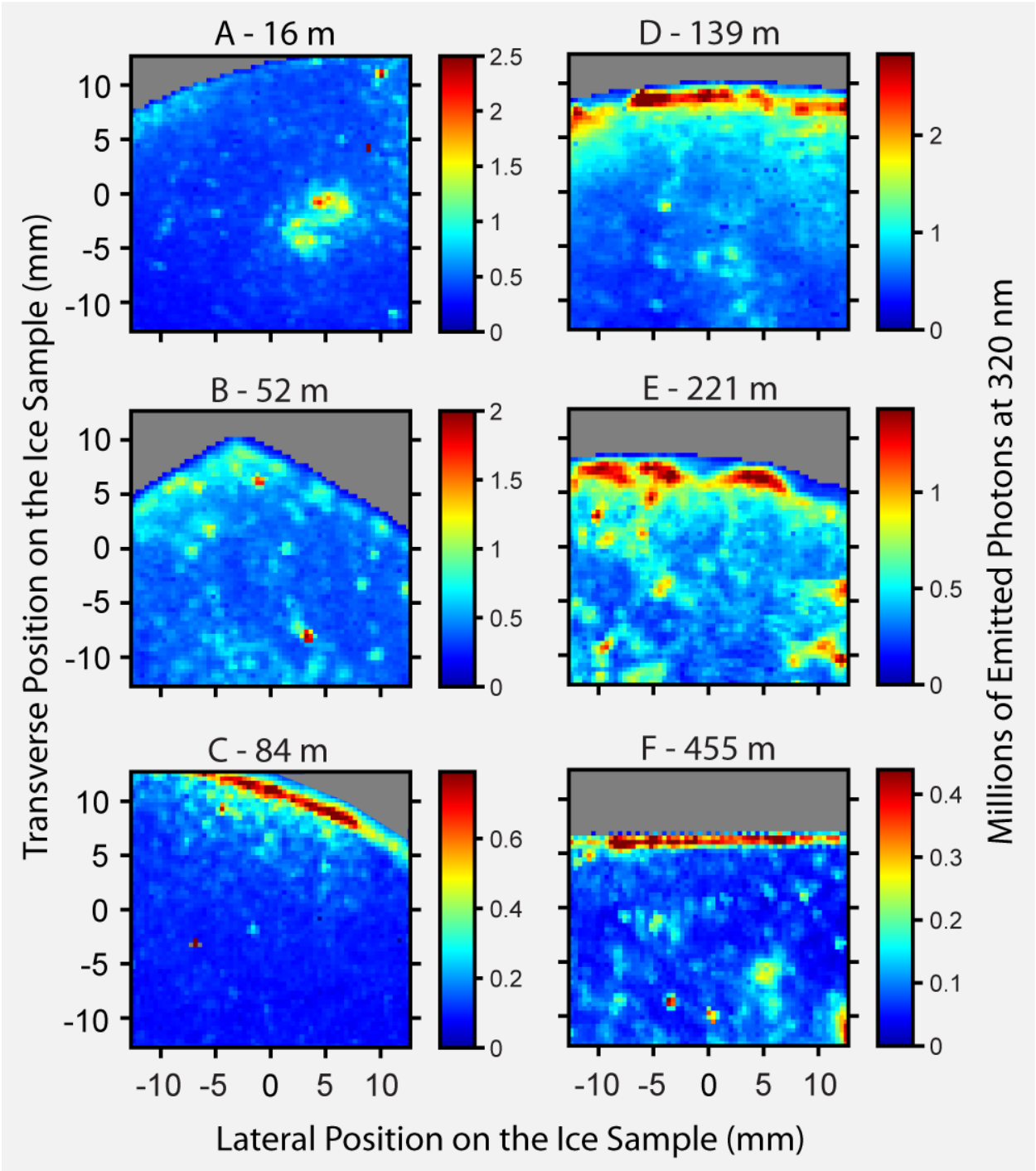

Figure 32: Selected two-dimensional raster scans made from WDC06A pieces (see Section 5.3). Each scan shows 1 square inch (6.5 cm^2) and intersects an edge of the ice core, indicated by gray coloration where the scanner travels beyond the ice surface. The three pieces from above 114 m (A, B, and C) were all dry-drilled. The 16 and 52 m pieces show low to moderate levels of excess fluorescence at the exterior surface while the 84 m piece shows quite high levels of near-surface contamination. The high levels of contamination on piece C are surprising since dry-

drilled pieces are generally expected to have been exposed to fewer contaminants. By contrast, we expect significant levels of drill fluid residue on outer surfaces of wet-drilled core, and this is confirmed in both the 139 and 221 pieces (D and E). We note that drill fluid appears to typically penetrate 2 to 5 mm into these cores. In the F panel, we show the intersection of the 455 m piece with an interior cut face. There appears to be substantial drill fluid redeposition on this interior cut surface, but the penetration is very shallow, only ~1 mm. Such redeposition appears to be extremely common as drill fluid on the exterior faces is able to migrate to interior sections. Localized packets of fluorescence, consistent with packets of microbes are observed at various locations on all scans.

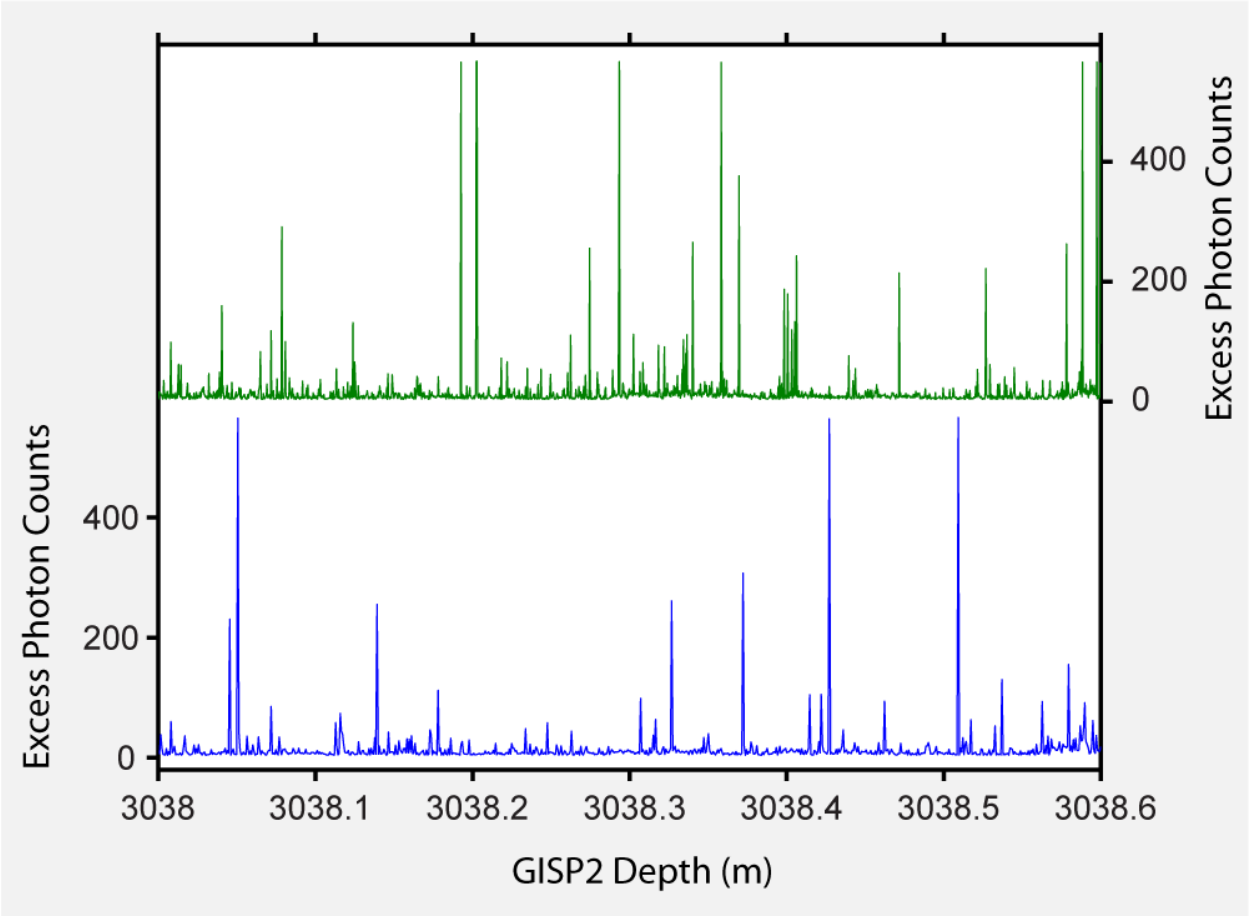

Figure 33: Comparison of two parallel scans laterally separated by 1 cm conducted along a GISP2 ice core at 3038 m depth using the TUCS instrument. Note the high degree of dissimilarity in the spike-like details. This implies that the spikes were caused by compact fluorescing objects with lateral dimensions much less than 1 cm, presumably packets of microbes similar to those observed in raster scanning (Figure 32). This instrument configuration used a highly focused excitation beam, comparable to that used in the raster scans, but different from the less focused beam used during most of the 2008 and 2009 scanning with the BFS. The choice to defocus the beam during the later scans was made in the hopes of capturing more large scale structure and fewer of the highly localized features shown here.

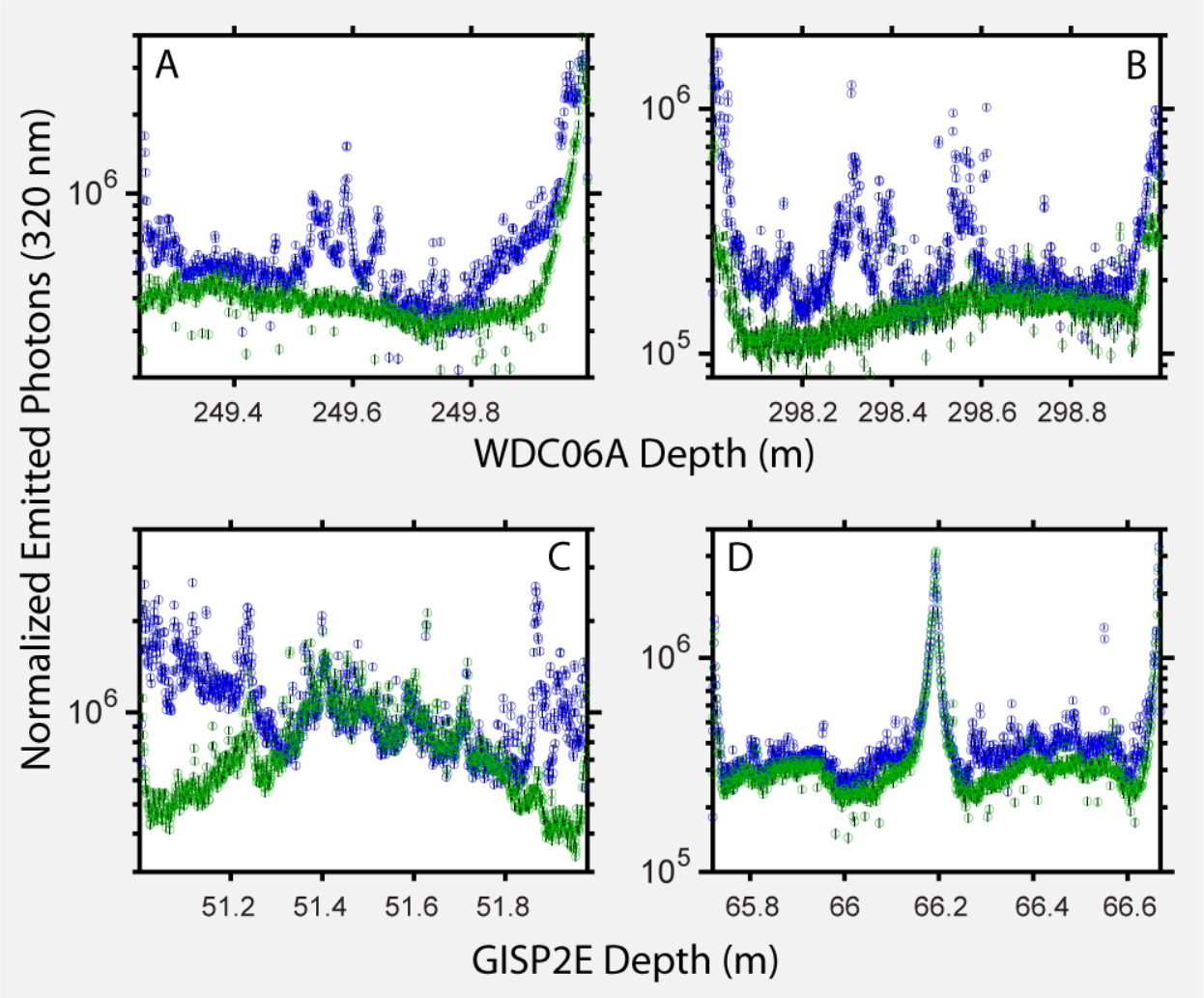

Figure 34: Comparison of planed and unplaned fluorescence emission at 320 nm from the wet drilled WDC06A ice core (A and B) and the dry-drilled GISP2E ice core (C and D). In every case the act of planing results in a lower 320 nm fluorescence intensity for at least some of the scan region (lower, green circles in each panel) than the uplaned measurements of the same ice (blue circles). The difference is significantly larger than the measurement uncertainty (vertical black lines). In general the, dry-drilled GISP2E core shows a smaller effect than the wet-drilled WDC06A core. It also appears that many of the localized vertical spikes seen on many cores may simply be surface contaminants that should be removed by planing. See Section 6.2.1.

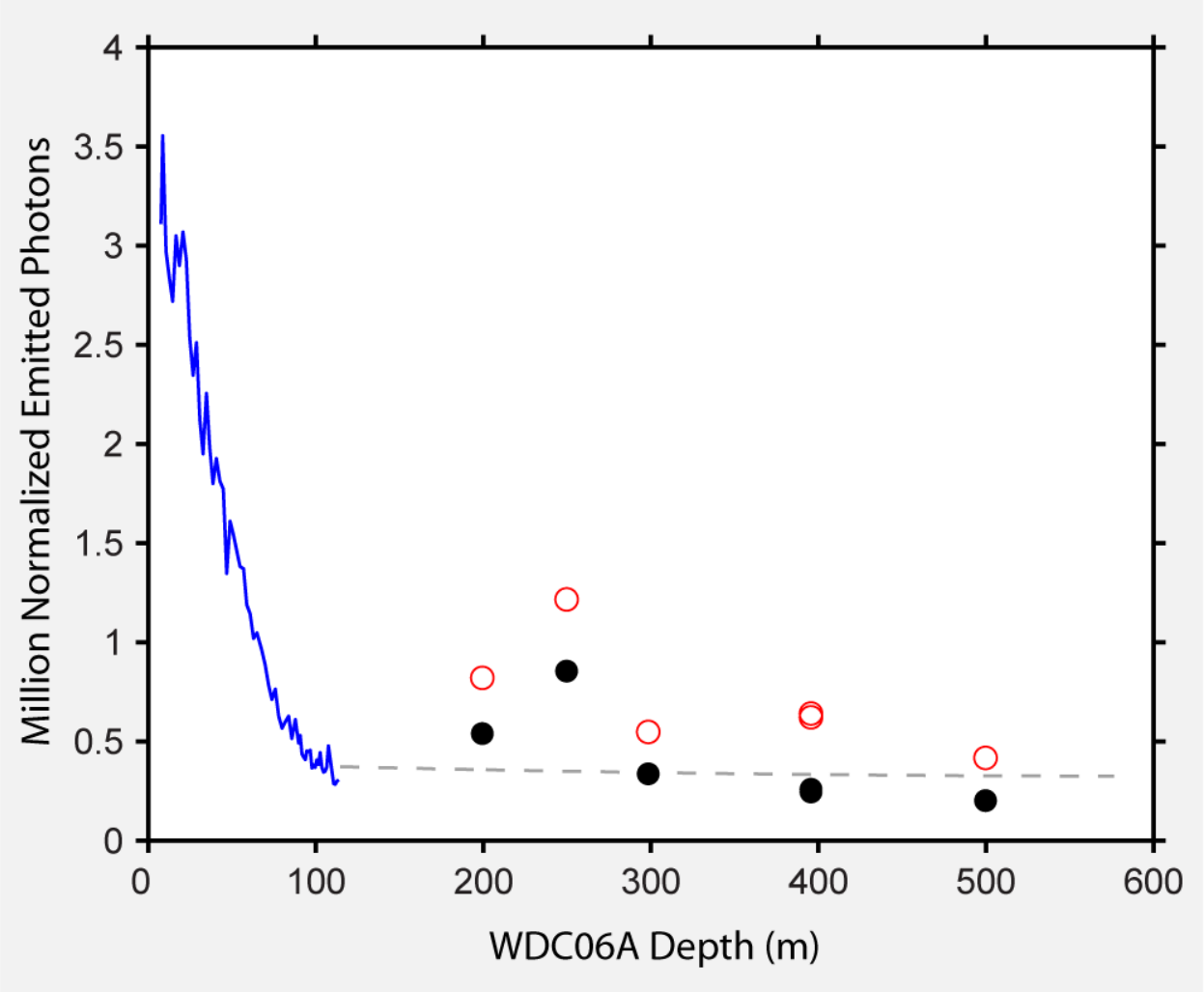

Figure 35: Shift in the mean fluorescence intensity in the 320 nm channel between planed (black, filled circles) and unplaned (red, open circles) WDC06A ice cores as measured in 2009. The blue curve is the similar 320 nm intensity measured in 2008 on dry-drilled core, and the gray, dashed line shows the estimated extension assuming it would follow the same pattern of decline as the 670 nm fluorescence. We assume that below 114 m, all of the unplaned surfaces are contaminated with drill fluid (see Section 6.2.1), and note that planing leads to a substantial reduction in 320 nm emission. However, of the six pieces considered in 2009, at least one (the 250 m sample) appears substantially elevated even after planing. Though this result is anecdotal, it suggests that even after planing significant contamination may remain, for example in microcracks that extend deeper than the typical ~1 mm planning effort.

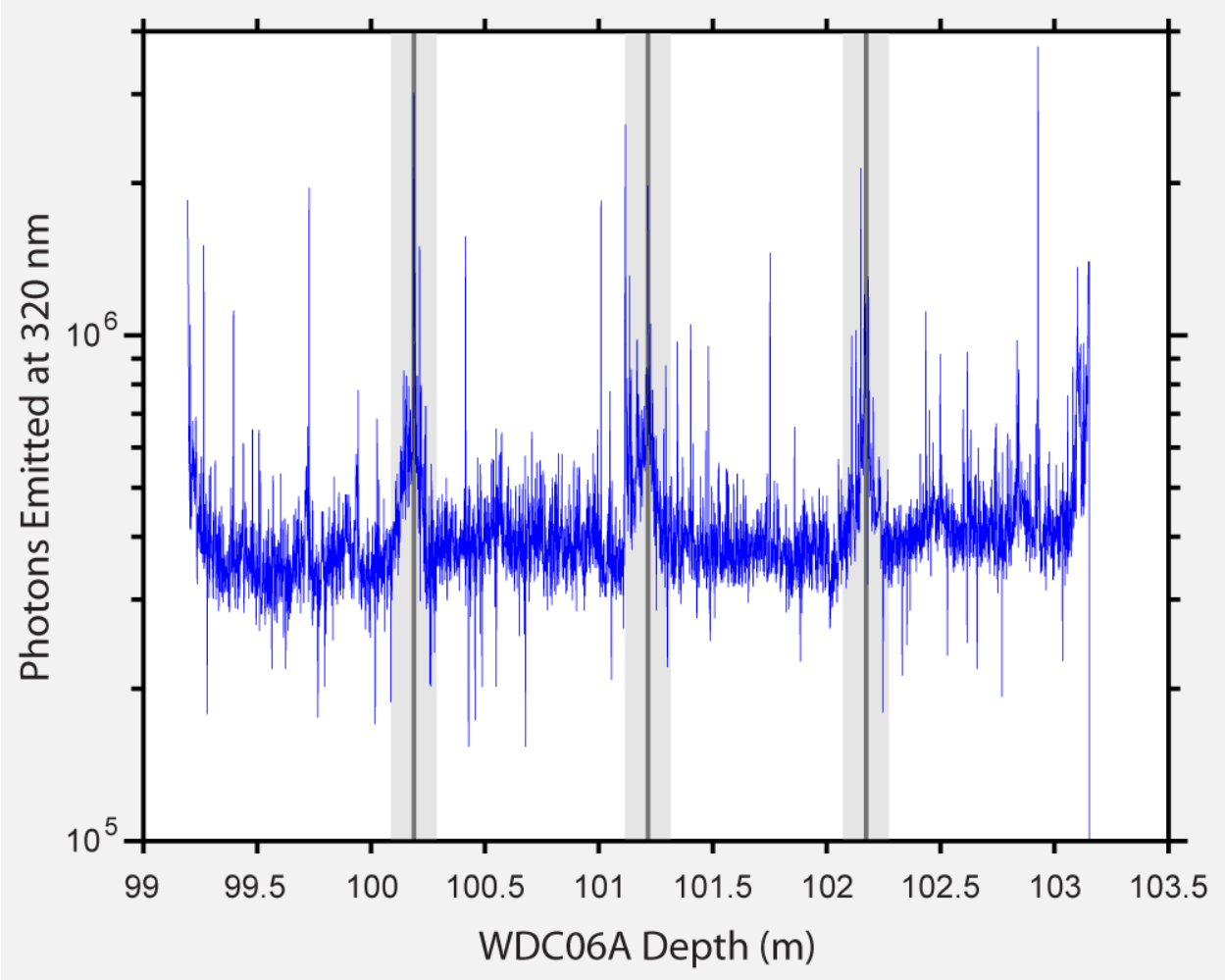

Figure 36: Fluorescence pattern at edges of core segments for selected pieces of WDC06A scanned in 2008. Black lines highlight the core cuts and gray bands indicate regions of ± 10 cm on either side of the cuts. As indicated, it is fairly common to see a 50-100% enhancement in fluorescence at core boundaries.

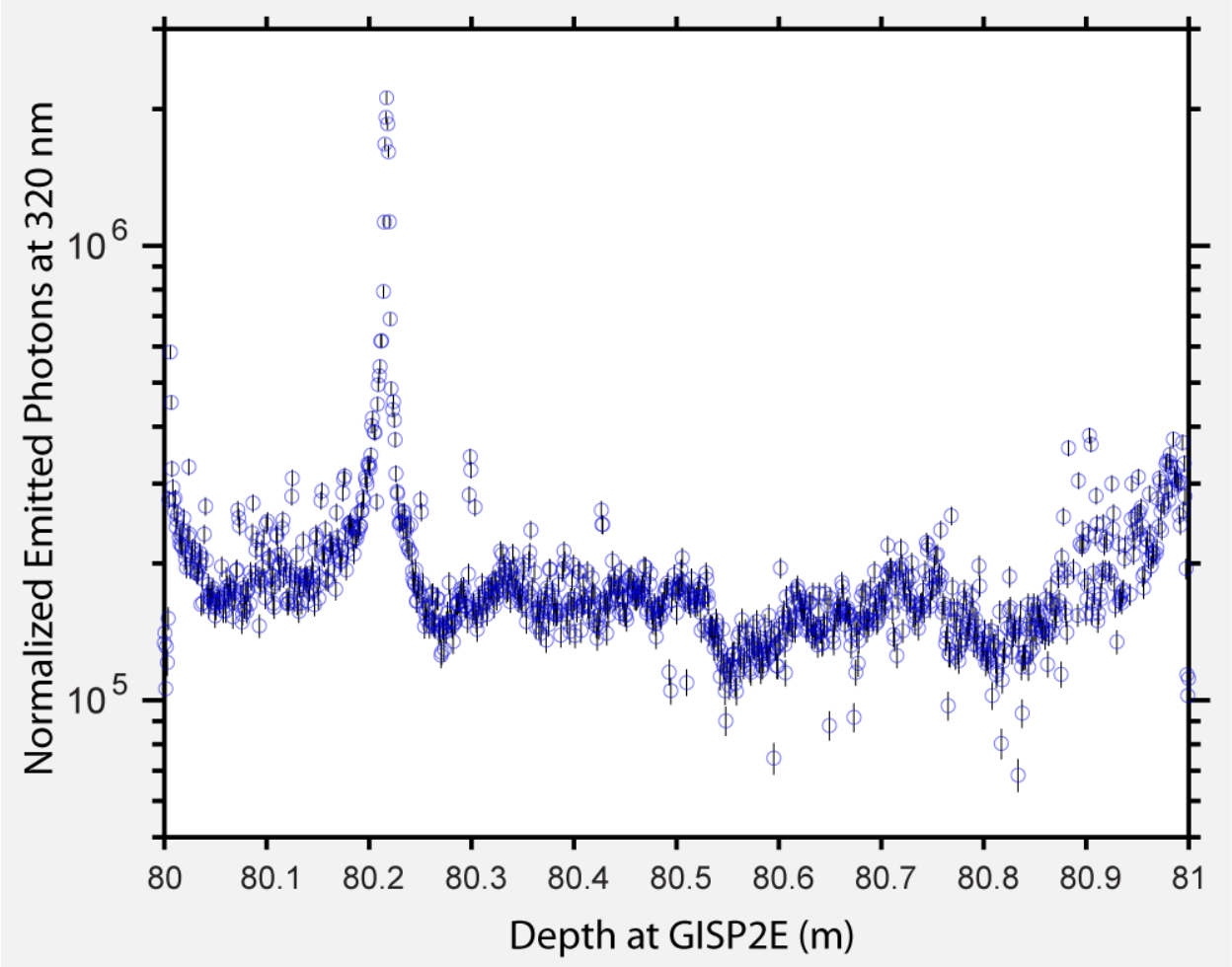

Figure 37: Planed GISP2E ice core at 80 m depth. The very large feature at 22 cm, associated with an order of magnitude increase in fluorescence, is caused by a healed fracture in the ice core. As this core was dry-drilled, this excess is not related to drill fluid. Rather, it is believed that this feature is a consequence of variations in the optical properties of the ice, see Section 6.2.3 and 6.3.

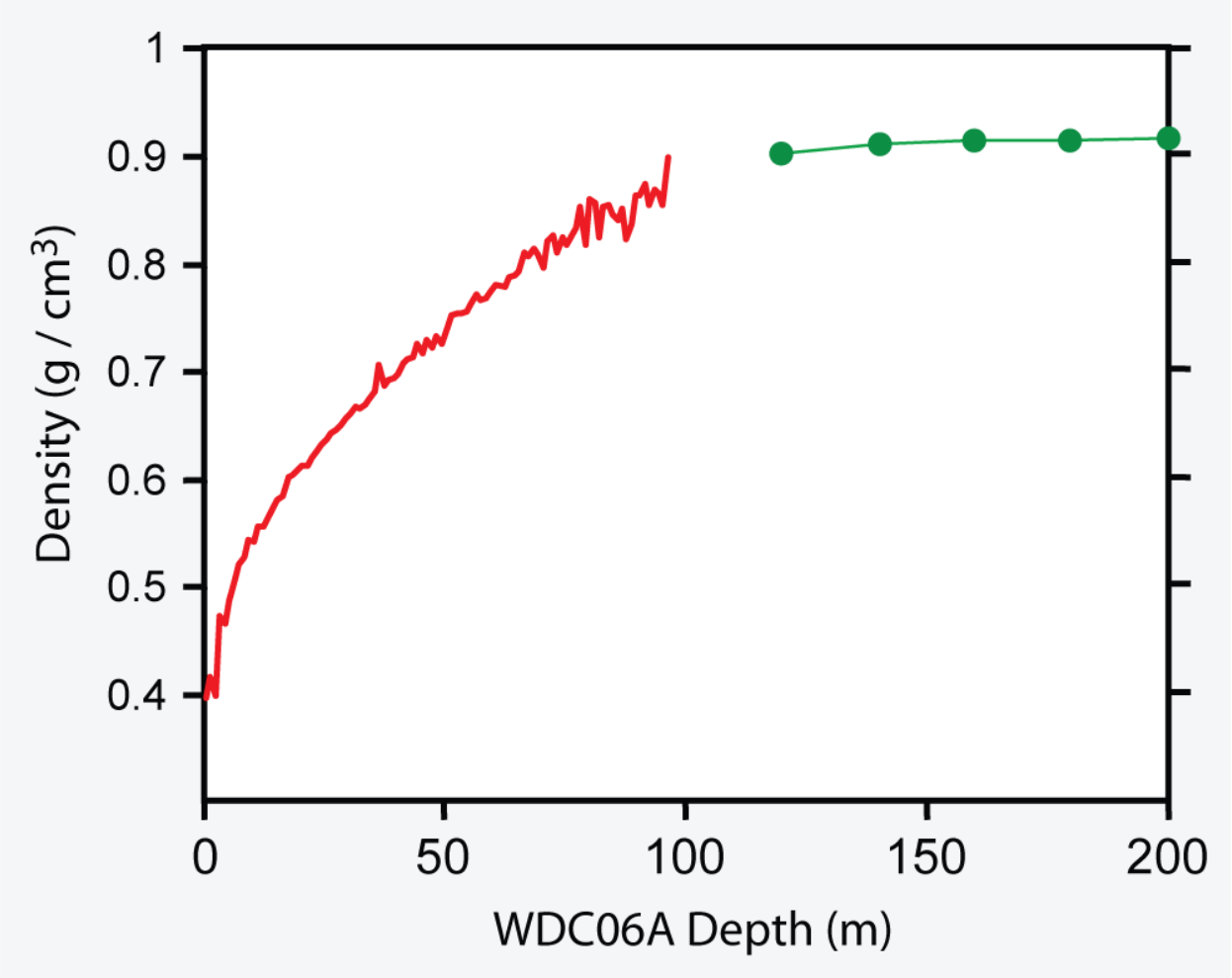

Figure 38: Density vs. depth at WAIS Divide. The red, solid curve shows density data measured every meter by Todd Sowers (unpublished). The dotted, green curve below 100 m shows measurements every 20 meters conducted by Joan Fitzpatrick and Richard Alley (unpublished). The approximately 100 m transition from snow and firn into solid ice occurs over a similar scale as the changes in fluorimetry we observe (e.g. Figure 26 and Figure 30).

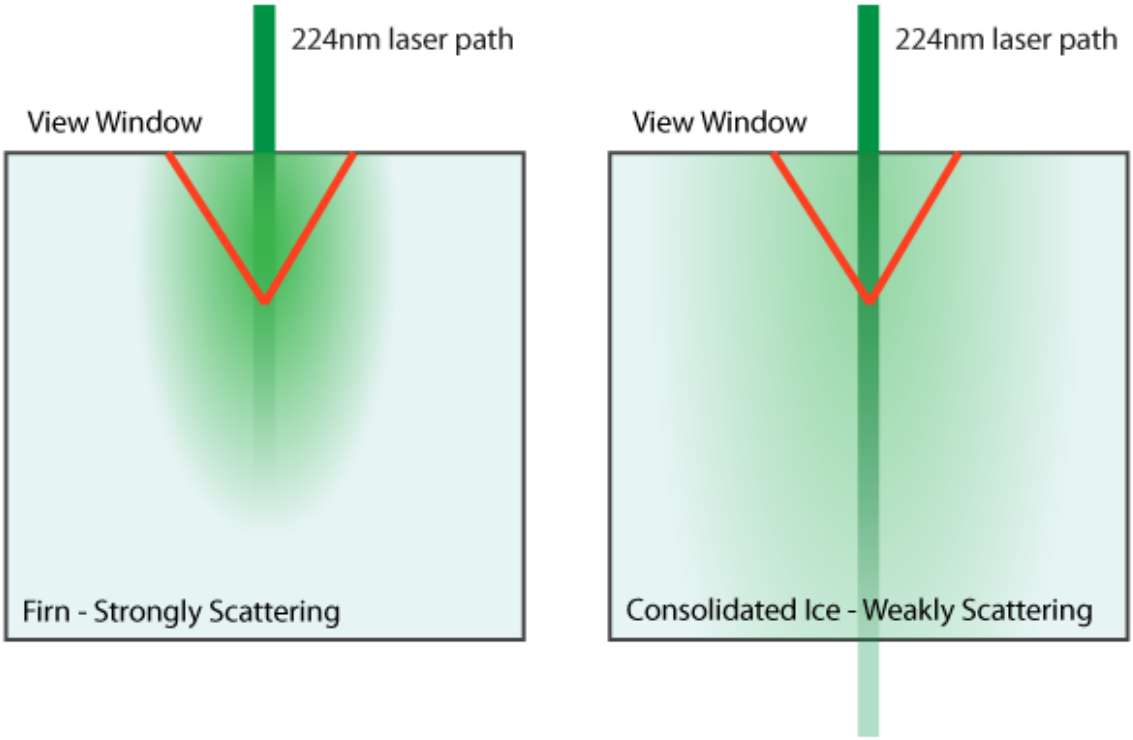

Figure 39: Schematic comparison of the evolution of the laser excitation in strongly scattering ice versus weakly scattering ice. In the weakly scattering case, one expects a significant portion of the laser beam to pass through the ice without having been either absorbed or scattered. By contrast, in the highly scattering ice, the beam will tend to diffuse around the point of entry into the ice. As a result the amount of material that can be illuminated and caused to fluoresce within the field of view of the instrument is substantially increased. Hence, we expect that strongly scattering ice will lead to higher apparent levels of fluorescence emission even for the same energy input.

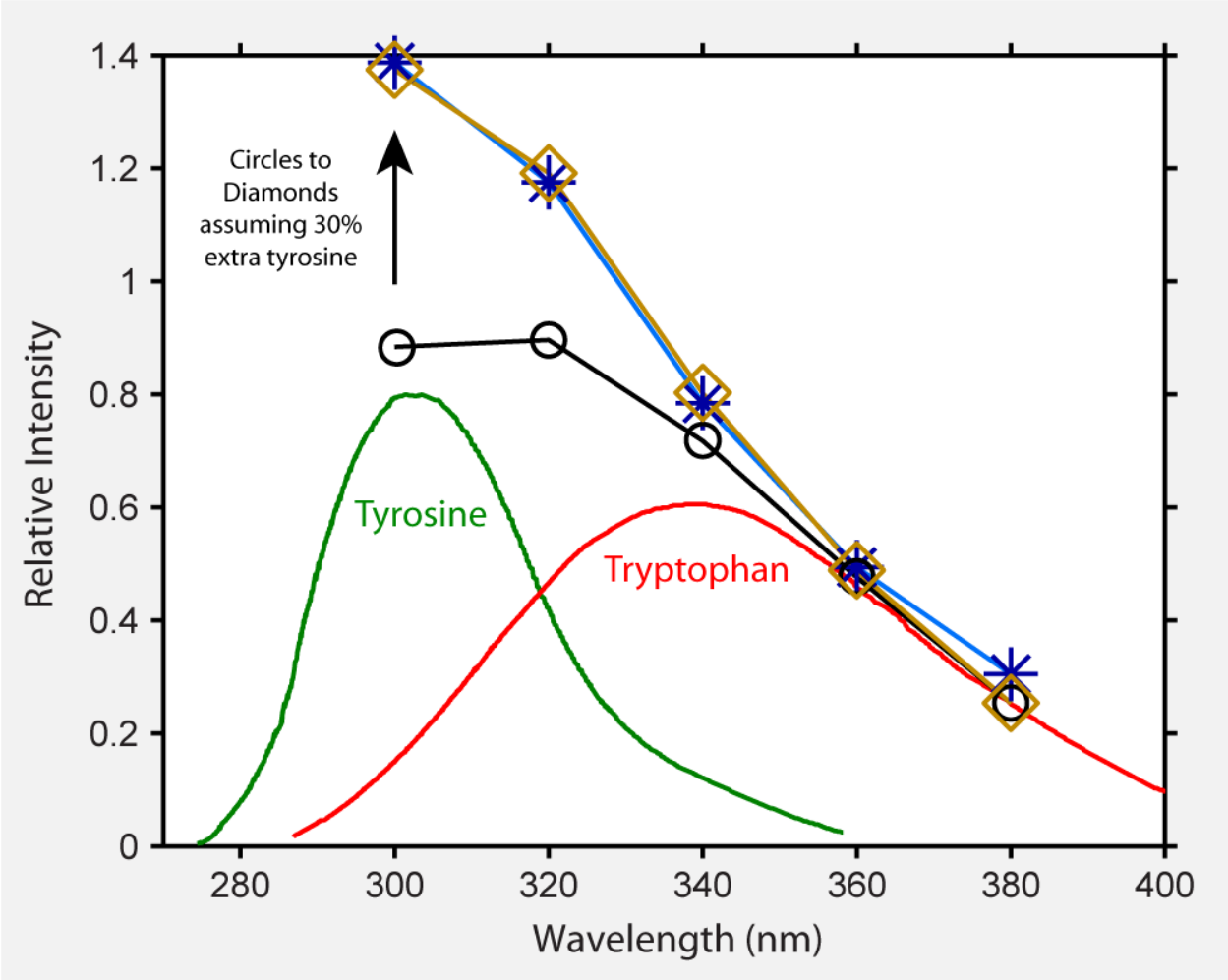

Figure 40: Comparison of the fluorescence spectrum from the dry-drilled portion of the WDC06A ice to that expected from amino acids. The blue curve marked with stars is the mean fluorescence spectrum detected by the BFS after averaging over all dry-drilled WDC06A core segments that were scanned. The smooth red and green curves show the expected emission spectra from tryptophan and tyrosine respectively, neglecting resonant energy transfer. Their relative weight is based on assumptions discussed in Section 6.4. Filtering these curves through the emission filters used in the BFS and summing the two components produced an expected emissions spectra indicated by black circles. This expected curve disagrees with the measured curve. As discussed in the text, one possible resolution to this discrepancy is to assume that the samples had ~30% more tyrosine than expected based on our assumptions. Such an adjustment would produce the brown curve marked with diamonds. However, as discussed in the text, it is at least as plausible to assume that our fluorescence spectrum is being influenced by some other unidentified fluorescence component.

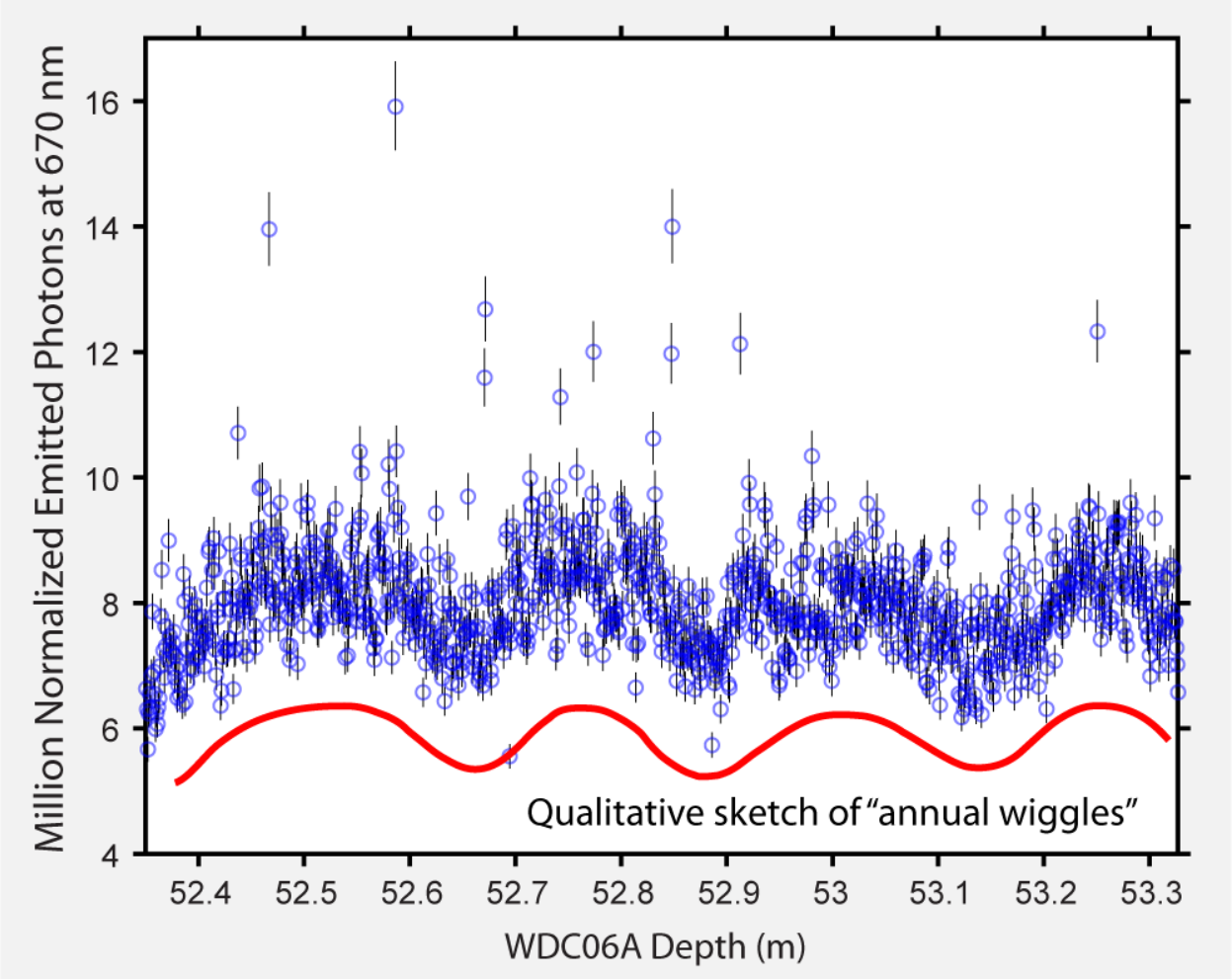

Figure 41: Example of oscillations in the 670 nm channel observed at shallow depths in the WDC06A core. The length scale is consistent with these fluctuations being interpreted as annual cycles. Approximately four years are represented in this plot.

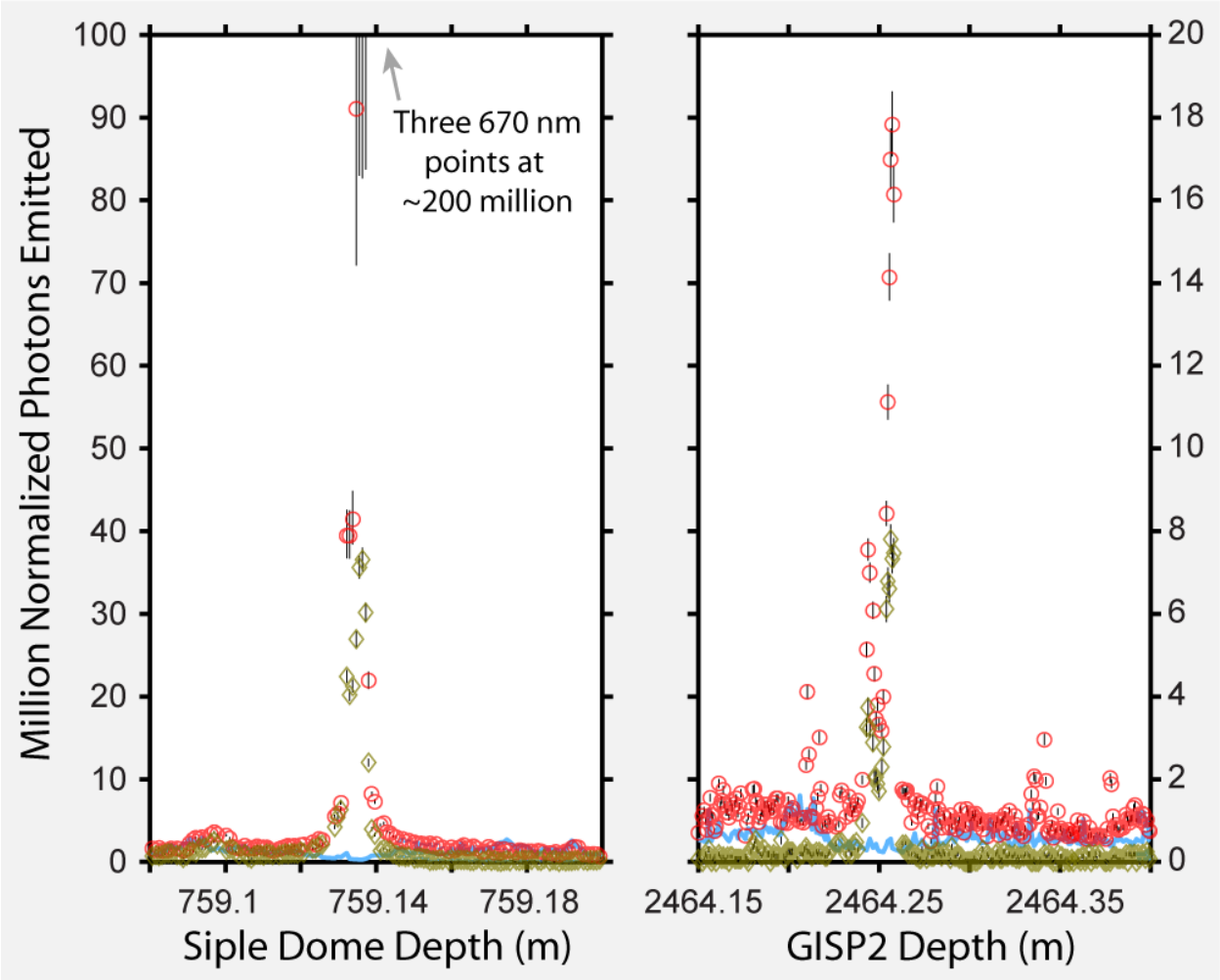

Figure 42: Fluorimetric scans of known ash layers in Siple Dome (left) and GISP2 (right) as measured in the 670 (red circles) and 710 nm (brown diamonds) channels of the BFS. The continuous blue curve denotes the average of the 300 to 380 nm fluorescence channels and is generally shown to be unresponsive to the presence of volcanic layers. The 710 nm channel will often go up 20 to 100 fold in the presence of volcanic ash and rarely at all in the presence of organics making it a sensitive discriminatory of ash layers. See Section 6.7.

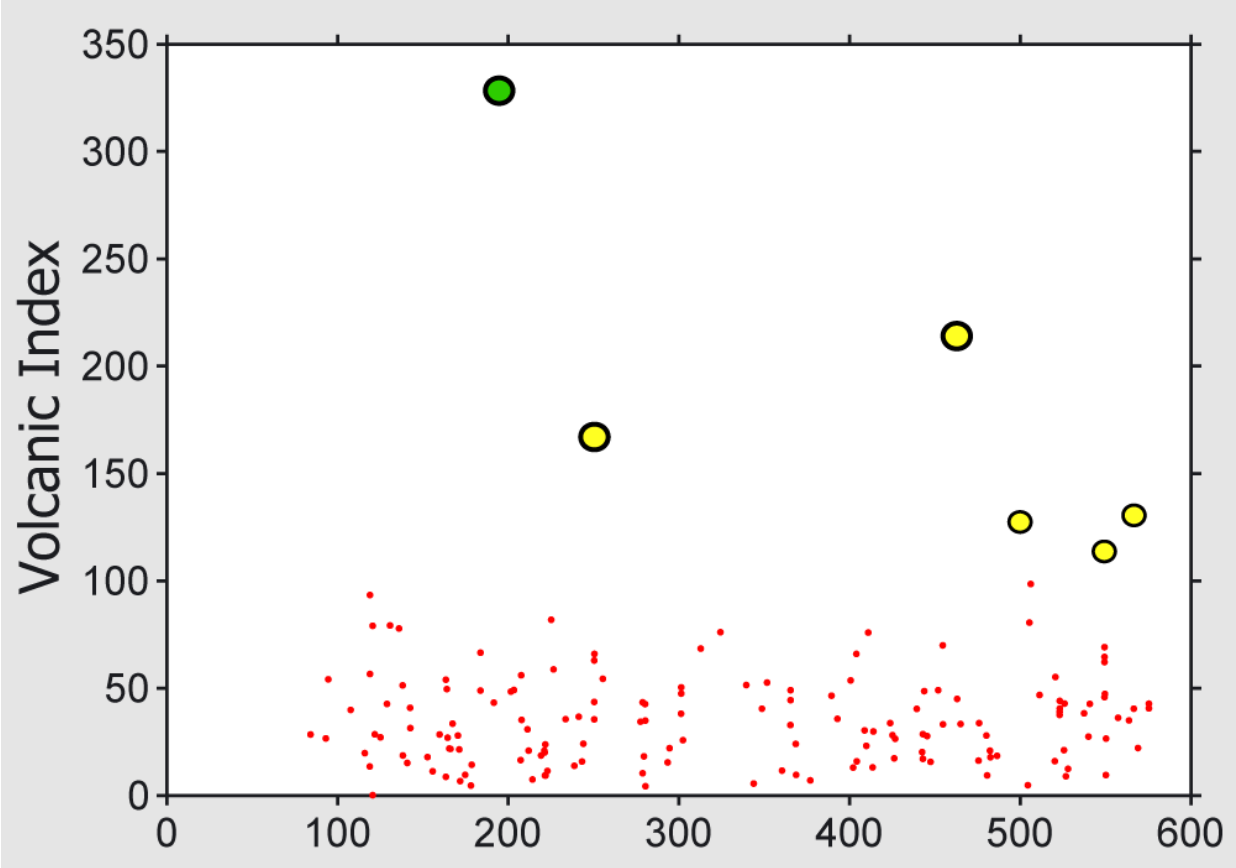

Figure 43: Volcanic index of WDC06A. Though four hundred thousand measurements were made on this core only the scans at a few hundred depths resulted in non-zero volcanic index values. Of these, most are at values of the index less than 100 which is believed to correspond to a background of mineral dust grains. The highest six values were analyzed by Nelia Dunbar to determine their composition. The five points in yellow were found to contain aeolian mineral dust, of unusually large particle sizes and concentrations. The one point in green was confirmed to contain a small number of volanic ash shards, thus demonstrating the ability of the instrument to locate an ash layer that was not recognizable by visual inspection.

10 Appendix

10.1 Labview Control Program

Available in the supplemental digital file *Labview Source Code.pdf.*

10.2 Matlab Analysis Script

The following script serves as sample code for applying the steps described in Section 4 and converting the BFS data files into properly processed and scaled results. This particular sample is designed to process the WDC06A portion of the 2008 NICL trip.

```
function cores = prepare_2008_WDC_data

% This function processes the 2008 WDC06A data from NICL though a
% series of adjustments that convert the raw measurements into useful,
% scaled and cleaned data structures for further consumption.

% Directory for 2008 WDC raw files
dd = 'C:\Recovered Files\Robert Rohde\Desktop\Flourescence Instruments\Merged Instrument\';

% Names of files to process
nms = {'first_cores.txt',
   'second_cores.txt',
   'third_set.txt',
   'fourth_set.txt',
   'fifth_set.txt',
   'sixth_set.txt',
   'seventh_set.txt',
   'eighth_set.txt',
   'ninth_set.txt',
   'tenth_set.txt',
   'eleventh_set.txt',
   'twelth_set_widecore.txt',
   'thirteenth_set_wide.txt',
   'last_wide_core.txt'
   };

% Calculate saturation response curve for photon counters
saturation_val = 5000;
mult = 8;
response = zeros(mult*saturation_val/10,2);
cnt = 1;
for k = 0:10:mult*saturation_val
   r = rand(k,1);
   r = floor(r*saturation_val);
   response(cnt,:) = [k, length(unique(r))];
   cnt = cnt + 1;
end
```

```
p = polyfit(response(:,1),response(:,2),10);
o = polyval(p,0:saturation_val*mult);
o(1) = 0;
sat_map = [o',(0:saturation_val*mult)'];

% Loads bandpass filter transmission curves for 300-380 nm
load 224_TUCS_Bandpass.txt
bp = X224_TUCS_Bandpass;
bp2 = interp1(bp(:,1),bp(:,1:end),250:800);


% Load and attach the 670 and 710 nm transmission curves to the above
load 'C:\Recovered Files\Data\filters\670.txt';
load 'C:\Recovered Files\Data\filters\710.txt';

bp670 = X670;
[g,I] = sort(bp670(:,1));
bp670 = bp670(I,:);

f = find(diff(bp670(:,1)) == 0);
bp670(f,:) = [];
bp2(:,7) = interp1(bp670(:,1),bp670(:,2),bp2(:,1));

bp710 = X710;
[g,I] = sort(bp710(:,1));
bp710 = bp710(I,:);

f = find(diff(bp710(:,1)) == 0);
bp710(f,:) = [];
bp2(:,8) = interp1(bp710(:,1),bp710(:,2),bp2(:,1));


% Loads counting efficiency data fof the photon counters.
load bialkali_ce.txt
load pmt06.sensitivity.txt
pmt = bialkali_ce;

[g,I] = sort(pmt(:,1));
pmt = pmt(I,:);
pmt2 = interp1(pmt(:,1),pmt(:,2),pmt(1,1):pmt(end,1));
pmt2 = [(pmt(1,1):pmt(end,1))',pmt2'];

[g,I] = sort(pmt06(:,1));
pmt06 = pmt06(I,:);
f = find(diff(pmt06(:,1)) == 0);
pmt06(f,:) = [];
pmt06_2 = interp1(pmt06(:,1),pmt06(:,2),pmt06(1,1):pmt06(end,1));
pmt06_2 = [(pmt06(1,1):pmt06(end,1))',pmt06_2'];

fk = findk(pmt2(:,1),360);
fk2 = findk(pmt06_2(:,1),360);
```

```
pmt_xx = [[pmt06_2(1:fk2,1), pmt06_2(1:fk2,2)*pmt2(fk,2)/pmt06_2(fk2,2)]; pmt2(fk:end,:)];
pmt3 = interp1(pmt_xx(:,1),pmt_xx(:,2),bp2(:,1));

load multialkali_ce.txt;
hmcm = multialkali_ce;
[g,I] = sort(hmcm(:,1));
hmcm = hmcm(I,:);

hmcm2 = interp1(hmcm(:,1),hmcm(:,2),hmcm(1,1):hmcm(end,1));
hmcm2  = [(hmcm(1,1):hmcm(end,1))',hmcm2'];
hmcm3 = interp1(hmcm2(:,1),hmcm2(:,2),bp2(:,1));


% Load transmission data for the laser line blocking filter.
load 248nm.txt;
lineblock = interp1(X248nm(:,1),X248nm(:,2)/100,bp2(:,1));


% Perform convolution of transmission curves from filters, line block,
% and photon counter counting efficiency.
f = find(~isnan(pmt3));
transmission = sum(bp2(f,2:6).*((pmt3(f).*lineblock(f))*ones(5,1)'));
f = find(~isnan(hmcm3) & ~isnan(bp2(:,7)));
transmission = [transmission, sum(bp2(f,7).*lineblock(f).*hmcm3(f))];
f = find(~isnan(hmcm3) & ~isnan(bp2(:,8)));
transmission = [transmission, sum(bp2(f,8).*lineblock(f).*hmcm3(f))];


% Process the files
for nn = 1:length(nms);

   % Load data into "vals"
   name = nms{nn}
   load([dd name]);
   vals = eval(name(1:end-4));


   %fix breaks in run number
   f = find(diff(vals(:,1)) < 0);
   for k = 1:length(f)
      vals(f(k)+1:end,1) = vals(f(k)+1:end,1) + vals(f(k),1) +1 - vals(f(k)+1,1);
   end


   % Known corrections for 2008 data files
   if nn == 10
      f = find(vals(:,1) == 78);
      vals(f,2) = 175.34;
      vals(f,4) = vals(f,4) + 0.1;

      f = find(vals(:,1) == 56);
      vals(f,2) = 201.1;
```

```
    vals(f,4) = vals(f,4) + 0.1;
end
if nn == 7
    f = find(vals(:,1) == 30);
    vals(f,[2:4]) = vals(f,[2:4])-1;

    f = find(vals(:,1) == 17);
    vals(f,3) = 393.95;
end
if nn == 5
    f = find(vals(:,1) == 30);
    vals(f,2) = 465.35;
    vals(f,4) = vals(f,4) + 0.35;
end


% Remove runs the ended early
un = unique(vals(:,1));
for k = 1:length(un)
    f = find(vals(:,1)==un(k));
    mn = min(vals(f,4));
    mx = max(vals(f,4));
    mnt = min(vals(f(1),[2,3]));
    mxt = max(vals(f(1),[2,3]));
    if mn > mnt + 0.06 | mx < mxt - 0.06
        vals(f,:) = [];
    end
end


% Smooth position record and remove dropped reads.
un = unique(vals(:,1));
for k = 1:length(un)
    f = find(vals(:,1)==un(k));
    mv = min(vals(f,end));
    vals(f,end) = vals(f,end)-mv;
    f2 = find(vals(f,5) > 0.7495);
    p = polyfit(vals(f(f2),end),vals(f(f2),4),1);
    vals(f(f2),4) = polyval(p,vals(f(f2),end));
    vals(f,end) = vals(f,end)+mv;

    f2 = find(min(vals(f,6:10)')<=4);
    vals(f(f2),:) = [];
end


% Shift position to center
for k = 1:length(un)
    f = find(vals(:,1)==un(k));
    mnt = min(vals(f(1),[2:3]));
    mxt = max(vals(f(1),[2:3]));
```

```
    pos = -0.02:0.0001:0.02;
    r = pos.*0;
    cnt = 1;
    for j = pos
        f2 = find(vals(f,4) < mnt + j | vals(f,4) > mxt + j);
        r(cnt) = mean(mean(vals(f(f2),6:10)'));
        cnt = cnt + 1;
    end

    f3 = find(r == min(r));
    shift = mean(pos(f3));

    vals(f,4) = vals(f,4) - shift;

    % Cut edges
    f2 = find(vals(f,4) < mnt | vals(f,4) > mxt);
    vals(f(f2),:) = [];
end


% Initialize uncertainty values.
vals0 = vals;
vv = vals(:,6:12);
f1 = find(vv >= 1111.1);
f2 = find(vv < 1111.1);
vv(f1) = vv(f1)*0.03;
vv(f2) = sqrt(vv(f2));

uncertain_up = vv;
uncertain_low = vv;


% Remove dropout values
for k = 6:10
    for j = 1:length(un)
        f = find((vals(1:end-2,k) - vals(2:end-1,k)) ./ (vals(1:end-2,k)+1) > 0.25 & ...
            (vals(3:end,k) - vals(2:end-1,k)) ./ (vals(3:end,k)+1) > 0.25 & ...
            vals(2:end-1,k) > 100 & ...
            vals(2:end-1,1) == un(j));

        vals(f,:) = [];
        uncertain_up(f,:) = [];
        uncertain_low(f,:) = [];
    end
end


% Subtract background values
for k = 1:length(un)
    f = find(vals(:,1)==un(k));
    vals(f,6:12) = vals(f,6:12) -vals(f,13:19);
```

```
    vv = vals(f,13:19);
    f1 = find(vv < 1111.1);
    f2 = find(vv >= 1111.1);
    vv(f1) = sqrt(vv(f1));
    vv(f2) = 0.03*vv(f2);

    uncertain_up(f,:) = sqrt(uncertain_up(f,:).^2 + vv.^2);
    uncertain_low(f,:) = sqrt(uncertain_low(f,:).^2 + vv.^2);
end


% Adjust for saturation effect
for k = 6:12
    f1 = find(vals(:,k) > max(sat_map(:,1)));
    vals(f1,k) = max(sat_map(:,1));

    f2 = find(vals(:,k) < min(sat_map(:,1)));
    vals(f2,k) = min(sat_map(:,1));

    vv = vals;
    CX = interp1(sat_map(:,1),sat_map(:,2),vals(:,k));
    vals(:,k) = CX;

    CX = interp1(sat_map(:,1),sat_map(:,2),vv(:,k)+uncertain_up(:,k-5));
    f1 = find(vv(:,k)+uncertain_up(:,k-5) > max(sat_map(:,1)));
    uncertain_up(:,k-5) = CX - vals(:,k);
    uncertain_up(f1,k-5) = 1e8;

    CX = interp1(sat_map(:,1),sat_map(:,2),vv(:,k)-uncertain_low(:,k-5));
    f1 = find(vv(:,k)-uncertain_low(:,k-5) < min(sat_map(:,1)));
    uncertain_low(:,k-5) = vals(:,k) - CX;
    uncertain_low(f1,k-5) = vals(f1,k);
end


% Adjust for laser power
m = mean(vals(:,20));
s = std(vals(:,20));
f = find(vals(:,20) > m + 5*s | vals(:,20) < m-5*s);
vals(f,:) = [];
uncertain_up(f,:) =[];
uncertain_low(f,:) = [];
for k = 1:length(un)
    f = find(vals(:,1)==un(k));
    vals(f,6:12) = vals(f,6:12)./(vals(f,20)*ones(1,7));
    uncertain_up(f,:) = uncertain_up(f,:) ./ (vals(f,20)*ones(1,7));
    uncertain_low(f,:) = uncertain_low(f,:) ./ (vals(f,20)*ones(1,7));
end


% Remove data with bad timing diagnostics
f = find(vals(:,22) > 35);
```

```
    vals(f,:) = [];
    uncertain_up(f,:) =[];
    uncertain_low(f,:) = [];


    % Scale for filter transmission and counting efficiency
    vals(:,6:12) = vals(:,6:12) ./ (ones(length(vals(:,1)),1)*transmission);
    uncertain_up(:,1:7) = uncertain_up(:,1:7) ./ (ones(length(vals(:,1)),1)*transmission);
    uncertain_low(:,1:7) = uncertain_low(:,1:7) ./ (ones(length(vals(:,1)),1)*transmission);


    % Scaled for visibility
    vals(:,6:12) = vals(:,6:12) ./ (0.0789 / (4*pi));
    uncertain_up(:,1:7) = uncertain_up(:,1:7) ./ (0.0789 / (4*pi));
    uncertain_low(:,1:7) = uncertain_low(:,1:7) ./ (0.0789 / (4*pi));


    % Save data into processed files
    data = [vals(:,[1,4,6:12]), uncertain_up, uncertain_low];
    save([dd 'processed2.' name],'-ascii','data');


    % Data structures for later
    vlist{nn} = vals;
    ulist{nn} = uncertain_up;
    dlist{nn} = uncertain_low;
    elist{nn} = vals0;
    clist{nn} = get_comments([dd nms{nn}]);

end


% % Create files broken into blocks by depth.
% vset =[];
% for k = 1:length(vlist)
%     vset = [vset; k*ones(length(vlist{k}(:,1)),1), vlist{k}];
% end
%
% for block = 0:20:600
%     f = find(vset(:,5) > block & vset(:,5) < block + 20);
%     data = vset(f,[1,2,5,7:13]);
%     [s,I] = sort(data(:,3));
%     data = data(I,:);
%     save([dd 'wdc_block.' num2str(block) '.txt'],'-ascii','data');
% end


% Prepare data structure
cnt = 1;

core.start = 0;
core.stop = 0;
```

```
core.depths = [];
core.signal = [];
core.up_error =[];
core.down_error =[];
core.laser = [];
core.comments = {};
core.mid = 0;
core.nominal = [];
core.nom_error = [];
core.meanlaser = [];
core.edge = [];
core.set = 0;
core.run = 0;
core.time = [];

cores(1) = core;

% Load data structure
for k = 1:length(vlist)
   un = unique(vlist{k}(:,1));
   for j = 1:length(un)
      f = find(vlist{k}(:,1) == un(j));
      core.start = min(vlist{k}(f(1),[2,3]));
      core.stop = max(vlist{k}(f(1),[2,3]));
      core.depths = vlist{k}(f,4);
      core.signal = vlist{k}(f,6:12);
      core.up_error = ulist{k}(f,:);
      core.down_error = dlist{k}(f,:);
      core.laser = vlist{k}(f,20);
      core.mid = (core.start + core.stop)/2;
      core.edge = (core.depths < core.start + 0.1) | (core.depths > core.stop - 0.1);
      core.time = vlist{k}(f,end);
      f = find((~isnan(mean(core.signal')')) & ...
         (core.depths >= core.start + 0.1) & ...
         (core.depths < core.stop - 0.1));
      if length(f) > 20
         % Record nominal, per piece values.
         for m = 1:7
            fx = find(core.up_error(f,m) < core.signal(f,m) & ...
               core.down_error(f,m) < core.signal(f,m)/2);
            core.nominal(m) = mean(core.signal(f(fx),m));
            err = max([core.up_error(f(fx),m), core.down_error(f(fx),m)]')';
            ss = sqrt(sum(err.^2)/length(err).^2);
            tt = std(core.signal(f(fx),m)) / sqrt(length(fx));
            core.nom_error(m) = max(ss,tt);
         end
         core.meanlaser = mean(core.laser(f));
      else
         core.nominal = ones(1,7).*NaN;
         core.meanlaser = NaN;
      end
```

```
        if un(j) <= length(clist{k})
            core.comments = clist{k}{un(j)};
        else
            core.comments = {};
        end

        core.run = un(j);
        core.set = k;

        cores(cnt) = core;
        cnt = cnt + 1;
    end
end


% Helper function to load comments.
function clist = get_comments(name)

fid = fopen(name);
lastrun = -1;
running = 2;

comments = {};
last_comments = comments;

clist = {};
run = 1;

while ~feof(fid)
    line = fgetl(fid);
    if length(line) > 0 & line(1) == '%'
        if running == 2 & line(2) == '='
            running = 0;
            t = comments;
            comments = filter_comments(comments,last_comments);
            last_comments = t;
            disp(comments);
            if lastrun > 0
                clist{lastrun} = comments;
            end
            comments ={};
        elseif running==0 & length(line) > 1 & line(2) == '='
            line = fgetl(fid);
            if length(line)>1
                comments{end+1} = line(2:end);
                %disp(line);
            end
            running = 1;
        end
        if running == 2
            %disp(line);
            comments{end+1} = line(2:end);
```

```
        end
    elseif length(line) > 10
        run = str2num(line(1:3));
        run = run(1);
        if run ~= lastrun
            %disp(run);
            running = 2;
        end
        lastrun = run;
    end
end
if running==2
    comments = filter_comments(comments,last_comments);
    disp(comments);
end


% Helper function to cleanup comments.
function comments = filter_comments(comments, last_comments)

k = 1;
while k < length(comments)
    j = k + 1;
    while j <= length(comments)
        if strcmp(comments{j},comments{k}) == 1
            comments(j) = [];
        else
            j = j +1;
        end
    end
    k = k + 1;
end

k = 1;
while k <= length(comments)
    j = 1;
    while j <= length(last_comments)
        if strcmp(last_comments{j},comments{k}) == 1
            if strcmp(comments{k},'cleaned with ethanol') == 0
                comments(k) = [];
                k = k - 1;
                break;
            else
                j = j + 1;
            end
        else
            j = j +1;
        end
    end
    k = k + 1;
end
```